SYMMETRY BREAKING AND SINGULARITY STRUCTURE IN BOSE-EINSTEIN CONDENSATES

by

Kelley A. Commeford

A thesis submitted to the Faculty and the Board of Trustees of the Colorado School of Mines in partial fulfillment of the requirements for the degree of Master of Science (Applied Physics).

Golden, Colorado

Date _____

Signed: _____
Kelley A. Commeford

Signed: _____
Dr. Lincoln D. Carr
Thesis Advisor

Golden, Colorado

Date _____

Signed: _____
Dr. Tom Furtak
Head
Department of Physics

ABSTRACT

This thesis presents an analytical description of the effect of a symmetry breaking impulse on a vortex, or singularity, trapped in an axisymmetric harmonic potential. The analysis is performed for a weakly interacting Bose-Einstein condensate. For the purposes of analytical approximation, we initially assume the interaction time to be much larger than that of the initial dynamics; later this approximation is examined by complete numerical solution of the governing equations. We reserve the term *vortex* for the interacting case, and use the more generic term *singularity* for both interacting and non-interacting cases, when the interacting or non-interacting condensate density drops to zero and the phase winds by a non-zero integer multiple of 2π around the density zero. We find that our analytical approach based on the singularities in the non-interacting case predicts most of the dynamics of vortices in the interacting case, including the initial breakup of a vortex into singly charged daughter vortices, and their trajectories in the trapping potential up until they approach each other and collide after spiraling back in due to the action of the harmonic trap. Thus we show that the kinetics drive most of the interactions, not interactions. First, we construct the singularity state for the quantum harmonic oscillator and propagate it through the discretely symmetric impulse using the time-evolution operator for a given Hamiltonian the impulse approximation allows us to factorize the time evolution operator and obtain analytical results. After the impulse, the resulting wave function can be treated using the Feynman propagator for a harmonic oscillator potential. Once the necessary integration has been carried out, it is discovered that the symmetry of the initial singularity is broken into that of the impulse. In this analysis, we take the impulse to have four-fold symmetry. The actual form of the impulse does not change the dynamics of the post-symmetry breaking singularities, only the order of symmetry. Using an incident singularity of winding number $\ell = 3$ as our case study, the result-

ing singularity structure after symmetry breaking consists of five singularities, one at the origin, with winding number now $\ell = -1$, and four singularities propagating periodically about the origin of winding number $\ell = 1$. The initial winding number of the parent singularity is therefore conserved. The four daughter singularities propagating about the axis do so in an oscillatory manner, where the recombination time of the singularities is half the trapping potential period. The maximum radius the trajectories achieve is dependent on the impulse strength and the trapping frequency. We develop equations of motion and a force-torque model to describe the dynamics of daughter singularities. We find that the singularities are imprinted by the impulse with two distinct non-trivial sources of motion. We develop a simple dynamical model treating the singularities as point particles. We discover that there are two effective forces the singularities experience during symmetry breaking; a repulsive harmonic force that causes the trajectories to propagate outward, and a Magnus force that introduces a torque about the axis of symmetry. The singularities initially travel away from each other due to the presence of a singular repulsive potential at time $t = 0$ immediately after symmetry breaking. A torque is also imprinted, causing them to rotate around the axis of symmetry. Although the singularities initially repel from the origin, the harmonicity of the trapping potential causes them to fold back on themselves after one-half the trapping period, creating a four-fold petal-like structure. When compared to numerical integration of the Gross-Pitaevskii equation, we found that for small enough impulse strength and duration, the impulse serves solely to break the symmetry of the system. By increasing the duration of the impulse while decreasing its strength, we obtain the same results to within 10%. This demonstrates that for weak enough symmetry-breaking potentials, the impulse approximation is unnecessary. All results can also be applied to singular optics for an optical vortex in a parabolic gradient index fiber due to the mapping from the Schrödinger equation to the Helmholtz equation.

TABLE OF CONTENTS

LIST OF FIGURES

ACKNOWLEDGEMENTS

After countless hours and numerous seemingly unsurmountable roadblocks, we have finally seen this thesis to completion. I cannot express enough gratitude to the advisor that has pushed me further than anyone ever has before, or probably ever will. Dr. Lincoln Carr not only served as my advisor, but also as my mentor, professor, employer, counselor, and most of all, my guide to self-discovery. I have learned much about myself and how I interact with others these past two years that will set the tone for all future endeavors I hope to tackle. Dr. Carr didn't hold my hand through research until I was comfortable on my own. He threw me in headfirst and taught me how to swim. He trusted me enough to figure things out for myself, he taught me responsibility, and how to operate like a professional. Although it took longer than anticipated, I have grown as a student and as a researcher more than I ever could have imagined, all thanks to Dr. Carr.

I would also like to thank the Colorado School of Mines for providing me with an amazing education and an unforgettable college experience. I will cherish my time as an Oredigger until the day I die. Within the physics department, I would like to thank Barbara and Summer for ensuring I always remembered to dot my i's and cross my t's. I would not have survived without you. Furthermore, I would like to thank Dr. Miguel Angel García March for providing support on this project, and Dr. Albert Ferrando for introducing me to the wonderful world of symmetry breaking. I would also like to thank Dr. Albert Ferrando and Dr. Jezabel Pérez for hosting me in Spain for the summer, where I got a chance to immerse myself in a new culture while expanding my knowledge of physics, mathematics, and the Spanish language.

I would like to thank my thesis committee, Dr. Bernard, Dr. Durfee, and Dr. Hereman. I chose the three of you because I knew you would push me to produce the best thesis I possibly could, and you did. I am truly proud of this publication,

and I thank you for your help. Last, but definitely not least, I would like to thank the National Science Foundation for their generous support, and of course, Susan and Chris Commeford for their unyielding love and motivation.

Poets say science takes away from the beauty of the stars - mere globs of gas atoms. I, too, can see the stars on a desert night, and feel them. But do I see less or more?

-Richard Feynman

CHAPTER 1

INTRODUCTION

Vortices are ubiquitous to many diverse branches of science, including fluid dynamics [1], meteorology [2], cosmology [3, 4], liquid crystals [5], superconductivity [6–8], solid state physics [9], and nonlinear singular optics [10, 11]. Whenever a hydrodynamic description is appropriate, one has the possibility of vortices [1]. In particular, vortices have been realized experimentally in Bose-Einstein condensates (BEC), obtained when bosons are cooled down to sub-microKelvin temperatures [12–22]. These vortices are expected to offer interesting applications in interferometry [23], and as a means to study the behavior of random polynomial roots [24]. Vortices are characterized by the presence of a singularity in the value of its phase to which an integer number can be associated, called vorticity, topological charge, or winding number [25, 26]. This singularity behaves as a particle-like object whose motion can be studied with respect to the background condensate. The determination of this motion and its control is applicable in the study of many of the fields described above. We use the term *singularity* for the generic case of both interacting and non-interacting BECs. Since only an interacting BEC is described by hydrodynamics, we only use the term vortex in the interacting case. In this thesis we determine the dynamics of a vortex in a Bose-Einstein condensate when it is struck by a symmetry breaking impulse. A two-dimensional vortex with winding number greater than 1 is generated in an axisymmetric harmonic potential, and immediately a symmetry breaking potential is turned on transversely, i.e., in the plane containing the vortex, for a very short period of time, such that it can be described by an impulse with a constant area of $\Delta V \Delta(t)$. This potential shows some rotational discrete point symmetry of order N, that is, it reproduces itself under multiple integer rotations of $2\pi/N$ [27]. The topological charge of the vortex, taken to be $l = 3$ in this work as a case study, will experience

a transformation, as discussed in [28–30]. The parent singularity will disintegrate into a number of single-charged daughter singularities of different sign, analogous to the disintegration of a radioactive nucleus. The number and sign of these daughter singularities are related to the peculiarities of the symmetry breaking impulse [31]. Figure 1.1 shows a representation of this discretely symmetric impulse acting on the parent singularity.

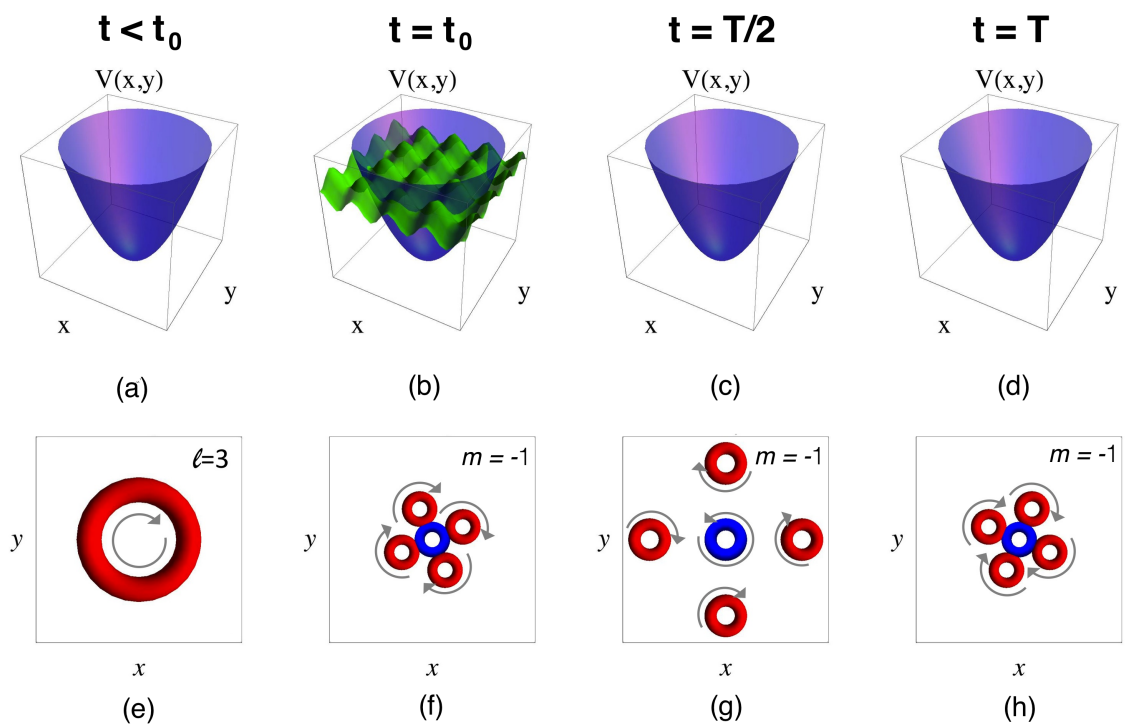

Figure 1.1: A parent singularity of winding number $\ell = 3$ is imprinted by a C_4 discretely symmetric impulse. This symmetry breaking process will result in five daughter singularities, one at the origin of winding number $m = -1$, and four off-axis of winding number $m = 1$. The red singularities have positive winding number, and rotate clockwise. The central blue singularity has a negative winding number and rotates counterclockwise.

Here we determine the path followed in a harmonic potential by the ejected daughter singularities after the impulse. We obtain these trajectories analytically for the non-interacting case by utilizing the Feynman propagator for a harmonic potential, and determine their validity in the weakly interacting case. In the non-interacting

case we find that the parent singularity reconstructs itself from the daughter singularities after a period of time. The repulsion between interacting singularities in the weakly interacting system prevents the parent singularity to be reconstructed, hence describing a helical trajectory around the origin. We discover that there are two effective forces the singularities experience during symmetry breaking; a repulsive harmonic force that causes the trajectories to propagate outward, and a Magnus force that introduces a torque about the axis of symmetry [32]. It is possible for the ideal Bose-Einstein condensate to condense into more than one single-particle mode [33], i.e., be fragmented, so we are actually treating the interacting BEC, but for times much less than the interaction time, described in 2.5.2. Our results pave the way to the control and manipulation of the motion of singularities by means of symmetry breaking impulses. The results are equally applicable to the neighboring field of nonlinear singular optics [11] by exchanging time evolution with axial-spatial evolution and the symmetry breaking impulse with an inhomogeneous thin diffracting element. The study of dynamics of singularities and their interaction is an exciting field with many potential applications. The dynamics of vortex dipoles; their interaction, oscillation, tunneling, and their collapse; has been theoretically studied in the framework of BEC [34–40]. Other structures of singularities and the interactions among them lead to elaborated trajectories [41, 42], as discussed numerically in [43]. The geometry of vortex trajectories, like loops or hyperbolas, is related to vortex creation and annihilation and vortex interactions, and its study leads to a variety of vortex structures [25, 44–47]. Moreover, the interpretation of the role of a singularity in quantum dynamics is an interesting issue, as well as the effect of the dynamics of the singularities in the quantum system [48, 49]. Also, vortices in BEC and nonlinear optics can show more than one off-axis singularity, called clusters of vortices [26, 50–56]. These structures are typically unstable, showing very slow dynamical decay rates, though some controversy has been built up around this issue [57–59]. Here,

we obtain a breathing cluster of vortices, and we obtain numerical stability of this structure along the times of the evolution. The outline of this thesis is as follows. In chapter 2, we present the various concepts and uses of vortices in Bose-Einstein condensation as well as sketching the analogy in nonlinear optics. For those unfamiliar with either field, we briefly explain what an optical vortex is, and how to create a Bose-Einstein condensate. We also present the uses of vortices in several fields, and how their manipulation can be advantageous. We finish the chapter by describing the previous work and the problem to be solved in this thesis. Chapter 3 reviews some basic mathematical techniques for the linear Schrödinger equation, starting with the derivation of the harmonic-oscillator propagator. The propagator allows us to take our initial singularity and propagate it to a future time and place. We will use the propagator to arrive at our final state as a function of time, allowing us to see the distinct singularities that arise after symmetry breaking. We also introduce the unitary time-evolution operator that will be used to propagate our singularity through the impulse. In chapter 4, we introduce the discretely symmetric impulse that breaks the symmetry of our initial singularity by constructing a potential profile valid for any spatially variant discretely symmetric potential. We then use this profile to construct the unitary time-evolution operator necessary to propagate the initial parent singularity through the impulse. Using group theory [60], we can utilize various symmetry arguments to simplify the mathematics of the unitary time-evolution operator. In chapter 5, we introduce the initial test case singularity, with winding number $\ell = 3$, that will be tested in this thesis. Due to the dependence on l that will arise in the propagation integral, we need to choose a distinct value for ℓ in order to carry out our calculations analytically. We choose $\ell = 3$ as our test case to observe the difference between the constant potential done previously [61] and the harmonic potential done here [32]. We then carry out the harmonic oscillator propagation integral introduced in chapter 3 and calculate the trajectories of the post-symmetry breaking singulari-

ties. We plot the amplitude of the wave function after symmetry breaking in order to get a preliminary view of the post-symmetry breaking singularity motion. The final wave function can be grouped into three different terms, explicitly unveiling the angular momentum structure of the system. This angular momentum structure is used to calculate the trajectories of an off axis singularity, which can then be rotated by $n\pi/2$ radians, where n is an integer, to describe the other three singularities due to the four-fold symmetry of the imprinting impulse. Chapter 6 utilizes the trajectories of the previous chapter to arrive at analytic descriptions of the equations of motion. These equations of motion are analyzed to understand the fundamental motion that the singularities undergo once symmetry is broken. We discover that there are two effective forces the singularities experience during symmetry breaking, a repulsive harmonic force that causes the trajectories to propagate outward, and a force that introduces a torque about the axis of symmetry. We analyze the two effective forces in detail. These forces are similar to those found in the constant-potential study in the optical regime [61], as we would expect. However, the singularities continue to oscillate about the origin in a flower shape due to the harmonicity of the trapping potential. Chapter 7 includes a comparison of the analytic trajectories calculated in this thesis with a numerical analysis performed by my collaborator Dr. M. A. Garcia March [32]. The numerical analysis was done using the Gross-Pitaevskii equation, with the nonlinearity set to zero to recover the traditional Schrödinger equation, or nonlinear Schrödinger equation, including evaluation of the impulse approximation in the limiting non-interacting case. We also compare the trajectories with the local minima of the wave function to see how well they match. For the nonlinear system, we compare the analytic trajectories with numerical data for both attractive and repulsive interparticle interactions and quantitatively analyze the accuracy of the linear approximation.

CHAPTER 2

BACKGROUND

In this chapter, we introduce several concepts needed to lay the foundation for this thesis, beginning with the description of Bose-Einstein condensation (BEC). We also discuss several uses for vortices in BEC, as well as their optical analog. Finally, the previous work is discussed, followed by an introduction to the current theoretical system.

2.1 Bose-Einstein Condensates

Bose-Einstein condensation occurs when a group of bosons is cooled to extremely low temperatures on the order of microKelvin or smaller. At these temperatures, the classical picture of a thermal distribution of particles across all different energy states no longer applies. The bosons begin dropping into the ground state one by one, until eventually all of the particles are in a single macroscopically occupied mode. When particles are in the ground state, they have the lowest energy available, so they also have low momentum. Thus, when the particles condense, their momentum is bound near zero. By Heisenberg's uncertainty principle [62], we cannot know the momentum and the position simultaneously. Thus, if the momentum is bound to a range near zero, the particle's position becomes ill defined. This causes the individual particle wave function to spread out, making it equally likely to find them anywhere in the sample. If the particles are close to each other their wave functions blur into their neighbors, until eventually all the individual wave functions coalesce into a single function for the entire system, and the individual particles become indistinguishable [63]. In an ideal BEC, the particles do not interact with each other, so the total wave function behaves exactly like the single particle [64]. This phenomena allows us to see quantum effects on a mesoscopic or macroscopic scale rather than

working with a single atom. Fermions are identical and indistinguishable from each other, so due to the anti-symmetry of their wave functions, we cannot have two of the same fermions in the same state. Thus, fermions fill more energy levels when more particles are added to the system. This is known as the Pauli-Exclusion principle, seen in Figure 2.1, and is the reason that BECs cannot be made with fermions [65]. However, bosonic wave functions are symmetric and distinguishable, so we can put as many of them in single state as we want, thus allowing us to create a BEC in which more than one particle may occupy the ground state. In an ideal BEC, all of the bosons are in the ground state.

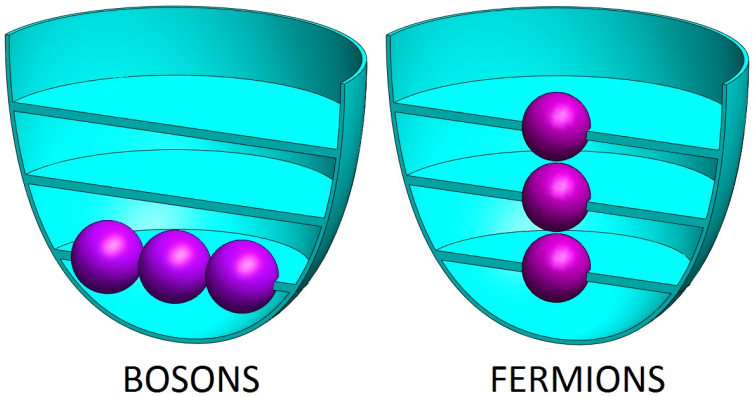

Figure 2.1: Filling of states for bosons and fermions: Identical bosons can occupy the same state due to the symmetry of their wave functions. For a BEC, all of the particles are in the ground state. Fermions can only have one particle per state due to the anti-symmetry of their wave functions, and thus fill more energy levels. Figure does not represent spin-degeneracy.

2.1.1 Creating Bose-Einstein Condensates in the Laboratory

In 1995, BECs were made in the laboratory for the first time by the group led by Eric A. Cornell and Carl E. Wieman from JILA in Boulder, Colorado using Rubidium-87 molecules [63]. Another group led by Randall Hulet at Rice University created a BEC using lithium atoms [66]. An independent research group led by Wolfgang Ketterle of Massachusetts Institute of Technology created a BEC using Sodium-23

atoms about four months after Cornell and Wieman [67]. Cornell, Wieman, and Ketterle won the 2001 Nobel prize for their experiments. To create a BEC, the atoms need to be trapped in a vacuum on the order of 10^{-11} Torr [68], and then cooled using laser trapping and cooling. When photons from the trapping laser beams hit the atom, they transfer momentum. To get the atoms to slow down and lower their energy, we want them to interact mainly with the photons traveling in the opposite direction. Much like a car crash, the head-on scattering of a photon off of the atom will slow the atom down, lowering its momentum in the direction it was traveling. The frequencies of the trapping lasers are adjusted to take advantage of the Doppler effect [69]. If the atom is traveling in the same direction as the photons, the laser frequency appears to be lower, and the photons will not have a high enough energy to be absorbed and reemitted by the atom. If the atom is moving against the photons, the laser frequency will be effectively higher, allowing the photons to have a high enough energy to be absorbed and reemitted by the atom, and pushing the atom back to the center of the trap [70]. This is known as velocity dependent scattering and is illustrated in Figure 2.2.

To confine atoms to the middle of the laser trap, we need them to interact with photons coming from the six spatial directions. This is done using an array of lasers adjusted to the absorption frequency of the particles being held. There are two lasers along each Cartesian axis to ensure photons are coming from each of the six spatial directions. This method cools the atoms by damping atomic motion, and therefore lowering the energy. However, the atoms can still float out of the trap when hit by random photons that scatter from other atoms, so we need another trapping mechanism. At this point, magnetic fields are turned on. Atoms have a magnetic dipole moment, so they interact with magnetic fields. The spatially varying magnetic field can be tweaked to confine the atoms closer, creating what is known as a magneto-optical trap [70], shown in Figure 2.3. We create a harmonic trap by using

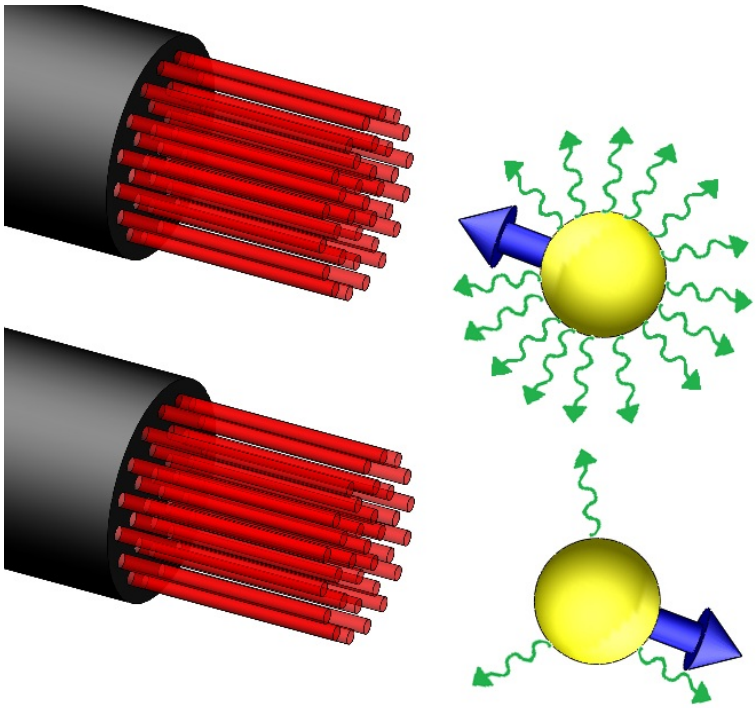

Figure 2.2: Velocity dependent scattering: If the atom is moving toward the laser beam, it scatters more photons, pushing it back to the center of the trap. If the atom is moving away from the laser beam, and therefore toward the center of the trap, it scatters less photons.

a time-orbiting magnetic field, which creates the pancake shape of a two-dimensional harmonic trap. By using a specific magnetic field profile, atoms that try to escape are subject to the *Zeeman effect*, and get their resonance frequency shifted closer to the frequency of the lasers by the magnetic field, making the atom more likely to get a photon kick back to the center of the trap [71].

Some atoms are still moving too fast to effectively reduce the temperature of the system, so we then reduce the confining field to let the most energetic atoms escape. This is known as evaporative cooling. When two atoms collide, they transfer momentum. The atoms with more momentum are moving faster, and are therefore warmer than their counterparts. If we let this high-energy atom escape, the remaining atoms are the slow moving atoms, so the entire system is effectively cooled. As explained previously, cold atoms have low momentum, making their position ill defined. By

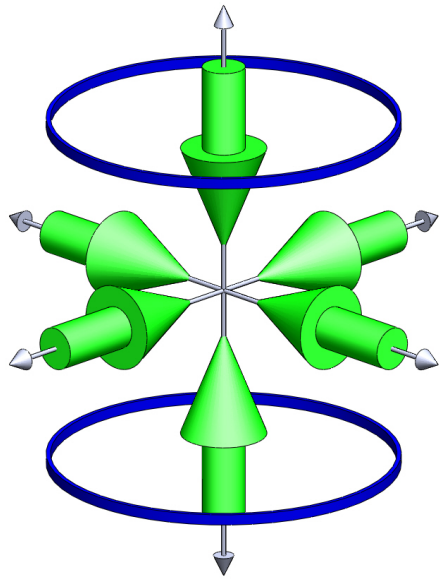

Figure 2.3: A magneto-optical trap: A pair of laser beams (green arrows) along each Cartesian axis is sufficient to trap the atoms. Two Helmholtz coils (blue circles) create a magnetic field to further confine the particles to the center of the trap.

having a collection of sufficiently cold atoms in our trap, the individual wave functions blur together, making the total wave function act like the wave function of a single particle. This is where one achieves Bose-Einstein condensation, opening the door to many quantum experiments on a macroscopic scale.

2.1.2 Vortices in Bose-Einstein Condensate

Similarly to fluid dynamics, where one can create a *vortex* by rotating the fluid in question, it is possible to create vortices in BEC. The velocity of the vortex flows around the center according to

$$\mathbf{v} \equiv \frac{\hbar}{M}\nabla\theta, \tag{2.1}$$

where θ is the phase of the vortex. The change in phase around a closed contour must be an integer multiple of 2π to conserve the boundary conditions of the vortex, so we can also state that

$$\Delta\theta = \oint_C \nabla\theta \cdot d\mathbf{l} = 2\pi\ell \tag{2.2}$$

Quantum vortices are different from their classical counterparts in that the *circulation* around a closed contour is quantized in units of h/m, such that

$$\Gamma \equiv \oint_C \mathbf{v} \cdot d\mathbf{l} = \frac{\hbar}{M} 2\pi\ell = \frac{h}{M}\ell, \tag{2.3}$$

where C is a closed circular path about the axis of cylindrical symmetry of the vortex and ℓ is the angular momentum quantum number of the vortex [72]. The integer value of ℓ is referred to as the *winding number* or *topological charge* of the vortex. Vortices in BECs [16] are analogous to vortices in a fluid, however, the velocity flow around the core is quantized in a quantum vortex, rather than allowing any value for the circulation [73].

2.1.3 Controlling Vortices in Bose-Einstein Condensates

The study of vortices in BECs is relatively new, so few practical applications have been realized. One of the main applications is in the field of atom optics. Atom optics is the study of the wavelike properties of a beam of particles. Much like a laser beam, coherent atom beams exhibit diffraction, interference, and various other optical phenomena. The uses of quantum and atom optics are showing improvements in communication, sensing, navigation, and quantum computing. Bose-Einstein condensates have already been generated directly on chips, so it is only a matter of time before we are creating integrated atom circuits for faster data transfer [74]. Vortices in BECs can be used for quantum computing [75]. Because of the stability of vortices in BEC, they are likely to be used in the future as qubits in quantum information processors [75]. However, means to control the vortices are still lacking. This thesis provides another avenue of vortex control. By having an analytical description of vortex trajectories after symmetry breaking, it is possible to generate several smaller vortices from one vortex by the action of an impulse, and know exactly where the

smaller vortices are going to go, as we develop in Sec. 5.3. By varying the symmetry of the impulse and the initial winding number of the vortex, we can create different patterns with the vortices, allowing us to send the vortices to definite locations.

2.1.4 Vortices in Superconductors

Superconductors are made of materials cooled below some critical temperature such that all electric resistance vanishes. This allows current to travel through the superconductors with no dissipation. Due to the Meissner effect [76], superconductors are unable to be manipulated by external magnetic fields. Type II superconductors get around this effect by using mixed states, including normal filaments surrounded by superconducting regions. This is called a vortex state. These vortices have superconducting currents surrounding the vortex core, allowing external magnetic fields to penetrate the material without destroying superconductivity [77].

The ability to control the behavior of these vortices with external magnetic fields and still be in a superconducting state suggest the possibility of creating a new generation of superconducting devices. Also, controlled vortices in superconductors can be applied in the construction of quiet circuits for sensing and communication, as well as large currents in high-field magnets [78].

2.2 Symmetry Breaking

When a system encounters a fluctuation that drives it past a critical point, the state of the system can suddenly change into a completely different structure. This process is known as spontaneous symmetry breaking. An important concept of symmetry breaking is that when a system of symmetry M undergoes an action of symmetry N, the system changes its symmetry from M to N. In this thesis, we break the symmetry of a singularity in an $O(2)$ fully symmetric medium using an impulse with symmetry C_4. Thus our post-action singularities are also C_4 symmetric. An

$O(2)$ symmetry means full rotational in two dimensions, i.e., if it is rotated in the plane of symmetry, it looks the same at all angles of rotation. An example of $O(2)$ symmetry is a circle. C_N symmetry is a discrete symmetry, meaning if the object is rotated $2\pi/N$ degrees, one recovers the initial view of the object. An example of C_4 symmetry would be a square, C_3 an equilateral triangle, etc.

2.3 Optical Vortices

The results of this thesis can easily be translated to the field of singular optics, where vortices in BEC are replaced with optical vortices. Optical vortices are circularly polarized beams of light with helical wave fronts, with a singularity in the center of the helix [79]. Because the phase is singular, and therefore undefined at this point, the amplitude of the beam vanishes at the center of the helix. By having a vanishing amplitude, optical vortices can be physical because the singular phase is canceled by zero amplitude. The amplitude of a beam with a vortex, in its simplest form, appears as a donut of intensity, with an empty center, as illustrated in Figure 2.4. Optical vortices are also known as screw dislocations and phase singularities.

When we calculate the trajectories of several singularities later in Sec. 5.2, we are actually tracking the center of the vortex where the singularity occurs. If we were to look at the amplitude, we would see small rings of intensity propagating either down a fiber (in the optical regime, as described here), or around a two-dimensional Bose-Einstein condensate (as we will study in this thesis). The number of phase windings in a single wavelength is known as the topological charge, or winding number [80]. Figure 2.5 shows the helical wave fronts of an optical vortex with winding number $\ell = 3$, like the one we will be using later in this thesis. A single wavelength is plotted, and there are three full rotations in the wave front. The sign of the topological charge determines which direction the beam rotates. Since the light wave is rotating, it can carry orbital angular momentum [81].

Figure 2.4: The amplitude of a vortex field is shaped similar to a donut to allow vortices to be physical. The amplitude must vanish at the center to allow a singular phase, hence the term singularity or vortex. The apparent height shown by false coloring represents the magnitude of the amplitude.

Optical vortices have numerous practical applications, including photonic crystals, laser trapping, material manipulation, and telecommunications [82].

2.3.1 Laser Trapping

Numerous breakthroughs have been made in biomedical research due to the ability to trap and study living cells, chromosomes, spermatozoa, and motor proteins [83, 84]. These traps are called optical tweezers, and are one of the most useful optical manipulation techniques. Optical tweezers can trap objects as small as 5 nanometers, so they are used heavily for the study of biological systems [85]. The ability of optical tweezers to precisely manipulate and transfer particles has led to their use in medical clinics for procedures such as *in vitro* fertilization [86]. Optical tweezers may be used in the future to modify chromosomes of living cells [87]. However, typical optical trapping using focused Gaussian beams has encountered problems. Due to the high intensity at the center of the trap, the trapped particles are susceptible

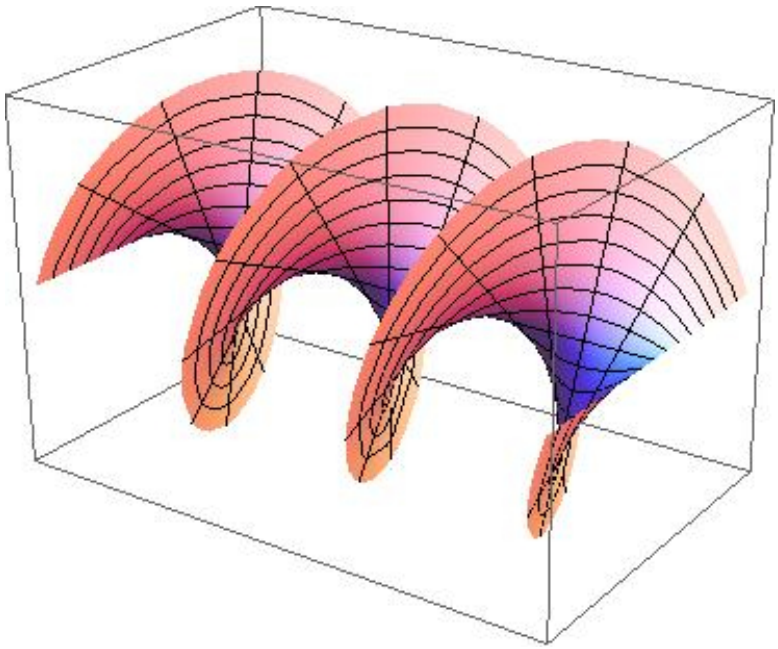

Figure 2.5: Visualization of the helical wave fronts of an optical vortex plotted in 3-D with winding number $\ell = 3$. A single wavelength is plotted, showing three distinct rotations in the wave front.

to damage by absorptive heating [83]. Typical particles that cannot be trapped by conventional optical tweezers are reflecting, absorbing, and low-dielectric constant materials [88, 89]. These materials are either easily damaged or repelled by the focus of typical tweezers. Optical vortices, with their donut shaped intensity profiles, remedy this problem. Large diameter dielectric particles are trapped in the center region of optical vortices rather than the high amplitude center used with typical optical tweezers to prevent damage. The smaller dielectric particles are trapped in the high points of the vortex amplitude [84], but are still undamaged due to the lower intensity. By creating patterns with the vortices, as one can do with the work in this thesis, particles can be confined to a distinct path of the user's choosing [90].

2.3.2 Material Manipulation and Telecommunications

Optical vortices are becoming more popular in trapping devices not only because they cause minimal heating damage, but also for the ability to rotate the trapped

particles [91] by taking advantage of the beam's inherent angular momentum [92, 93]. Photons in optical vortices carry orbital angular momentum of $l\hbar$ per photon, where the quantum angular momentum number ℓ is represented by the winding number of the beam [94]. The realization that photons carry well-defined orbital angular momentum associated to the helical wave fronts only furthers the connections between paraxial optics and quantum mechanics. This angular momentum also allows optical vortices to be used in quantum computing [95–97]. Because the states can be entangled [98], essentially creating an infinite-dimensional discrete Hilbert space, optical vortices can carry more than the typical 0 and 1 values of electronic computers [99, 100]. These entangled states have a tendency to annihilate when left to interact with the environment, so it is important to be able to control the vortices' interactions [101]. The work in this thesis provides further means of controlling vortices.

2.3.3 Photonic Crystals

Photonic crystals are periodic dielectric structures that manipulate photons much like semiconductors manipulate electrons. These photonic crystals have a band gap that filters light in a certain frequency range. The introduction of defects in a photonic crystal creates energy levels, allowing precise control of where and how light flows through the crystal [102]. However, conventional methods for creating defects are difficult to control. Defects are usually created via temperature quenching, mechanical stress, or phase transitions, but these naturally occurring defects tend to annihilate one another to reduce the elastic free energy in the system [82]. Optical vortices allow us to introduce defects to a crystal exactly where we want them to be. Because the vortices are user controlled, they do not annihilate one another. By manipulating crystals using optical vortices, we essentially create reconfigurable diffraction gratings. Photonic crystals have a plethora of uses, from redirecting cell phone radiation away

from the user's head, to reducing signal loss in hollow optical fibers [102].

2.3.4 Gradient Index Optics

The refractive index is a measure of what the speed of light will be in a given medium. Indices of refraction are usually thought to be homogeneous in a typical optical system. The way an optical system interacts with light depends on the value of the refractive index, the thickness of the material, and the curvature of the material's faces. However, it is possible to manufacture a material such that the index of refraction varies within the material itself [103]. Since light always takes the path of least time [104], the variation of the refractive index in a given material controls the path of the light beam. These specifically manufactured materials are called Gradient Index components, or GRIN mediums. A beam of light propagating through an inverted quadratic GRIN fiber converges at a focal point further down the axis of propagation. The beam then diverges past the focal point, only to be refocused by the GRIN medium again. This process is repeated over and over, revealing a periodic propagation pattern [81], as depicted below.

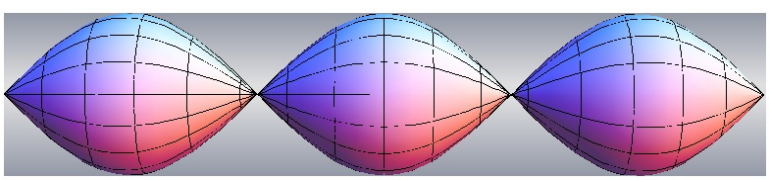

Figure 2.6: Due to the varying index of refraction in an inverted quadratic GRIN medium, light diverges and reconverges in an oscillatory manner. This periodic structure makes GRIN mediums analogous to the quantum harmonic oscillator.

By using GRIN materials in optical systems, we can set up experiments that are closely analogous to quantum experiments. For example, in this thesis we will be using a harmonic potential to trap a Bose-Einstein condensate. The optical analog of a harmonic trap is a quadratically varying GRIN fiber. Where we would normally use the Schrödinger equation in quantum mechanics, we use the Helmholtz equation

for optics [105] to mathematically describe our system. The square of the refractive index profile plays the same role as the potential profile in the Schrödinger equation. Due to the close analogy between theories, the results of this thesis can be directly applied to optics just by changing a few fundamental constants.

2.4 Previous Work

When an optical vortex encounters an infinitesimally thin discretely symmetric diffraction grating, the symmetry of the initial vortex is broken into the symmetry of the grating. For a vortex in a constant potential (homogeneous medium), it has been shown that the initial vortex is broken into N off-axis singularities and a single singularity at the origin [61]. After returning to the homogeneous fiber, one would expect the singularities to show trivial motion due to the lack of external forces. However, this was not the case. The off-axis singularities were seen to travel away from the origin and rotate about the axis of symmetry before settling into far-field straight asymptotic trajectories. By calculating the equations of motion for the singularities, it was observed that the singularities experienced effective external forces, even though none were present. The diffraction grating imprinted the peculiar motion onto the singularities when the symmetry was broken. A full study for the constant potential case can be found in [61]. The same phenomena is expected to be seen for a vortex in a harmonic potential or GRIN medium. This thesis explores the effect of an instantaneous discretely symmetric impulse on a singularity in an ideal BEC trapped by a harmonic potential. Due to the mathematical similarities between optics and BEC, the work in this thesis and in [61] can be applied to both fields of study.

2.5 Current Work

To set the stage for the current work, we must first introduce the Gross-Pitaevskii equation as it applies for weakly interacting Bose-Einstein condensates.

2.5.1 Gross-Pitaevskii Equation

In a dilute BEC, the separation between particles is much larger than the length scales associated with particle-particle interactions. Due to this separation of scales, the two-body interactions are much more prevalent than three-or-more-body interactions. Low-energy particles cannot overcome the centrifugal barrier for partial waves of p symmetry and above. Thus, if we analyze the two-body interaction using scattering theory for low-energy particles, we see that it is sufficient to consider only s-wave scattering, which is spherically symmetrical. This simplification for low-energy particles allows us to describe the system entirely in terms of the scattering length, a. By considering only s-wave scattering and using the Born approximation, we find that the effective two-particle interaction can be described entirely by the scattering length for the potential:

$$V_{\text{eff}}(\mathbf{r},\ \mathbf{r}') = \frac{4\pi a\hbar^2}{m}\delta(\mathbf{r}-\mathbf{r}') = g_{3\text{D}}\delta(\mathbf{r}-\mathbf{r}'), \tag{2.4}$$

where $g_{3\text{D}}$ is known as the coupling constant, or *nonlinearity* of the system. If we include the previous potential in the Hamiltonian for a system of particles,

$$H = \sum_{i=1}^{N}\left(\frac{\mathbf{p}_i^2}{2m} + V(\mathbf{r}_i)\right) + g_{3\text{D}}\sum_{i<j}\delta(\mathbf{r}_i - \mathbf{r}_j). \tag{2.5}$$

By averaging over the many-body quantum interactions using the mean-field approximation, we arrive at the Gross-Pitaevskii equation [106]:

$$i\hbar\frac{\partial}{\partial t}\psi(\mathbf{r},t) = \left(-\frac{\hbar^2}{2m}\nabla^2 + V_{\text{ext}}(\mathbf{r}) + g_{3\text{D}}|\psi(\mathbf{r},t)|^2\right)\psi(\mathbf{r},t). \tag{2.6}$$

2.5.2 Two-Dimensional Bose-Einstein Condensate and Symmetry Breaking Potential

Let us now consider a Bose-Einstein condensate with the axial frequency set much higher than the transverse trapping frequencies, making our BEC effectively two-dimensional. When working in two-dimensions, we must renormalize the nonlinearity according to [107], thus allowing us to express the nonlinearity as $g_{2\mathrm{D}} = a\sqrt{8\pi\hbar^3\omega_z/M}$ or g for simplicity, as will be used for the rest of this thesis. We also make the assumption that the time scale for interactions is much larger than the time scale of the symmetry breaking process. This assumption allows us to study the system as though it were indeed non-interacting.

We must first note that each term in (2.6) has a time scale associated with it. The transverse potential has a time $t_{\mathrm{pot}} \sim 2\pi/\omega$. The symmetry breaking potential has a time Δt. The nonlinearity has a time t_{nonlin}. The kinetic energy or dispersion $\hbar^2/2mL^2$ has a time

$$t_{\mathrm{lin}} = \hbar/E_{\mathrm{kin}}, \tag{2.7}$$

where $E_{\mathrm{kin}} \simeq \hbar^2/2mL^2$. L is the harmonic oscillator length, defined by $L \equiv \sqrt{\hbar/m\omega}$. So, $t_{\mathrm{lin}} \simeq 2/\omega$, showing that t_{lin} and t_{pot} are on the same order.

The interaction time can be found by units considerations. To show this, we begin by stating the units of several variables, where E is the unit of energy and L is the unit of length, and the square brackets indicate units:

$$\begin{aligned} [g_{2\mathrm{D}}] &= [E][L]^2, \\ [|\psi_{2\mathrm{D}}|^2] &= \frac{1}{[L]^2}, \\ [\hbar] &= [E][t]. \end{aligned} \tag{2.8}$$

We can then show that

$$[t] = \frac{[\hbar]}{[E]} = \frac{[\hbar][L]^2}{[g_{2\mathrm{D}}]}, \tag{2.9}$$

$$t_{\mathrm{nonlin}} = \frac{\hbar}{\bar{n}_{2\mathrm{D}} g_{2\mathrm{D}}}, \tag{2.10}$$

where $\bar{n}_{2\mathrm{D}} = 1/L^2 \int_{-L/2}^{L/2} dxdy|\psi_{2\mathrm{D}}|^2$ is the mean particle density in two-dimensions.

Now let us consider a stationary singularity state in the BEC, with an integer winding number that is greater than 1. Because the singularity wave function must be the same at $\theta = 0$ and at $\theta = 2\pi$, the winding number is always an integer, as explained in Sec. 2.1.2. We are interested in the effect of a discretely symmetric impulse on the parent singularity. We describe this impulse by the potential profile,

$$V(\mathbf{x},\, t) = \begin{cases} V_0(\mathbf{x}) & 0 \leq t < t_0, \\ V_0(\mathbf{x}) + \Delta V(\mathbf{x}) & t_0 \leq t < t_1 = t_0 + \Delta t, \\ V_1(\mathbf{x}) & t_1 \leq t. \end{cases} \tag{2.11}$$

where $\mathbf{x}$ is the two-dimensional position vector $(x,\ y)$, We assume that the second interval of time describing the impulse has a very small duration, so that $\Delta t/t_{\mathrm{nonlin}} \ll 1$. Mathematically, the impulse is described by the Dirac delta function, where the area of the impulse, $\Delta V \Delta t$, is described by the limits $\lim_{\Delta V \to \infty} \Delta V \Delta t =$ constant and $\lim_{\Delta t \to 0} \Delta V \Delta t =$ constant. The impulse potential, given by ΔV, is taken to have C_4 symmetry so we can observe the effects of a symmetry breaking impulse on a singularity. We can utilize this limit to erase all time dependence from the symmetry breaking potential, taking $\Delta V \Delta t$ to be constant. If this limit fails, the time dependence inherent in an ever-widening delta function will significantly alter the physics of the singularity trajectories. We explore this limit with numerical data in chapter 7. The first and last regions are described by the fully symmetric trapping harmonic potential, so V_0 and V_1 are identical, and will henceforth be referred to as

simply V. The impulse ΔV will be described in more detail later. If this impulse has discrete symmetry, i.e., it is invariant under the action of the C_4 rotation group, it will break the symmetry of the fully symmetric singularity into C_4. After this symmetry breaking impulse occurs, the parent singularity is disassociated into a cluster of singly charged singularities. Our goal is to find the trajectories of these singularities and study their dynamics and validity when applied to a nonlinear BEC.

CHAPTER 3

MATHEMATICAL DESCRIPTION OF A SINGULARITY IN A NON-INTERACTING BOSE-EINSTEIN CONDENSATE WITH A HARMONIC POTENTIAL

In this chapter, we present the necessary background mathematics for the calculations that take place in this thesis.

3.1 The Harmonic-Oscillator Propagator

A non-interacting BEC in a harmonic trap can be treated using the single particle wave function. The single particle wave function is the solution to the Schrödinger equation, which can be recovered from the Gross-Pitaevskii equation given in (2.6) by taking the nonlinearity g to be negligible. We begin by treating the one-dimensional case for heuristic purposes, and will generalize to more dimensions later.

$$i\hbar\frac{\partial\psi(x,\,t)}{\partial t} = H\psi(x,\,t). \tag{3.1}$$

Since we will be working in a harmonic trap, we use the harmonic oscillator Hamiltonian [108]

$$H = -\frac{\hbar^2}{2m}\frac{\partial^2}{\partial x^2} + \frac{1}{2}m\omega^2 x^2. \tag{3.2}$$

The solutions to the Schrödinger equation describe the time and spatial evolution of a system. However, our goal is to study both the time and spatial evolution of our singularity state. To do this, we use a *propagator*. The propagator allows us to take some arbitrary initial wave function $\psi(x_0,\,t_0)$, and evolve the initial state from one point in space to another at some different time. We derive the harmonic-oscillator propagator here. For clarity, we proceed in Dirac notation.

3.1.1 General Propagation

We begin by assuming the initial wave function can be expanded into a superposition of the eigenstates of the harmonic-oscillator Hamiltonian [109], such that

$$|\psi(t_0)\rangle = \sum_{n=0}^{\infty} a_n |\phi_n\rangle, \tag{3.3}$$

where a_n are the eigenvalues and $|\phi_n\rangle$ are the eigenkets of H. Currently, we do not know what the eigenvalues are for our arbitrary wave function, so we are going to solve for them in terms of the known eigenkets and the wave function. If we take the scalar product of $|\psi(t_0)\rangle$ with one of the eigenkets, $|\phi_m\rangle$, we can solve directly for a_m,

$$\langle\phi_m|\psi(t_0)\rangle = \sum_{n=0}^{\infty} a_n \langle\phi_m|\phi_n\rangle. \tag{3.4}$$

Since the eigenkets are orthogonal and normalized, $\langle\phi_m|\phi_n\rangle = 0$ for all values of $n \neq m$, and 1 for $n = m$. Thus, our sum turns into

$$\begin{aligned} \langle\phi_m|\psi(t_0)\rangle &= \sum_{n=0}^{\infty} a_n \langle\phi_m|\phi_n\rangle \\ &= a_m \langle\phi_m|\phi_m\rangle \\ &= a_m. \end{aligned} \tag{3.5}$$

So, rewriting (3.3) with our newly solved value of a_n yields

$$|\psi(t_0)\rangle = \sum_{n=0}^{\infty} \langle\phi_n|\psi(t_0)\rangle |\phi_n\rangle. \tag{3.6}$$

In order to evaluate the inner product of $|\phi_n\rangle$ with $|\psi(t_0)\rangle$, we insert a resolution of the identity in terms of a complete set of position eigenkets to project the state

vectors into position space, in the form [110]

$$|\psi(t_0)\rangle = \sum_{n=0}^{\infty} \int_{-\infty}^{\infty} dx_0 \, \langle \phi_n | x_0 \rangle \langle x_0 | \psi(t_0) \rangle | \phi_n \rangle. \tag{3.7}$$

The previous equation gives us a means to propagate $\psi(t_0)$ to a new position x, but what about to a future time t? To propagate $\psi(t_0)$ forward in time, we need to introduce time-dependent coefficients to the sum in (3.3). Thus, we get

$$\begin{aligned} |\psi(t)\rangle &= \sum_{n=0}^{\infty} a_n c_n(t) |\phi_n\rangle \\ &= \sum_{n=0}^{\infty} c_n(t) \langle \phi_n | \psi(t_0) \rangle | \phi_n \rangle \\ &= \sum_{n=0}^{\infty} \int_{-\infty}^{\infty} dx_0 \, \langle \phi_n | x_0 \rangle \langle x_0 | \psi(t_0) \rangle | \phi_n \rangle c_n(t). \end{aligned} \tag{3.8}$$

For the harmonic oscillator, we take the set of $|\phi_n\rangle$ to be harmonic oscillator eigenstates, and use the time-dependent coefficients $c_n(t)$, which are given by

$$c_n(t) = e^{-i\omega(n+1/2)(t-t_0)}, \tag{3.9}$$

where ω is the frequency of the harmonic oscillator. If we take the inner product of x with (3.8) , we get our final expression for $\psi(x,\, t)$:

$$\langle x | \psi(t) \rangle = \sum_{n=0}^{\infty} \int_{-\infty}^{\infty} dx_0 \, \langle \phi_n | x_0 \rangle \langle x_0 | \psi(t_0) \rangle \langle x | \phi_n \rangle e^{-i\omega(n+1/2)(t-t_0)}, \tag{3.10}$$

or, in functional form,

$$\psi(x,\, t) = \sum_{n=0}^{\infty} \int_{-\infty}^{\infty} dx_0 \, \phi_n^*(x_0) \psi(x_0,\, t_0) \phi_n(x) e^{-i\omega(n+1/2)(t-t_0)}. \tag{3.11}$$

3.1.2 Hermite Polynomials and the Propagator

To further simplify (3.11), we need to insert the stationary states, $\phi_n(x)$. It is easiest to introduce dimensionless variables at this time. Let us define

$$L \equiv \sqrt{\frac{\hbar}{m\omega}}, \tag{3.12}$$

$$\tilde{x} \equiv \frac{x}{L} \text{ and } \tilde{y} \equiv \frac{y}{L} \tag{3.13}$$

Using these dimensionless variables, we take the stationary states of the harmonic oscillator given in terms of Hermite polynomials [110]:

$$\phi_n(\tilde{x}) = \frac{1}{\sqrt{n!2^n}} \left(\frac{1}{\pi}\right)^{1/4} H_n(\tilde{x}) e^{-\tilde{x}^2/2}. \tag{3.14}$$

If we plug these wave functions into (3.11), we get

$$\psi(\tilde{x},\ t) = \sum_{n=0}^{\infty} \int_{-\infty}^{\infty} d\tilde{x}_0\, \psi(\tilde{x}_0,\ t_0) e^{-i\omega(n+1/2)(t-t_0)} \frac{1}{2^n n! \sqrt{\pi}} H_n(\tilde{x}) H_n(\tilde{x}_0) e^{-(\tilde{x}_0^2+\tilde{x}^2)/2}. \tag{3.15}$$

If we define

$$W(\tilde{x},\ \tilde{x}_0,\ t) = \sum_{n=0}^{\infty} \frac{H_n(\tilde{x}) e^{-\tilde{x}^2/2} H_n(\tilde{x}_0) e^{-\tilde{x}_0^2/2}}{2^n n! \sqrt{\pi}} T^n, \tag{3.16}$$

where

$$T \equiv e^{-i\omega(t-t_0)}, \tag{3.17}$$

we can simplify the expression for $\psi(\tilde{x},\ t)$ significantly. The integral form of the Hermite polynomials is given by

$$H_n(\tilde{x}) = \frac{2^n (-i)^n e^{\tilde{x}^2}}{\sqrt{\pi}} \int_{-\infty}^{\infty} du\, u^n e^{2i\tilde{x}u - u^2}. \tag{3.18}$$

If we substitute this expression into (3.16) and simplify, we find

$$\begin{aligned}
W(\tilde{x},\, \tilde{x}_0,\, t) &= e^{(\tilde{x}^2+\tilde{x}_0^2)/2}\pi^{-3/2}\sum_{n=0}^{\infty}\frac{-T^n 2^n}{n!}\int_{-\infty}^{\infty}du\int_{-\infty}^{\infty}dv\; u^n v^n e^{2i\tilde{x}u-u^2}e^{2i\tilde{x}_0 v-v^2} \\
&= e^{(\tilde{x}^2+\tilde{x}_0^2)/2}\pi^{-3/2}\int_{-\infty}^{\infty}du\int_{-\infty}^{\infty}dv\sum_{n=0}^{\infty}\frac{-T^n 2^n u^n v^n}{n!}e^{2iyu-u^2+2iy_0 v-v^2} \\
&= e^{(\tilde{x}^2+\tilde{x}_0^2)/2}\pi^{-3/2}\int_{-\infty}^{\infty}du\int_{-\infty}^{\infty}dv\; e^{-2Tuv}e^{-u^2-v^2+2i\tilde{x}u+2i\tilde{x}_0 v} \\
&= e^{(\tilde{x}^2+\tilde{x}_0^2)/2}\pi^{-3/2}\int_{-\infty}^{\infty}dv\; e^{-v^2+2i\tilde{x}_0 v}\int_{-\infty}^{\infty}du\; e^{-u^2-2u(Tv-i\tilde{x})}. \qquad (3.19)
\end{aligned}$$

The u integral can be carried out by noting that

$$\int_{-\infty}^{\infty}dx\; e^{-a^2x^2-2bx} = \frac{\sqrt{\pi}}{a}e^{b^2/a^2},\;\; \mathrm{Re}(a^2)>0, \qquad (3.20)$$

which will give us

$$\begin{aligned}
W(\tilde{x},\, \tilde{x}_0,\, t) &= e^{(\tilde{x}^2+\tilde{x}_0^2)/2}\pi^{-3/2}\int_{-\infty}^{\infty}dv\; e^{-v^2+2i\tilde{x}_0 v}\left(\sqrt{\pi}\, e^{(Tv-i\tilde{x})^2}\right) \\
&= \frac{e^{(\tilde{x}_0^2+\tilde{x}^2)/2}}{\pi}\int_{-\infty}^{\infty}dv\; e^{T^2v^2-2i\tilde{x}Tv-\tilde{x}^2}e^{-v^2+2i\tilde{x}_0 v} \\
&= \frac{e^{(\tilde{x}_0^2-\tilde{x}^2)/2}}{\pi}\int_{-\infty}^{\infty}dv\; e^{-v^2(1-T^2)-2iv(\tilde{x}T-\tilde{x}_0)}. \qquad (3.21)
\end{aligned}$$

If we carry out the v integral using (3.20),

$$\begin{aligned}
W(\tilde{x},\, \tilde{x}_0,\, t) &= \frac{e^{(\tilde{x}_0^2-\tilde{x}^2)/2}}{\sqrt{\pi(1-T^2)}}\exp\left[-\frac{(\tilde{x}T-\tilde{x}_0)^2}{1-T^2}\right] \\
&= \frac{1}{\sqrt{\pi(1-T^2)}}\exp\left[-\frac{1}{2}(\tilde{x}^2+\tilde{x}_0^2)\frac{1+T^2}{1-T^2}+2\tilde{x}\tilde{x}_0\frac{T}{1-T^2}\right]. \qquad (3.22)
\end{aligned}$$

If we look back at (3.15), we can use our simplified $W(\tilde{x},\ \tilde{x}_0,\ t)$ function to simplify, giving us

$$\begin{aligned}
\psi(\tilde{x},\ t) &= \sum_{n=0}^{\infty} \int_{-\infty}^{\infty} d\tilde{x}_0\, \psi(\tilde{x}_0,\ t_0) e^{-i\omega(n+1/2)(t-t_0)} \frac{1}{2^n n! \sqrt{\pi}} H_n(\tilde{x}) H_n(\tilde{x}_0) e^{-(\tilde{x}_0^2+\tilde{x}^2)/2} \\
&= \int_{-\infty}^{\infty} d\tilde{x}_0\, \psi(\tilde{x}_0,\ t_0) e^{-i\omega(t-t_0)/2} W(\tilde{x},\ \tilde{x}_0,\ t) \\
&= \int_{-\infty}^{\infty} d\tilde{x}_0\, \psi(\tilde{x}_0,\ t_0) T^{1/2} W(\tilde{x},\ \tilde{x}_0,\ t) \\
&= \int_{-\infty}^{\infty} d\tilde{x}_0\, \psi(\tilde{x}_0,\ t_0) \sqrt{\frac{T}{\pi(1-T^2)}}\, \exp\left[-\frac{1}{2}(\tilde{x}^2+\tilde{x}_0^2)\frac{1+T^2}{1-T^2} + 2\tilde{x}\tilde{x}_0 \frac{T}{1-T^2}\right].
\end{aligned} \tag{3.23}$$

We can simplify the arguments of the exponentials by using trigonometry identities

$$i\frac{1+T^2}{1-T^2} = i\frac{1+e^{-2i\omega(t-t_0)}}{1-e^{-2i\omega(t-t_0)}} = \frac{\cos\omega(t-t_0)}{\sin\omega(t-t_0)} \tag{3.24}$$

and

$$\frac{1-T^2}{2iT} = \frac{1-e^{-2i\omega(t-t_0)}}{2ie^{-i\omega(t-t_0)}} = \sin\omega(t-t_0). \tag{3.25}$$

Our propagated wave function over time then becomes

$$\begin{aligned}
\psi(\tilde{x},\ t) = &\int_{-\infty}^{\infty} d\tilde{x}_0\, \psi(\tilde{x}_0,\ t_0) \frac{1}{\sqrt{2i\pi \sin\omega(t-t_0)}} \\
&\times \exp\left\{\frac{i}{2\sin\omega(t-t_0)}[(\tilde{x}^2+\tilde{x}_0^2)\cos\omega(t-t_0) - 2\tilde{x}\tilde{x}_0]\right\}.
\end{aligned} \tag{3.26}$$

This is the dimensionless harmonic-oscillator propagator in one dimension. To extend this propagator to more dimensions, we multiply them together [111], such that

$$\begin{aligned}
\psi(\tilde{\mathbf{x}},\ t) = &\prod_{s=1}^{N} \int_{-\infty}^{\infty} d\tilde{x}_s\, \psi(\tilde{x}_{0s},\ t_0) \left[\frac{1}{2i\pi \sin\omega_s(t-t_0)}\right]^{1/2} \times \\
&\exp\left\{\frac{i}{2\sin\omega_s(t-t_0)}[(\tilde{x}_s^2+\tilde{x}_{0s}^2)\cos\omega_s(t-t_0) - 2\tilde{x}_s\tilde{x}_{0s}]\right\},
\end{aligned} \tag{3.27}$$

where ω_s is the harmonic trap frequency in the s dimension. We will use dimensionless units throughout the entire thesis, so $\tilde{x}$ and $\tilde{y}$ are understood to be dimensionless.

3.1.3 Test Cases

If we take the ground state wave function of the one-dimensional harmonic oscillator [110], given by

$$\psi(\tilde{x}) = \left(\frac{1}{\pi}\right)^{1/4} e^{-\tilde{x}^2/2} \tag{3.28}$$

we can demonstrate that the ground state is in fact a stationary state. We demonstrate this property of the ground state by inserting the wave function into (3.26), which gives the expression for $\psi(\tilde{x},\ t)$:

$$\begin{aligned}\psi(\tilde{x},\ t) = \int_{-\infty}^{\infty} d\tilde{x}_0 \ \left(\frac{1}{\pi}\right)^{1/4} \sqrt{\frac{1}{2i\pi\sin(\omega t)}} e^{-\tilde{x}_0^2/2} \\ \times \exp\left\{\frac{i}{2\sin(\omega t)}[(\tilde{x}^2+\tilde{x}_0^2)\cos(\omega t) - 2\tilde{x}\tilde{x}_0]\right\}.\end{aligned} \tag{3.29}$$

If we proceed with the integration, we see that

$$\begin{aligned}\psi(\tilde{x},\ t) &= \left(\frac{1}{\pi}\right)^{1/4} \sqrt{\frac{1}{2i\pi\sin(\omega t)}} \int_{-\infty}^{\infty} d\tilde{x}_0 \ e^{-\tilde{x}_0^2/2} \exp\left\{\frac{i}{2\sin(\omega t)}[(\tilde{x}^2+\tilde{x}_0^2)\cos(\omega t) - 2\tilde{x}\tilde{x}_0]\right\} \\ &= \left(\frac{1}{\pi}\right)^{1/4} \sqrt{\frac{1}{2i\pi\sin(\omega t)}} \sqrt{\frac{2\pi}{[1-i\cot(\omega t)]}} e^{-\tilde{x}^2/2} \\ &= \left(\frac{1}{\pi}\right)^{1/4} e^{-\tilde{x}^2/2} \sqrt{\frac{1}{i\sin(\omega t)+\cos(\omega t)}} \\ &= \left(\frac{1}{\pi}\right)^{1/4} e^{-\tilde{x}^2/2} \exp\left(\frac{-i\omega t}{2}\right) \\ &= \psi(\tilde{x},\ 0)\exp\left(-\frac{i\omega t}{2}\right) \\ &= \psi(\tilde{x},\ 0)e^{-iE_0 t},\end{aligned} \tag{3.30}$$

where E_0 is the ground state energy $E_0 \equiv 1/2$ in dimensionless units. This equation is consistent with the unitary time-evolution operator formulated from the Schrödinger equation [110], which confirms that the spatial propagator returns the same result as the more direct evolution operator when all spatial dependence is removed. We can directly demonstrate how the propagator evolves a wave function spatially by using a superposition of eigenstates of the harmonic oscillator. Let us consider the wave function created by a superposition of the ground state and the first excited state of the harmonic oscillator,

$$\psi(\tilde{x},\ t) = \frac{1}{2}\left(\frac{1}{\pi}\right)^{1/4} e^{-\tilde{x}^2/2}(\sqrt{2} + 2x). \tag{3.31}$$

If we insert this equation into the propagator given in (3.26) and simplify, we see that the future wave function is now

$$\psi(\tilde{x},\ t) = \frac{1}{2}\left(\frac{1}{\pi}\right)^{1/4} e^{-\tilde{x}^2/2}(\sqrt{2}e^{-it/2} + 2xe^{-3it/2}), \tag{3.32}$$

which is exactly what results when using the time evolution operator. Evidently, the use of the time evolution operator and the Feynman propagator result in the same wave function. However, the propagator is more straightforward for arbitrary wave functions where one does not know how to write it as a superposition state. It turns out that the probability distribution given by this wave function is varying spatially in time, so the actually beating between states is clearly visible. We plot several time steps in Figure 3.1 to demonstrate.

3.2 The Unitary Time-Evolution Operator

The unitary time-evolution operator is a postulate of quantum mechanics. It provides a means to take the initial state of a wave function and propagate it to a

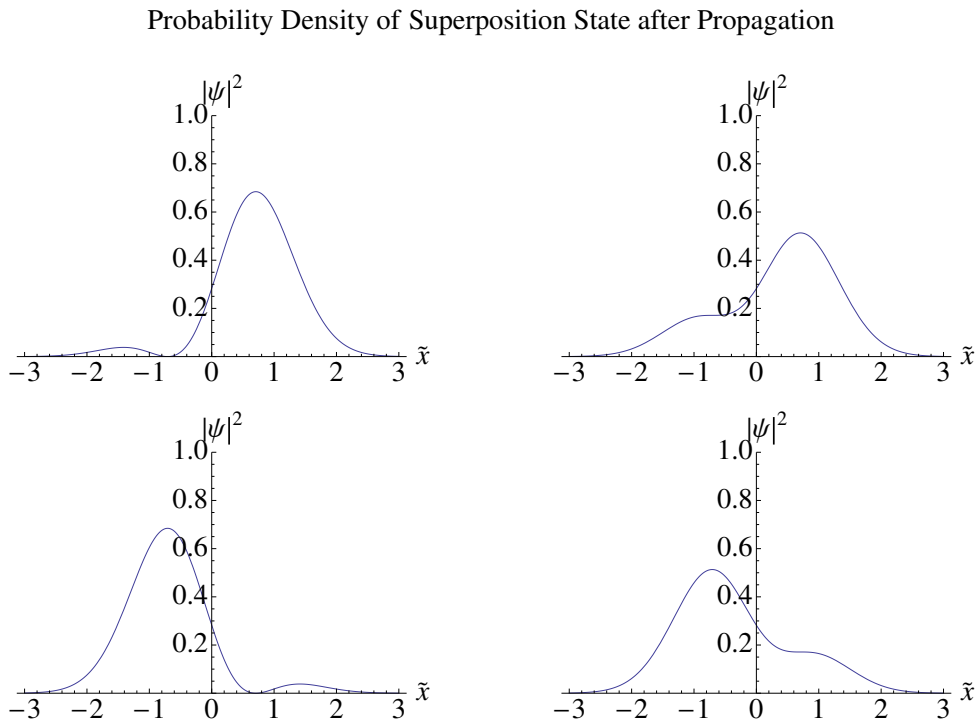

Figure 3.1: A parent singularity of winding number $\ell = 3$ is imprinted by a C_4 discretely symmetric impulse. This symmetry breaking process will result in five daughter singularities, one at the origin of winding number $m = -1$, and four off-axis of winding number $m = 1$.

future time t using the particle's Hamiltonian. It is given by [110]

$$\psi(\mathbf{x},\ t) = e^{-i\hat{H}_0(t-t_0)/\hbar}\psi(\mathbf{x},\ t_0). \tag{3.33}$$

In most cases, t_0 is taken to be 0, so

$$\psi(\mathbf{x},\ t) = e^{-i\hat{H}_0 t/\hbar}\psi(\mathbf{x},\ 0). \tag{3.34}$$

For stationary states, i.e. when the wave function has separable spatial and temporal components, the operation of the time evolution operator on the stationary state will evolve the state in time only. For non-stationary states, the operation of the time evolution operator will evolve the state in time and space. We will use the time evolution operator to evolve the initial singularity state through the symmetry

breaking impulse. We then use the full Feynman propagator to find the solution to (2.6) for a future time and new position.

3.2.1 Symmetry Breaking Case

In this thesis, we will be using the two-dimensional propagator to evolve our initial singularity in the transverse plane. Before we continue, let us remember the dimensionless variables used previously:

$$\omega t \equiv \tau, \ \sqrt{\frac{\hbar}{m\omega}} \equiv L, \text{ and } \tilde{x} = \frac{x}{L} \tag{3.35}$$

In two dimensions, the wave function in (3.26) becomes

$$\begin{aligned}\psi(\tilde{\mathbf{x}},\, t) =& \frac{1}{2i\pi \sin\tau} \exp\left[\frac{i\cos\tau(\tilde{x}^2+\tilde{y}^2)}{2\sin\tau}\right] \int_{-\infty}^{\infty} d\tilde{x}' \int_{-\infty}^{\infty} d\tilde{x}'\ \psi(\tilde{\mathbf{x}}',\, \tau') \\ &\times \exp\left\{\frac{i}{2\sin\tau}\left[(\tilde{x}'^{\,2}+\tilde{y}'^{\,2})\cos\tau - 2(\tilde{x}\tilde{x}'+\tilde{y}\tilde{y}')\right\}\right]\end{aligned} \tag{3.36}$$

for $t \geq 0$.

CHAPTER 4

EFFECT OF AN IMPULSE DURING PROPAGATION

The goal of this research is to determine what happens to a singularity in a BEC when it is "shocked" by an instantaneous symmetry breaking potential. To analyze the potential profile given by equation (2.11), we first assume that the second region describing the impulse is very short, so that $\Delta t \ll 1$. Since we are making the assumption that the impulse is instantaneous, we can evolve our singularity through the impulse by using the spatially invariant unitary time-evolution operator, rather than a propagator.

4.1 Evolution Operator

The evolution operator for a wave function can be expressed by $e^{i\hat{H}\tau}$ [110], where τ is the dimensionless time variable $\tau \equiv \omega t$, as described in Sec. 3.2. For this potential profile, we can decompose the evolution operator into three separate operators, one for each region, according to

$$e^{i\hat{H}\tau} = e^{i\hat{H}(\tau-\tau_1)} e^{i\hat{H}\Delta\tau} e^{i\hat{H}\tau_0}. \tag{4.1}$$

Now, $\hat{H} = \hat{H}_0 + \Delta\hat{V}$, where $\hat{H}_0$ is the initial Hamiltonian of the harmonic oscillator given in (3.2), and $\Delta\hat{V}$ is the symmetry breaking potential, both in dimensionless units. According to the potential profile given in (2.11), the evolution operator can be rewritten as

$$e^{i\hat{H}\tau} = e^{i\hat{H}_0(\tau-\tau_1)} e^{i(\hat{H}_0+\Delta\hat{V})\Delta\tau} e^{i\hat{H}_0\tau_0}. \tag{4.2}$$

Let us analyze the evolution operator for the impulse. Since $\Delta\tau \ll 1$, we can apply the Hausdorff-Campbell decomposition [112] via the Zassenhaus formula to lowest

order, given by

$$e^{t(\hat{X}+\hat{Y})} = e^{t\hat{X}} e^{t\hat{Y}} e^{-t^2\left[\hat{X},\,\hat{Y}\right]/2} \tag{4.3}$$

in order to get

$$e^{i(\hat{H}_0+\Delta\hat{V})\Delta\tau} = e^{i\hat{H}_0\Delta\tau} e^{i\Delta\hat{V}\Delta\tau} + O(\Delta\tau^2) = e^{i\Delta\hat{V}\Delta\tau} e^{i\hat{H}_0\Delta\tau} + O(\Delta\tau^2), \tag{4.4}$$

where the two orders of the operators are possible since they commute with $O(\Delta\tau^2)$. The full evolution operator is then given by

$$e^{i\hat{H}\tau} = e^{i\hat{H}_0(\tau-\tau_1)} e^{i\Delta\hat{V}\Delta\tau} e^{i\hat{H}_0\Delta\tau} e^{i\hat{H}_0\tau_0} = e^{i\hat{H}_0(\tau-\tau_1)} e^{i\Delta\hat{V}\Delta\tau} e^{i\hat{H}_0(\tau_0+\Delta\tau)}. \tag{4.5}$$

If we take into account that $\tau_1 = \tau_0 + \Delta\tau$, we find

$$e^{i\hat{H}\tau} = e^{i\hat{H}_0(\tau-\tau_1)} e^{i\Delta\hat{V}\Delta\tau} e^{i\hat{H}_0\tau_1}. \tag{4.6}$$

If we apply this operator to an initial wave function, we see that

$$|\phi(\tau)\rangle = e^{i\hat{H}_0(\tau-\tau_1)} e^{i\Delta\hat{V}\Delta\tau} e^{i\hat{H}_0\tau_1} |\phi(0)\rangle = e^{i\hat{H}_0(\tau-\tau_1)} e^{i\Delta\hat{V}\Delta\tau} |\phi(\tau_1)\rangle. \tag{4.7}$$

It turns out that the presence of an impulse at time τ_1 only produces a multiplication by the diagonal operator in position space, $e^{i\Delta\hat{V}\Delta\tau}$. If we define

$$\bar{\phi}(\tau_1) = e^{i\Delta\hat{V}\Delta\tau} |\phi(\tau_1)\rangle, \tag{4.8}$$

the resulting amplitude can be propagated to future times using the unitary time-evolution operator from Sec. 3.2 in the final potential $e^{i\hat{H}_0(\tau-\tau_1)}$.

4.2 Impulse Potential with Discrete Rotational Symmetry

In this section, we analyze the effect of an impulse having rotational symmetry of finite order. This means that $\Delta\hat{V}$ is invariant under the action of the elements of a discrete rotational group C_N. The operation of C_N on $\Delta\hat{V}$ returns the original potential when rotated π/N radians. To simplify the analysis, we assume that the original medium has continuous rotational symmetry, $O(2)$. This restricts our harmonic trap such that the trapping frequencies $\omega_x = \omega_y$. Mathematically, we express the invariance property of the impulse as

$$\Delta V(G\tilde{\mathbf{x}}) = \Delta V(\tilde{\mathbf{x}}) \quad \forall G \in C_N. \tag{4.9}$$

This property determines the functional form of the potential close to the rotation axis. It is convenient to introduce a complex notation for the spatial coordinates such that $\chi = \tilde{x} + i\tilde{y}$. Close to the origin, $|\chi|^2 = \tilde{x}^2 + \tilde{y}^2 \approx 0$ so we can perform a Taylor expansion of the evolution operator in (4.8) in the complex variable χ and keep the lower order terms. Because of the C_N invariance of the potential, there are only two types of C_N-invariant products of χ and χ^* that can appear in this Taylor expansion: $\chi\chi^* = |\chi|^2 = \tilde{x}^2 + \tilde{y}^2$, χ^N, and χ^{*N}. As a concrete example of our symmetry breaking procedure, we will study one of the simplest cases corresponding to discrete rotational symmetry of order $N = 4$. If we perform a Taylor expansion on the arbitrary impulse function $V(\chi)$ in both variables and keep the allowed terms mentioned previously, the potential of the impulse can be expanded to read

$$\Delta V(\chi) = u_0 + u_1|\chi|^2 + u_2|\chi|^4 + v_0\chi^4 + v_1\chi^{*4} + O(\chi^6), \tag{4.10}$$

where u_0, u_1, u_1, v_0 and v_1 are constants. In order for this expansion to be valid, $\Delta V(\chi)$ must be real, and the constants v_0 and v_1 must be equal and real, which we

state specifically later after Eq. (5.23). This potential presents the most general form of a C_4 invariant potential close to the symmetry axis. Since we assume that the first medium is $O(2)$ invariant, it is clear that the only terms that break the symmetry into C_4 are χ^4 and χ^{*4}. Since we are only analyzing the result of the symmetry breaking process, it is sufficient to only consider the χ^4 and χ^{*4} terms. We take $u_0 = u_1 = u_2 = 0$ and proceed to evaluate the form of the function after the action of the symmetry breaking impulse. By only considering the symmetry breaking terms, our evolution operator becomes

$$e^{i\Delta\hat{V}\Delta\tau} = e^{i\Delta\tau(v_0\chi^4 + v_1\chi^{*4})}. \tag{4.11}$$

4.3 Transformation Rule

Before we proceed, we can predict the singularity structure of the singularities after symmetry breaking via the transformation rule [31]. If an $O(2)$ (infinitely) symmetric waveform interacts with a discretely symmetric impulse, the resulting waveform takes on the discrete symmetry of the impulse [31]. The question is, how does the singularity get changed physically? For a symmetric wave function, $\psi(r,\theta) = e^{im\theta}u(r,\theta)$, where

$u(r,\theta) = u(r,\theta + \frac{2\pi}{N})$ is the amplitude field of the wave function, θ is the phase, m is the central singularity winding number, and N is the symmetry order. To differentiate between the daughter singularities after symmetry breaking and the incident parent singularity, we refer to the winding numbers of the post-symmetry breaking singularity as m, rather than ℓ. The value of m can take on several values based on the symmetry order:

$$m = \begin{cases} 0, \pm 1, \pm 2, \ldots, \pm\frac{N}{2}, & \text{even } N \\ 0, \pm 1, \pm 2, \ldots, \pm\frac{N-1}{2}, & \text{odd } N. \end{cases} \tag{4.12}$$

Now that we have various options for m, we can use it to find out how many daughter singularities come off axis after symmetry breaking. This is governed by the *transformation rule* [31]

$$\ell - m = kN, \tag{4.13}$$

where ℓ is the winding number of the singularity and k is an integer. The integer k is related to the number of rings of single valued singularities emerging from the axis. For the typical symmetry breaking potential, only one ring of positively single charged singularities emerges from the origin. The number of daughter singularities propagating off the axis is determined by kN. In general, the off axis singularities carry $m = 1$ and there are always N of them [31]. For an incident singularity with winding number $\ell = 3$ being broken by an $N = 4$ symmetric impulse, the transformation rule gives $3 - m = 4$, so evidently our central singularity has winding number $m = -1$. In this case, a single singularity of winding number $\ell = 3$ will result in 5 singularities after symmetry breaking. One stays at the origin, with a new winding number of $m = -1$, and four come symmetrically off-axis with winding number $m = 1$, as seen in Figure 1.1. Since the central singularity resides at the origin, and therefore does not have interesting dynamics, we will only study the behavior of the N off-axis singularities. Let us now explicitly calculate the outcome of the symmetry breaking impulse on our initial parent singularity. We begin by introducing the initial singularity state.

CHAPTER 5

PROPAGATION AFTER SYMMETRY BREAKING

We are interested in the analytical description of the symmetry breaking process of a singularity propagating in the fully rotationally invariant medium after experiencing the symmetry breaking impulse. According to the analysis of the potential profile in chapter 4, the amplitude of the singularity wave function after the action of the impulse will be given by

$$\bar{\phi}(\chi,\, \tau_1) = e^{i\Delta V(\chi)\Delta\tau}\phi(\chi,\, \tau_1), \tag{5.1}$$

where $\phi(\chi,\, \tau_1)$ represents the singularity wave function before the impulse.

5.1 Incident Singularity

To observe distinct singularities after symmetry breaking, we need to begin with a stationary state of the harmonic oscillator. The stationary state wave functions of the harmonic oscillator are given by

$$\phi_n(\tilde{x}) = \sqrt{\frac{1}{2^n n! \sqrt{\pi}}} H_n(\tilde{x}) e^{-\tilde{x}^2/2}, \tag{5.2}$$

where $H_n(\tilde{x})$ are Hermite polynomials [105]. To extend these states into two dimensions, we multiply $\phi_n(\tilde{x})$ and $\phi_m(\tilde{y})$ [108]. Continuing to substitute our dimensionless conventions introduced in Sec. 3.2.1, the 2-D stationary state becomes

$$\phi_{nm}(\tilde{\mathbf{x}}) = \frac{1}{\sqrt{2^{n+m} n! m! \pi}} H_n(\tilde{x}) H_m(\tilde{y}) e^{-(\tilde{x}^2+\tilde{y}^2)/2}. \tag{5.3}$$

This gives us the general form of our incident wave function, but we still need to make a singularity state. To describe a singularity at the origin on a Gaussian background,

which is what the harmonic oscillator state is made of, we multiply by the factor χ^l, with $\chi \equiv \tilde{x} + i\tilde{y}$. [113] Since we are going to be continuing with a direct calculation, let us take our initial parent singularity to have winding number $\ell = 3$. Thus, our wave function becomes

$$\phi_{nm}(\tilde{\mathbf{x}}) = (\tilde{x} + i\tilde{y})^3 \frac{1}{\sqrt{2^{n+m} n! m! \pi}} H_n(\tilde{x}) H_m(\tilde{y}) e^{-(\tilde{x}^2+\tilde{y}^2)/2}. \tag{5.4}$$

We would like to work with a normalized state, so let us calculate what normalization constant we will need. To begin, we enforce the normalization conditions such that $\int_{-\infty}^{\infty} d\tilde{\mathbf{x}}\, \phi^*_{nm}(\tilde{\mathbf{x}})\phi_{nm}(\tilde{\mathbf{x}}) = 1$. For the case of $l = 3$,

$$\int_{-\infty}^{\infty} d\tilde{x} \int_{-\infty}^{\infty} d\tilde{y} \left| (\tilde{x} + i\tilde{y})^3 \frac{1}{\sqrt{2^{n+m} n! m! \pi L^2}} H_n(\tilde{x}) H_m(\tilde{y}) e^{-(\tilde{x}^2+\tilde{y}^2)/2} \right|^2 = \sqrt{6}. \tag{5.5}$$

Thus, we need to add a factor of $\sqrt{1/6}$ onto our input wave function, making it now

$$\phi_{nm}(\tilde{\mathbf{x}}) = \sqrt{\frac{1}{6}} (\tilde{x} + i\tilde{y})^3 \frac{1}{\sqrt{2^{n+m} n! m! \pi}} H_n(\tilde{x}) H_m(\tilde{y}) e^{-(\tilde{x}^2+\tilde{y}^2)/2}. \tag{5.6}$$

To test whether this state is in fact a stationary state, it needs to satisfy the time-independent Schrödinger equation. Since we are using the ground state for our calculations, we set $n = m = 0$. The time-independent Schrödinger equation for the two-dimensional harmonic oscillator in dimensionless units from (3.12) is given by

$$\left[-\frac{1}{2}\tilde{\nabla}^2 + \frac{1}{2}(\tilde{x}^2 + \tilde{y}^2) \right] \phi(\tilde{x},\ \tilde{y}) = E\phi(\tilde{x},\ \tilde{y}). \tag{5.7}$$

If we substitute (5.6) into the previous equation, we see that $E = (1 + \ell)$. This result shows us that the winding number of the singularity adds an additional ℓ units relative to the ground state energy. However, our input wave function still satisfies the time-independent Schrödinger equation, so it is indeed a stationary state. We can

also find the eigenvalue of the orbital angular momentum operator L_{z} by operating on the wave function with $L_{\mathrm{z}} = xp_{\mathrm{y}} - yp_{\mathrm{x}}$. Doing so, we see that the eigenvalue is the winding number, ℓ.

5.2 Propagation

Now that we have a valid expression for the initial singularity state $\phi_{n,m}(\tilde{\mathbf{x}})$, we can insert it into our expression for the wave function after the impulse given by (5.1) using the Taylor expansion of the evolution operator given in (4.11). This gives us

$$\bar{\phi}(\tilde{\mathbf{x}}) = e^{ih\Delta\tau\left[v_0(\tilde{x}+i\tilde{y})^4+v_1(\tilde{x}-i\tilde{y})^4\right]}\phi(\tilde{\mathbf{x}}). \tag{5.8}$$

If we carry out another Taylor expansion for the exponential, we get the expression for $\bar{\phi}(\tilde{\mathbf{x}})$ that will be used for the propagation in the harmonic trap.

$$\bar{\phi}(\tilde{\mathbf{x}}) = \left[1 + iv_0 h\Delta\tau(\tilde{x}+i\tilde{y})^4 + iv_1 h\Delta\tau(\tilde{x}+i\tilde{y})^{*4}\right]\phi(\tilde{\mathbf{x}}). \tag{5.9}$$

Inserting the initial state ϕ_{nm} given in Sec. 5.1 into the previous equation, we arrive at the final form of our wave function after symmetry breaking.

$$\begin{aligned}\bar{\phi}(\tilde{\mathbf{x}}) = &\left[1 + iv_0\Delta\tau(\tilde{x}+i\tilde{y})^4 + iv_1\Delta\tau(\tilde{x}-i\tilde{y})^4\right]\sqrt{\frac{1}{6}}(\tilde{x}+i\tilde{y})^3\frac{1}{\sqrt{2^{n+m}n!m!\pi}}\times \\ &\times H_n(\tilde{x})H_m(\tilde{y})e^{-(\tilde{x}^2+\tilde{y}^2)/2},\end{aligned} \tag{5.10}$$

where χ was replaced by its Cartesian representation, $\chi \equiv \tilde{x} + i\tilde{y}$. Taking the initial state to be the ground state, given by

$$\phi_{00} = \frac{1}{\sqrt{6\pi}}e^{-(x^2+y^2)/2}(x+iy)^3, \tag{5.11}$$

equation (5.10) is then used as the initial function in the harmonic-oscillator propagator from (3.36). Before we integrate, it is convenient to absorb the length of the impulse $\Delta\tau$ into the constants v_0 and v_1, such that $v_0\Delta\tau \equiv v_0$ and $v_1\Delta\tau \equiv v_1$. Now, if we carry out the propagator integral given by (3.36) for the previous equation using the initial state ϕ_{00}, we get the final wave-function for the singularity field after symmetry breaking:

$$\begin{aligned}\phi(\tilde{x},\ \tilde{y},\ \tau) = e^{-8i\tau-(\tilde{x}^2+\tilde{y}^2)/2}\sqrt{\frac{\pi}{6}}\,\big(&e^{4i\tau}(\tilde{x}+i\tilde{y})^3 + iv_0(\tilde{x}+i\tilde{y})^7 \\ &+ v_1(i\tilde{x}+\tilde{y})\left\{24e^{6i\tau} + 36e^{4i\tau}(\tilde{x}^2+\tilde{y}^2-2) + (\tilde{x}^2+\tilde{y}^2-12)(\tilde{x}^2+\tilde{y}^2)^2\right. \\ &\left.+12(3\tilde{x}^2+3\tilde{y}^2-2) + 12e^{2i\tau}\left[6+\tilde{x}^4-6\tilde{y}^2+\tilde{y}^4+2\tilde{x}^2(\tilde{y}^2-3)\right]\right\}\big)\,. \quad (5.12)\end{aligned}$$

As a preliminary observation, we can plot the amplitude of $\phi(\tilde{x},\ \tilde{y},\ \tau)$ via Contour Plot 3D in Mathematica, so we can have an idea of what the singularities should be doing after symmetry breaking before we explicitly calculate the trajectories. If we choose $v_1 = v_0 = 5 \times 10^{-4}$, we get the following figure:

As we expected from the transformation rule analysis in Sec. 4.3, we have four singularities propagating off axis. If we take several time slices of our system, we can track the rotation direction of the off-axis singularities about the axis of symmetry, as well as have a better understanding of the symmetry breaking process. We can view the progression of the singularities in Figure 5.2. The axis of symmetry in this case is the origin.

The singularities are evidently propagating in a counterclockwise direction around the origin.

5.2.1 Angular Momentum Structure

The expression for $\phi(\tilde{\mathbf{x}})$ in (5.12) can be written in a clearer form by reintroducing the complex coordinate $\chi = \tilde{x} + i\tilde{y}$ so that we can recognize a well defined angular

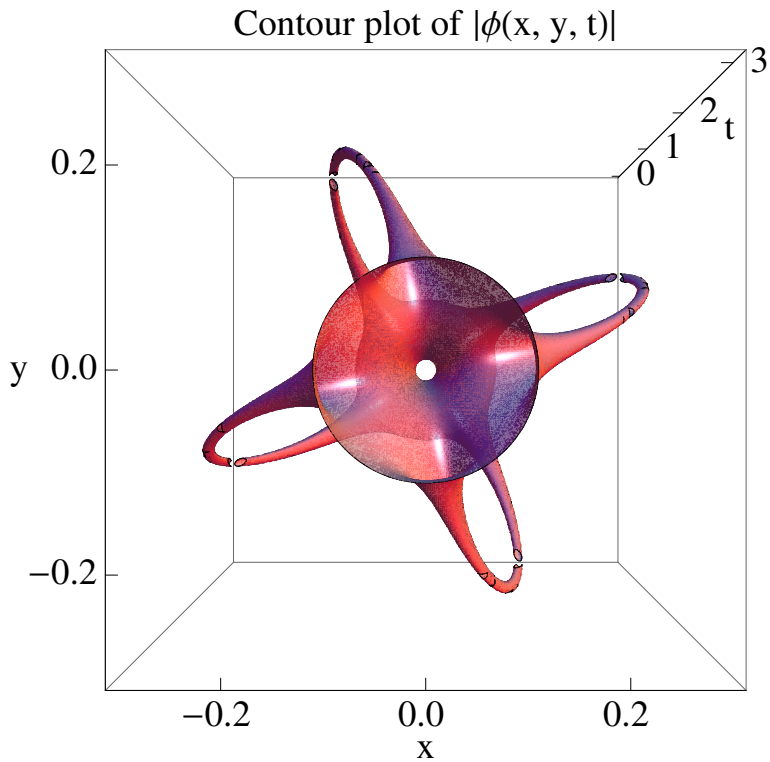

Figure 5.1: 3-D contour plot of the amplitude of $\phi(\tilde{x},\, \tilde{y},\, \tau)$, as viewed over one period of axial oscillations. The parent singularity is broken into five daughter singularities. One singularity remains at the origin, as seen by the hole in the center of the figure. Four off-axis singularities propagate periodically about the axis of symmetry. False color is added to improve visibility.

momentum structure. After transferring to the complex coordinate χ, we get the complex version of (5.12):

$$\begin{aligned}\phi_{\text{complex}}(\chi,\ \tau) =& e^{-8i\tau-|\chi|^2/2}\sqrt{\frac{\pi}{6}}\left(e^{4i\tau}\chi^3 + iv_0\chi^7 + iv_1\chi^*\left\{-24 + 24e^{6i\tau} + \right.\right. \\ &\left.\left. +|\chi|^2(|\chi|^2-6)^2 + 36e^{4i\tau}(|\chi|^2-2) + 12e^{2i\tau}\left[6+|\chi|^2(|\chi|^2-6)\right]\right\}\right)\end{aligned} \tag{5.13}$$

We can break this down so that

$$\phi_{\text{complex}}(\chi,\ \tau) = e^{-8i\tau-|\chi|^2/2}\sqrt{\frac{\pi}{6}}\left(A_0(\tau)\chi^3 + A_+\chi^7 + A_-(|\chi|,\ \tau)\chi^*\right), \tag{5.14}$$

where

$$A_+ \equiv iv_0, \tag{5.15}$$

$$A_0(\tau) \equiv e^{4i\tau}, \tag{5.16}$$

and

$$\begin{aligned} A_-(|\chi|,\ \tau) \equiv & iv_1 \left\{ -24 + 24e^{6i\tau} + |\chi|^2(|\chi|^2 - 6)^2 + 36e^{4i\tau}(|\chi|^2 - 2) \right. \\ & \left. +12e^{2i\tau} \left[6 + |\chi|^2(|\chi|^2 - 6) \right] \right\} \end{aligned} \tag{5.17}$$

The expression in (5.14) has the form predicted by our previous symmetry arguments from Sec. 4.3 and [60] since it can be written as

$$\phi(\chi,\ \tau) = \sqrt{\frac{\pi}{6}} e^{-8it-|\chi|^2/2} \chi^* \left(\frac{A_+\chi^8 + A_0(t)\chi^4}{|\chi|^2} + A_-(|\chi|,\ t) \right) = \chi^* F(\chi,\ t), \tag{5.18}$$

where we have used the identities $\frac{\chi^7}{\chi^*} = \frac{\chi^8}{|\chi|^2}$ and $\frac{\chi^3}{\chi^*} = \frac{\chi^4}{|\chi|^2}$, and where

$$F(\chi,\ \tau) \equiv \sqrt{\frac{\pi}{6}} e^{-8it-|\chi|^2/2} \left(\frac{A_+\chi^8 + A_0(t)\chi^4}{|\chi|^2} + A_-(|\chi|,\ t) \right). \tag{5.19}$$

It becomes immediately apparent that $F(\chi,\ \tau)$ is C_4 invariant due to the dependence on only χ^4 and χ^8 terms. Because $F(\chi,\ \tau)$ is C_4 invariant,

$$\phi(\epsilon\chi,\ \tau) = \epsilon^{-1}\phi(\chi,\ \tau), \tag{5.20}$$

where $\epsilon \equiv e^{i\pi/2}$ is the elementary rotation of 4th order. Thus, as expected from the analysis in Sec. 4.3 using the transformation rule, the solution preserves the winding number $m = -1$ for the center singularity.

5.3 Trajectories

In this thesis, we are interested in the trajectories followed by the singularities that arise after symmetry breaking. Since we have an analytical expression for the propagating field, we can obtain clearer insight into the dynamics of these singularities. Singularities are given by the zeros of the complex wave function $\phi(\chi,\ \tau)$. We can find these zeros by setting $\phi(\chi,\ \tau) = 0$ and solving for χ. From (5.18), we see that there are two situations when $\phi(\chi,\ \tau) = 0$, when $\chi^* = 0$ and when $F(\chi,\ \tau) = 0$. The former corresponds to the singularity at the origin of winding number $m = -1$ that we have predicted in Sec. 4.3. We can study the behavior of the wave function near the origin ($|\chi| \approx 0$) by developing $\phi(\chi,\ \tau)$ in a Taylor series around $\chi = 0$:

$$\phi(\chi,\ \tau) \approx 32e^{-5i\tau}\sqrt{6\pi}\sin^3(\tau)v_1\chi^*. \tag{5.21}$$

Evidently, the singularity at the origin is due to the symmetry breaking of the initial parent singularity, as seen by the dependence on the symmetry breaking parameter v_1. We see again that this singularity has winding number $m = -1$, as evidenced by the factor of χ^*. If we set $v_1 = 0$, then $A_-(|\chi|,\ \tau) = 0$, and the expansion about $\chi = 0$ is instead

$$\phi(\chi,\ \tau) \approx \sqrt{\frac{\pi}{6}}e^{-4i\tau}\chi^3, \tag{5.22}$$

which preserves the initial winding number of $\ell = 3$, as seen by χ^3. The latter type of phase singularity, when $F(\chi,\ \tau) = 0$, is more difficult to analyze because we have to work with the complex roots of the nonlinear equation $F(\chi,\ \tau) = 0$. This is the same as solving the equation

$$A_+\chi^8 + A_0(\tau)\chi^4 + |\chi|^2 A_-(|\chi|,\ \tau) = 0. \tag{5.23}$$

To make the calculation easier, we assume that the two symmetry breaking parameters are of the same order. Thus, we take $v_0 \approx v_1 = v$. If we go to the $v = 0$ limit, we see that $A_+ = 0$ and $A_-(|\chi|,\ \tau) = 0$. For $F(\chi,\ \tau) = 0$ to be true in this limit, it follows that as $v \approx 0$, $A_0(\tau)|\chi|^4 \approx 0$, and therefore $\chi \approx 0$, leading to the conclusion that $\chi = \chi(v)$, and the statement that in the $v \ll 1$ regime, $|\chi| \ll 1$. For small values of χ, the first terms that reappear in (5.23) are those in $A_-(|\chi|,\ \tau)$ that depend on $|\chi|^2$. Due to $|\chi|$ being much less than 1, it follows that $|\chi|^2 > |\chi|^4 > |\chi|^8$. By expanding out $A_-(|\chi|,\ \tau)$, we see that the $|\chi^2|$ term is

$$\lim_{v \ll 1} A_-(|\chi|,\ t) \approx |\chi|^2(-24iv_1 + 72ie^{2it}v_1 - 72ie^{4it}v_1 + 24ie^{6it}v_1). \tag{5.24}$$

By using this approximation, we can instead solve the equation

$$F \approx A_0(\tau)\chi^4 + \lim_{v \ll 1} A_-(|\chi|,\ t) = 0, \tag{5.25}$$

where we have kept only the nonzero terms from the $v \ll 1$ limit. Thus, to this order

$$e^{4it}\chi^4 + |\chi|^2(-24iv_1 + 72ie^{2it}v_1 - 72ie^{4it}v_1 + 24ie^{6it}v_1) = 0. \tag{5.26}$$

If we solve for χ^4,

$$\chi^4 = \frac{24iv_1 - 72ie^{2it}v_1 + 72ie^{4it}v_1 - 24ie^{6it}v_1}{e^{4it}}|\chi|^2 = vp(t)|\chi|^2. \tag{5.27}$$

The simplest mathematical object to calculate now is $|\chi|$. This is done by taking the modulus of the previous expression and dividing by $|\chi|^2$. We obtain

$$|\chi|^2 = 192v_1 \sin^3 \tau. \tag{5.28}$$

The equation above provides the evolution of the radial coordinate of the off-axis singularities. Recall that $|\chi(\tau)|^2 = \tilde{x}(\tau)^2 + \tilde{y}(\tau)^2 = r(\tau)^2$ so that in polar coordinates the radius of the phase singularity trajectory is given by

$$R(\tau) \approx 8\sqrt{3}(v_1 \sin^3(\tau))^{1/2}. \tag{5.29}$$

To find $\theta(\tau)$, we need to look back at (5.27). If we rewrite χ and p in modulus-argument complex form, χ becomes $|\chi|e^{i\theta}$ and p becomes $|p|e^{i\gamma}$. Equation (5.27) becomes

$$|\chi|^4 e^{i4\theta} = v|p|e^{i\gamma}|\chi|^2 \quad |\chi|^2 e^{i4\theta} = v|p|e^{i\gamma}. \tag{5.30}$$

We saw in (5.27) that $|\chi|^2 = vp$, so the previous equation becomes

$$e^{i4\theta} = e^{i\gamma} = 4\theta = \gamma + 2n\pi. \tag{5.31}$$

Thus, the evolution of the polar coordinates of the singularities is provided by the phase of $p(\tau)$. From (5.27),

$$p(\tau) = \frac{24i - 72ie^{2i\tau} + 72ie^{4i\tau} - 24ie^{6i\tau}}{e^{4i\tau}}. \tag{5.32}$$

The phase of $p(\tau)$ is found by taking the arctangent of $p(\tau)$. This gives us

$$\theta(\tau) = \frac{1}{4}\gamma = \frac{1}{4}\left[2n\pi + \arctan\left(\frac{\sin^4(\tau)}{-\cos(\tau)\sin^3(\tau)}\right)\right] = \frac{n\pi}{2} - \frac{\tau}{4} \tag{5.33}$$

We can plot the previous trajectories in the Cartesian plane by using the relations $\tilde{x} = R\cos(\theta)$ and $\tilde{y} = R\sin(\theta)$. The trajectories are plotted in Figure 5.3.

If we compare these trajectories with the amplitude of the final wave function, we see that they match. Figure 5.4 includes both the analytical trajectories and the amplitude of the wave function in Figure 5.1 for comparison. An in-depth convergence

study can be found in chapter 7.

5.4 Recombination Time and Maximum Radius

By analyzing the radial component of the trajectories when $R(\tau)$ returns to zero, we can determine the amount of time it takes for the singularities to recombine at the origin. We can equate $R(\tau)$ in (5.29) to 0 and solve for τ. Doing so, we see that

$$R(t) = 0 \quad \forall \quad \tau = n\pi \tag{5.34}$$

where n is an integer. Replacing the dimensionless variables with their original counterparts, we see that the recombination time is

$$t_{\text{recombination}} = \frac{n\pi}{\omega}, \tag{5.35}$$

or half the period of the trapping potential. We can also analytically solve for the maximum radius the trajectories achieve. We first take the derivative of the radial function in (5.29) and set it equal to zero to determine when the trajectories reach their maximum radius. Doing so, we see that R_{max} occurs at $\tau = \pi/2$. Evaluating (5.29) at $\tau = \pi/2$, we get a maximum radius of

$$R_{\text{max}} = 8\sqrt{3v}. \tag{5.36}$$

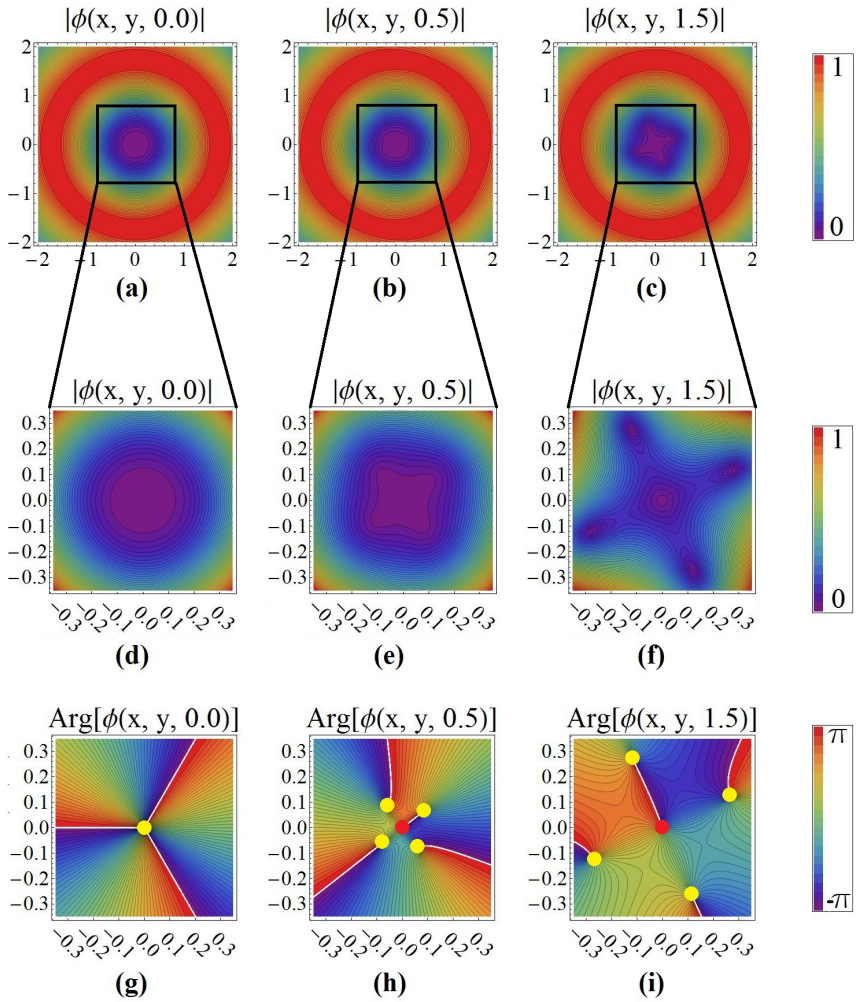

Figure 5.2: By plotting the amplitude of the wave function after symmetry breaking at discrete time steps, we can track the rotation of the off-axis singularities about the axis of symmetry. It is apparent that the singularities rotate clockwise around the axis of symmetry. We also plot the phase of the wave function and mark the singularities that arise after symmetry breaking. Positively charged singularities are yellow, and negatively charged ones are red.

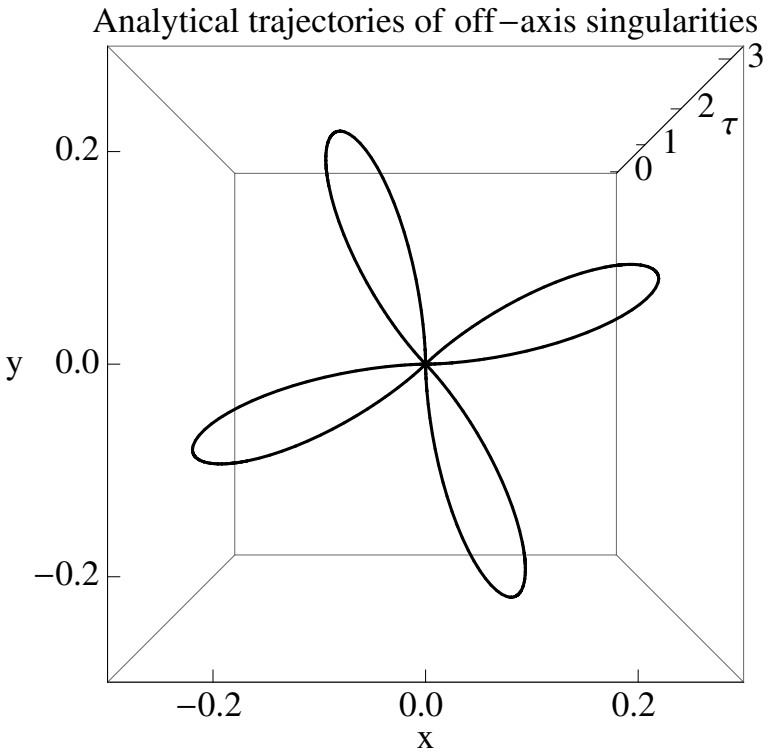

Figure 5.3: The trajectories of the four singularities that arise after symmetry breaking. The singularities traverse these lines in the clockwise direction. The trajectories are plotted over one period of the trapping potential.

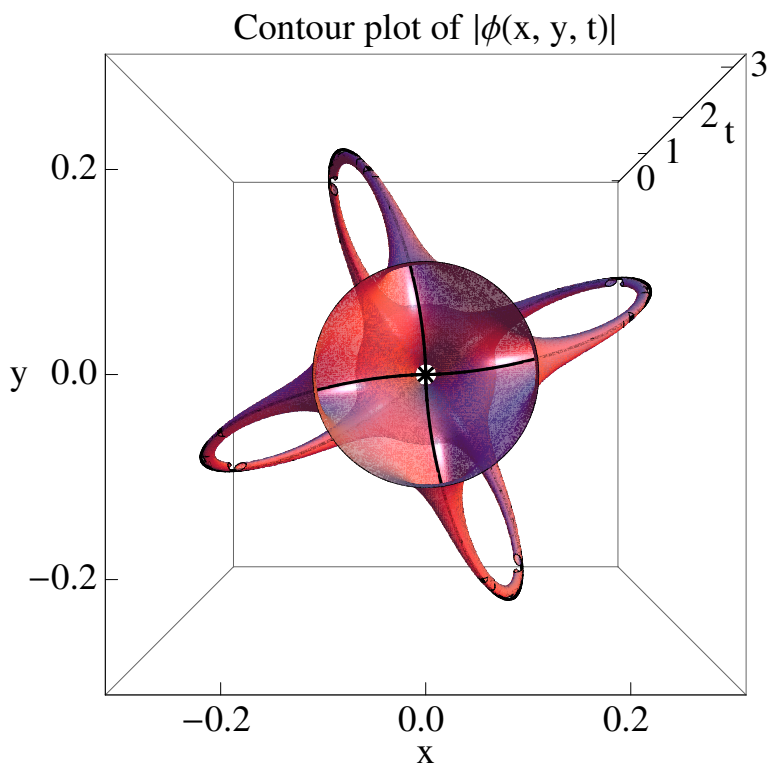

Figure 5.4: The analytical trajectories seen in Figure 5.3 are compared to the contour plot of the amplitude of the final wave function seen in Figure 5.1. A full convergence study between the approximate trajectories and the minimum of the wave function can be found in chapter 7.

CHAPTER 6

EQUATIONS OF MOTION

Using the expressions obtained for $R(\tau)$ and $\theta(\tau)$, we can find the equations of motion for the off-axis singularities. The equations of motion will reveal the effects of the impulse on the incident parent singularity in more detail.

6.1 Effective Forces

By taking the derivatives of $R(\tau)$, we see that the velocity and acceleration in the radial component can be expressed as

$$\dot{R}(\tau) = 12\sqrt{3}\cos(t)(v_1 \sin(\tau))^{1/2}, \tag{6.1}$$

$$\ddot{R}(\tau) = 3\sqrt{3}(3\cos(2t) - 1)(v_1 \csc(\tau))^{1/2}. \tag{6.2}$$

By taking the derivatives of $\theta(\tau)$, we see that the angular velocity is constant, and therefore the angular acceleration is zero. Thus,

$$\dot{\theta}(\tau) = -\frac{1}{4}, \tag{6.3}$$

$$\ddot{\theta}(\tau) = 0. \tag{6.4}$$

However, the fact that there is an angular velocity at all tells us that the singularities have experienced a torque about the axis at some point in their creation and propagation. If we recombine $R(\tau)$ and $\theta(\tau)$ into the complex coordinate $\chi(\tau) = R(\tau)e^{i\theta(\tau)}$ once again, we can study the behavior of the singularities immediately after symmetry breaking. If we Taylor expand equations (5.29) and (5.33) around $\tau = 0$, i.e., immediately after symmetry breaking, we get

$$R(\tau) \approx 8\sqrt{3}\sqrt{v}\,\tau^{3/2}, \tag{6.5}$$

and

$$\theta(\tau) \approx \frac{\pi}{4} - \frac{\tau}{4}. \tag{6.6}$$

The previous expansions give us the complex coordinate $\chi(\tau)$ right after symmetry breaking, such that

$$\chi(\tau) \approx 8\sqrt{3v}\,\tau^{3/2} e^{\frac{i}{4}(\pi-\tau)}. \tag{6.7}$$

We now proceed to derive the equation of motion associated to (6.7). If we differentiate (6.7) with respect to τ, we see that

$$\chi'(\tau) = \left(\frac{3}{2\tau} - \frac{i}{4}\right)\chi(\tau). \tag{6.8}$$

A second derivative of (6.7) will provide us with the equation of motion in complex notation:

$$\chi''(\tau) = \frac{12 - \tau(12i + \tau)}{16\tau^2}\chi(\tau). \tag{6.9}$$

If we let $\Omega_0^2 = \frac{1}{16} - \frac{3}{4\tau^2}$, and $\Omega_1^2 = \frac{3}{4\tau}$, we can rewrite (6.9) as

$$\chi''(\tau) = -(\Omega_0^2 + i\Omega_1^2)\chi(\tau). \tag{6.10}$$

Evidently, the singularities experience a nontrivial type of force. The previous equation represents a special type of harmonic oscillator in which the frequency is both complex and time dependent. Since the frequency is complex, we do not expect the system to be conservative. We can prove this statement by manipulating (6.9) and its conjugate in the same manner we would do to establish conservation of energy in a standard harmonic oscillator. First, we write the conjugate of (6.9):

$$\chi''^*(\tau) = -(\Omega_0^2 - i\Omega_1^2)\chi^*(\tau). \tag{6.11}$$

Next, we multiply (6.9) by $\chi'^*(\tau)$ and (6.11) by $\chi'(\tau)$ and add the two resulting equations to obtain

$$\begin{aligned}\chi''(\tau)\chi'^*(\tau)+\chi'(\tau)\chi''^*(\tau) &= -(\Omega_0^2+i\Omega_1^2)\chi(\tau)\chi'^*(\tau)+\chi'(\tau)(-\Omega_0^2+i\Omega_1^2)\chi^*(\tau) \quad (6.12)\\ &= -\Omega_0^2\chi(\tau)\chi'^*(\tau)-i\Omega_1^2\chi(\tau)\chi'^*(\tau)-\Omega_0^2\chi'(\tau)\chi^*(\tau)+i\Omega_1^2\chi'(\tau)\chi^*(\tau)\\ &= -\Omega_0^2(\chi(\tau)\chi'^*(\tau)+\chi'(\tau)\chi^*(\tau))+i\Omega_1^2(\chi'(\tau)\chi^*(\tau)-\chi(\tau)\chi'^*(\tau)).\end{aligned}$$

We immediately recognize that the left hand side and the first term of the right hand side are total derivatives. If we rewrite the total derivatives, we get

$$\frac{d}{d\tau}(\chi'(\tau)\chi'^*(\tau)) = -\Omega_0^2\,\frac{d}{d\tau}(\chi(\tau)\chi^*(\tau))+i\Omega_1^2(\chi'(\tau)\chi^*(\tau)-\chi(\tau)\chi'^*(\tau)). \quad (6.13)$$

Unfortunately, Ω_0^2 is time dependent, so we cannot just combine the total derivatives. Instead, we must subtract the term with $\frac{d}{d\tau}\Omega_0^2$. Namely, the total derivative of the Ω_0^2 term is

$$\frac{d}{d\tau}(\Omega_0^2\chi(\tau)\chi^*(\tau)) = \chi(\tau)\chi^*(\tau)\frac{d}{d\tau}\Omega_0^2+\Omega_0^2\frac{d}{d\tau}\chi(\tau)\chi^*(\tau). \quad (6.14)$$

This allows us to rewrite (6.13) as

$$\begin{aligned}\frac{d}{d\tau}(\chi'(\tau)\chi'^*(\tau))+\Omega_0^2\frac{d}{d\tau}(\chi(\tau)\chi^*(\tau)) &= i\Omega_1^2(\chi'(\tau)\chi^*(\tau)-\chi(\tau)\chi'^*(\tau))\\ \frac{d}{d\tau}\left(\chi'(\tau)\chi'^*(\tau)+\Omega_0^2\chi(\tau)\chi^*(\tau)\right)-\chi(\tau)\chi^*(\tau)\frac{d}{d\tau}\Omega_0^2 &= i\Omega_1^2(\chi'(\tau)\chi^*(\tau)-\chi(\tau)\chi'^*(\tau)).\end{aligned} \quad (6.15)$$

If we replace $\chi'(\tau)$ and $\chi'^*(\tau)$ with their functional values, and evaluate the derivative of Ω_0^2, we obtain

$$\frac{d}{d\tau}\left(\chi'(\tau)\chi'^*(\tau)+\Omega_0^2\chi(\tau)\chi^*(\tau)\right) = \left(\frac{3}{2\tau^3}+\frac{\Omega_1^2}{2}\right)\chi(\tau)\chi^*(\tau). \quad (6.16)$$

If we define the energy of the system the same way we would a typical harmonic oscillator,

$$E = \frac{1}{2}\chi'(\tau)\chi'^*(\tau) + \frac{1}{2}\Omega_0^2\chi(\tau)\chi^*(\tau), \tag{6.17}$$

it is clear that there is gain in the system. We can see the value of the gain by considering the derivative of the energy:

$$\begin{aligned}
\frac{dE}{d\tau} &= \frac{1}{2}\frac{d}{d\tau}\left(\chi'(\tau)\chi'^*(\tau) + \Omega_0^2\chi(\tau)\chi^*(\tau)\right) && (6.18)\\
&= \frac{1}{2}\left(\frac{3}{2\tau^3} + \frac{\Omega_1^2}{2}\right)\chi(\tau)\chi^*(\tau) && (6.19)\\
&= \frac{3}{4\tau}\left(\frac{1}{\tau^2} + \frac{1}{4}\right)|\chi(\tau)|^2 \geq 0. && (6.20)
\end{aligned}$$

Thus, energy is not conserved by the system containing just the singularities described by our equations of motion. However, the nonlinear Schrödinger equation does conserve energy, so the energy is being exchanged between the singularities and the remainder of the Bose-Einstein condensate described by the full nonlinear Schrödinger equation. The presence of this effective harmonic motion explains why the post-symmetry breaking singularities expel from the origin. However, we still need to explain the effective torque that the singularities seem to experience. To understand this torque better, let us rewrite our complex coordinate in Cartesian coordinates via the definition of $\chi(\tau) = \tilde{x}(\tau) + i\tilde{y}(\tau)$. This gives us

$$\begin{aligned}
\chi''(\tau) &= \tilde{x}''(\tau) + i\tilde{y}''(\tau) && (6.21)\\
&= -(\Omega_0^2 + i\Omega_1^2)(\tilde{x}(\tau) + i\tilde{y}(\tau))\\
&= -(\Omega_0^2 + i\Omega_1^2)\tilde{x}(\tau) - i(\Omega_0^2 + i\Omega_1^2)\tilde{y}(\tau)\\
&= -\Omega_0^2\tilde{x}(\tau) - i\Omega_1^2\tilde{x}(\tau) - i\Omega_0^2\tilde{y}(\tau) + \Omega_1^2\tilde{y}(\tau).
\end{aligned}$$

If we collect the real and imaginary parts, we arrive at

$$\tilde{x}''(\tau) = -\Omega_0^2 \tilde{x}(\tau) + \Omega_1^2 \tilde{y}(\tau) \tag{6.22}$$

$$\tilde{y}''(\tau) = -\Omega_0^2 \tilde{y}(\tau) - \Omega_1^2 \tilde{x}(\tau). \tag{6.23}$$

We can write the previous equations in vector form as

$$\mathbf{r}\,''(\tau) = -\Omega_0^2 \mathbf{r}(\tau) + \Omega_1^2 \begin{bmatrix} 0 & 1 \\ -1 & 0 \end{bmatrix} \mathbf{r}(\tau). \tag{6.24}$$

In order to see how a torque comes into our system, we need to rewrite the Ω_1^2 matrix term in three-dimensions. To do this, we construct the external 3-D vector $\Lambda = (0,\ 0,\ \Omega_1^2)$ such that

$$\mathbf{r} \times \Lambda = \begin{vmatrix} \mathbf{i} & \mathbf{j} & \mathbf{k} \\ \tilde{x} & \tilde{y} & \tilde{z} \\ 0 & 0 & \Omega_1^2 \end{vmatrix} = \Omega_1^2 (\tilde{y},\ -\tilde{x},\ 0) = \Omega_1^2 \begin{bmatrix} 0 & 1 \\ -1 & 0 \end{bmatrix} \mathbf{r}_T(\tau), \tag{6.25}$$

where $\mathbf{r}_T(\tau)$ is the transverse plane, which we are working in. Therefore, the equation of motion for the singularities can be represented in 3-D, although the motion is restricted to a two-dimensional plane $\mathbf{r}(\tau) = (\tilde{x}, \tilde{y}, 0)$. We write our 3-D representation as

$$\mathbf{r}\,''(\tau) = -\Omega_0^2 \mathbf{r}(\tau) + (\mathbf{r}(\tau) \times \Lambda). \tag{6.26}$$

This equation of motion shows the simultaneous presence of a harmonic force and an external force associated with a torque. The fact that the latter is associated with a torque can be checked by calculating its effect on the angular momentum of the phase singularity, $\mathbf{L} = \mathbf{r} \times \mathbf{r}'$. If we look at the derivative of the angular momentum,

we see that

$$\frac{d\mathbf{L}}{d\tau} = \frac{d}{d\tau}(\mathbf{r} \times \mathbf{r}') = \mathbf{r}' \times \mathbf{r}' + \mathbf{r} \times \mathbf{r}'' = \mathbf{r} \times \mathbf{r}''. \tag{6.27}$$

If we evaluate this cross product using our expression for $\mathbf{r}''(\tau)$ in (6.26),

$$\begin{aligned} \mathbf{r} \times \mathbf{r}'' &= \mathbf{r} \times (-\Omega_0^2 \mathbf{r} + (\mathbf{r} \times \Lambda) \\ &= -\Omega_0^2 (\mathbf{r} \times \mathbf{r}) + \mathbf{r} \times (\mathbf{r} \times \Lambda) \\ &= \mathbf{r} \times (\mathbf{r} \times \Lambda). \end{aligned} \tag{6.28}$$

Using the vector triple product [114], we obtain

$$\mathbf{r} \times \mathbf{r}'' = \mathbf{r}(\mathbf{r} \cdot \Lambda) - \Lambda(\mathbf{r} \cdot \mathbf{r}). \tag{6.29}$$

Because Λ is defined only to have a $\tilde{z}$ component, and our position vector is two-dimensional, the dot product of $\mathbf{r}$ with Λ vanishes, leaving

$$\begin{aligned} \mathbf{r} \times \mathbf{r}'' &= -\Lambda(\mathbf{r} \cdot \mathbf{r}) \\ &= -\Lambda |\mathbf{r}|^2 \\ &= (0,\ 0\ , -\Omega_1^2 |\mathbf{r}_T|^2). \end{aligned} \tag{6.30}$$

Finally, we arrive at

$$\frac{d\mathbf{L}}{d\tau} = \mathbf{M} \equiv \left(0,\ 0,\ -\Omega_1^2 |\mathbf{r}_T|^2\right) = \left(0,\ 0,\ -|\mathbf{r}_T|^2 \frac{3}{4\tau}\right), \tag{6.31}$$

where $\mathbf{M}$ is the torque. The previous equation shows that the angular momentum has variation only in the $\tilde{z}$ direction, which means there is a torque that causes rotation in the $\tilde{x},\ \tilde{y}$ plane, as we expect. Because the value of the torque is negative, our singularities rotate about the origin in a clockwise manner, as our trajectories in Sec. 5.3 were seen to do in Figure 5.2. We can check that the energy equation we found

in (6.18) is correct using our 3-D formalism. If we take the inner product of $\mathbf{r}'$ with $\mathbf{r}''$, we see that

$$\begin{aligned}
\mathbf{r}' \cdot \mathbf{r}'' &= \mathbf{r} \cdot (-\Omega_0^2 \mathbf{r} + (\mathbf{r} \times \Lambda)) \\
&= -\Omega_0^2 (\mathbf{r}' \cdot \mathbf{r}) + \mathbf{r}' \cdot (\mathbf{r} \times \Lambda) \\
&= -\Omega_0^2 (\mathbf{r}' \cdot \mathbf{r}) + \Lambda \cdot (\mathbf{r}' \times \mathbf{r}) \\
&= -\Omega_0^2 (\mathbf{r}' \cdot \mathbf{r}) - \Lambda \cdot \mathbf{L}..
\end{aligned} \tag{6.32}$$

We can rearrange for $\Lambda \cdot \mathbf{L}$ to get

$$-\Lambda \cdot \mathbf{L} = \mathbf{r}' \cdot \mathbf{r}'' + \Omega_0^2 (\mathbf{r}' \cdot \mathbf{r}). \tag{6.33}$$

If we look at the definition of energy again,

$$E = \frac{1}{2}(\mathbf{r}' \cdot \mathbf{r}') + \frac{1}{2}\Omega_0^2 (\mathbf{r} \cdot \mathbf{r}), \tag{6.34}$$

we can take the derivative to see how the energy is changing with time,

$$\begin{aligned}
\frac{dE}{d\tau} &= \frac{1}{2}\frac{d}{d\tau}(\mathbf{r}' \cdot \mathbf{r}') + \frac{1}{2}\frac{d}{d\tau}(\Omega_0^2 \mathbf{r} \cdot \mathbf{r}) \\
&= \frac{1}{2}(\mathbf{r}'' \cdot \mathbf{r}' + \mathbf{r}' \cdot \mathbf{r}'') + \frac{1}{2}\frac{d}{d\tau}(\Omega_0^2 \mathbf{r} \cdot \mathbf{r}) \\
&= \mathbf{r}' \cdot \mathbf{r}'' + \frac{1}{2}\left[\frac{d\Omega_0^2}{d\tau}(\mathbf{r} \cdot \mathbf{r}) + \Omega_0^2 (\mathbf{r}' \cdot \mathbf{r} + \mathbf{r} \cdot \mathbf{r}')\right] \\
&= \mathbf{r}' \cdot \mathbf{r}'' + \Omega_0^2 (\mathbf{r} \cdot \mathbf{r}') + \frac{1}{2}\frac{d\Omega_0^2}{d\tau}.
\end{aligned} \tag{6.35}$$

If we substitute in equation (6.33) and the value of Ω_0^2, we see that

$$\frac{dE}{d\tau} = -\Lambda \cdot \mathbf{L} + \frac{1}{2}\frac{d\Omega_0^2}{d\tau} = -\Lambda \cdot \mathbf{L} + \frac{3}{4\tau^3}, \tag{6.36}$$

and finally, if we use our numerical value for $\Lambda \cdot \mathbf{L}$, we see that the change in energy is consistent with our previous analysis in (6.18):

$$\frac{dE}{d\tau} = \frac{1}{2}\left(|\mathbf{r}|^2\Omega_1^2 + \frac{3}{4\tau^3}\right) = \frac{3}{4\tau}\left(\frac{1}{\tau^2} + \frac{1}{4}\right). \tag{6.37}$$

Let us note that all of these results apply, when properly rotated, to any of the four daughter singularities moving away from the center of symmetry. This is due to the four-fold symmetry of our solutions and it is reflected in the four solutions that we have for the angular coordinate $\theta(\tau)$ in (5.33).

6.2 Dynamics of Singularities after Rotational Symmetry Breaking

In Sec. 6.1, we derived the equation of motion for the four daughter singularities that arise immediately after symmetry breaking by a discretely symmetric impulse. We found that the breaking of rotational symmetry causes a parent singularity to cluster into a central singularity carrying topological charge equal to the angular pseudo-momentum m and a "wave" of N (N being the order of symmetry of the impulse) single charged daughter singularities with particle-like motion moving away from the symmetry axis. The dynamics of these singularities as point-like particles is described by the equation of motion in (6.26) (for the case $N = 4$). This equation is notable because it shows that although the wave function is described by the propagator for the linear harmonic oscillator, the clustered singularities do not move as classical particles in a harmonic potential. In fact, right after the action of the impulse, they experience two types of forces, as described by the right-hand side of (6.26):

- A harmonic repulsive force given by $\Omega_0^2\mathbf{r}(\tau)$.
- A rotational force $\mathbf{F} = (\mathbf{r}(\tau) \times \Lambda)$ generating a torque $\mathbf{M} = -|\mathbf{r}|^2\Lambda$.

Both forces have a peculiar behavior. Let us analyze them separately.

6.2.1 Effective Harmonic Potential

This effective potential is crucial because it is responsible for the dissociation of the initial parent singularity with topological charge $l = 3$ into the central singularity of charge $m = -1$ and four singularities of charge $q = 1$. If the interaction was attractive, the four singularities would remain at the origin (the center of symmetry) since both the initial position and initial velocity are zero. However, we find that the interaction is repulsive because $\Omega_0^2 = \frac{1}{16} - \frac{3}{4\tau^2} < 0$ for small values of τ. Nevertheless, a repulsive harmonic interaction is not enough to guarantee the motion of the broken singularities away from the origin since their position and velocity are initially zero. They would remain there in a situation of unstable equilibrium since the force upon them would be zero. Something else is needed to trigger the expansive motion of the broken singularities. The mechanism is the existence of a nonzero, in this case singular, repulsive potential at $\tau = 0$.

$$|\mathbf{F}_H| = \left|\left(\frac{1}{16} - \frac{3}{4\tau^2}\right)\right| r(\tau) \sim \frac{1}{\tau^2}\tau^{3/2} = \lim_{\tau\to 0}\frac{1}{\sqrt{\tau}} = \infty. \tag{6.38}$$

If we analyze the form of the effective harmonic potential for small values of τ, we see from (6.18) that

$$V_H(\mathbf{r}) = \frac{1}{2}\Omega_0^2|\mathbf{r}|^2 \approx -\frac{3}{4\tau^2}|\mathbf{r}|^2 \;\; \tau \ll 1, \tag{6.39}$$

indicating the presence of a singular repulsive potential at $\tau = 0$. The curvature of the quadratic potential is, thus, infinite and negative right after the symmetry is broken, so the force on the escaping singularities is non-zero when they are located at the origin when $\tau = 0$. This singular potential is the reason why the singularities start to move away from the center of symmetry. The fact that the potential and force are singular at $\tau = 0$ does not produce any issues in the velocity and position

of the fleeing singularities when $\tau = 0$ because the acceleration, which has the form $r''(\tau) \sim 1/\sqrt{\tau}$ has first and second integrals of the form:

$$r'(\tau) \sim \sqrt{\tau} + C \text{ and } r(\tau) \sim \tau^{3/2} + C', \tag{6.40}$$

which are both finite at $\tau = 0$ and compatible with the initial condition $r'(0) = 0$ and $r(0) = 0$ when the constants are taken to be zero.

6.2.2 Torque

As seen in (6.31), there is an r dependence in the torque that the singularities experience around the origin once symmetry is broken. The torque is zero when $\tau = 0$ since $\mathbf{M} \sim r^2$ and $\lim_{\tau \to 0} r^2 = 0$ due to the initial condition of $r(0) = 0$. Thus, the singularities must start moving away from each other, making $r \neq 0$, before the external torque can take effect. This allows us to conclude that the singular repulsive effective harmonic potential must act on the singularities before they can acquire any angular momentum. As our singularities acquire a linear velocity away from the origin, they become subject to the Magnus effect. This effect creates a force perpendicular to the direction of motion according to $\mathbf{F} = S(\omega \times \mathbf{v})$, where S is a property of the medium the singularity is traveling through, ω is the angular rotational velocity of the spinning object, and $\mathbf{v}$ is the linear velocity. This perpendicular Magnus force causes the singularities to follow a curved path. If we evaluate the expression for the Magnus force, we see that

$$\begin{aligned}
\mathbf{F} &= S(\omega \times \mathbf{v}) \\
&= S\langle 0,\ 0,\ \omega\rangle \times \langle \frac{3}{4\tau}\tilde{x},\ \frac{3}{4\tau}\tilde{y},\ 0\rangle \\
&= S\langle -\frac{3\omega}{4\tau}\tilde{y}, \frac{3\omega}{4\tau}\tilde{x}, 0\rangle,
\end{aligned} \tag{6.41}$$

where the velocity vector was formed by taking the derivative of the position at small τ given in (6.5). If we evaluate the torque associated with the Magnus force, we see that

$$\begin{aligned}\tau &= \mathbf{r} \times \mathbf{F} \\ &= \langle \tilde{x},\ \tilde{y},\ 0\rangle \times S\langle -\frac{3\omega}{4\tau}\tilde{y}, \frac{3\omega}{4\tau}\tilde{x}, 0\rangle \\ &= \langle 0,\ 0,\ \frac{3S\omega}{4\tau}|\mathbf{r}|^2\rangle, \end{aligned} \tag{6.42}$$

which is consistent with our expression for the torque found in the Sec. 6.1 with $S = -1$ and $\omega = 1$, verifying that the torque associated with the singularities after symmetry breaking is generated by the Magnus force. Therefore, the dynamics of our singularities after symmetry breaking can be described as follows: First, the action of the symmetric impulse introduces an effective singular repulsive harmonic potential that splits $N = 4$ single daughter singularities out of the original parent singularity. As these singularities begin to travel away from the origin, they gain angular momentum from the effective external torque caused by the Magnus force and rotate around the axis of symmetry. Eventually, the effective harmonic potential is overpowered by the trapping potential, so the singularities travel back toward the origin, and settle into oscillatory motion about the origin.

CHAPTER 7

CONVERGENCE STUDIES AND NUMERICAL ANALYSIS

We can compare the analytical trajectories from Sec. 5.3 with the actual minima of the wave function amplitude, found using the *minimize* command in Mathematica on the wave function given after the operation of the full Feynman propagator. We also compare the analytical trajectories with numerical data generated by numerically solving the Gross-Pitaevskii equation in (2.6). To begin, we compare the analytic trajectories with the full Feynman propagator to determine the accuracy of the analytical trajectories for various impulse areas. We then use the same value for impulse area, and compare to numerical data for three different impulse strengths and durations. For both studies, we create a list of points at different times using the analytic equations found in Sec. 5.3, and use the standard error analysis equation given in (7.1) to determine the validity of the analytical trajectories versus the numerical data, found by either using the *minimize* command or by numerical integration. Later, we demonstrate using numerical data obtained from full solution of the Gross-Pitaevskii equation the effect particle-particle interactions have when nonlinearity, g, is reintroduced. We can calculate the error between two methods by using the formula

$$\varepsilon = \mathrm{Log}_{10}\left|\frac{r_1 - r_2}{\frac{1}{2}(r_1 + r_2)}\right| \tag{7.1}$$

where $r = \tilde{x}^2 + \tilde{y}^2$.

7.1 Linear Comparison

To compare the analytic trajectories to their actual locations in the wave function found using the full Feynman propagator, we must find a way to track the singularities. Due to the non-analyticity of the wave function, we must use the *Minimize* command in Mathematica in order to track the singularities for various time steps. Using a *Do*

loop, we can append the location of the minima in the fourth quadrant to a list and plot the trajectories. As we do so, we can compare the analytical trajectories (in pink) with the located minima of the full Feynman propagator (blue) for $v = 5 \times 10^{-5}$ in Figure 7.1. The value of v is a numerical representation of the impulse area, $\Delta V \Delta t$, as described by the potential profile in 4.

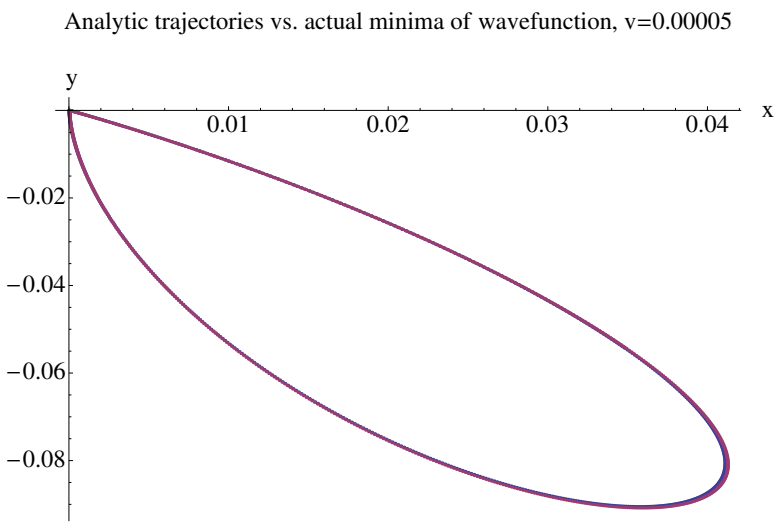

Figure 7.1: The analytical trajectories (pink) are plotted against the minima of the full Feynman propagator (blue) for discrete time steps, using a value of $v = 5 \times 10^{-5}$ for the area of the symmetry breaking impulse. The analytical trajectories are a good description of the singularity motion for small impulse areas.

We then calculate the error between the two methods using (7.1). As one can see in Figure 7.2, the error is largest at the apex of the petal loop, but is still within 0.5% of the amplitude minima. The first few points in Figure 7.2 have larger error due to the close proximity of the singularities immediately after symmetry breaking. The *minimize* command searches for a local minima, so when all four external singularities are very close to each other, the local minima could be from any of the singularities, increasing the error. If we repeat the calculations of error for various impulse areas v, we see that the error increases near the apex of the petal, but remains low near the origin. These results show that the analytic trajectories are the best approximations for extremely thin impulses, but are still valid near the origin for larger impulses.

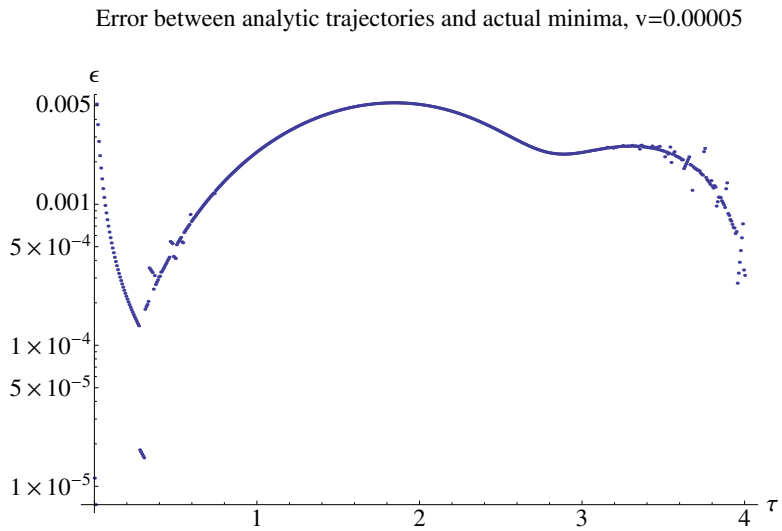

Figure 7.2: Error between the analytical trajectories and the local minima of the full Feynman propagator wave function for $v = 5 \times 10^{-5}$ plotted on logarithmic scale. The error is always less than 0.5%. The scattered points at the beginning and end of the plot are due to the *minimize* command in Mathematica being unable to distinguish between the four external singularities when they are extremely close to the origin.

The error is insignificant until the outer edge of the petals. The increase in error is most likely due to the various approximation techniques used to calculate the analytical trajectories, one of which was working close to the origin. We can increase the value of the impulse area v to observe the loss of validity as the area of the impulse increases. As one can see in Figure 7.3, the error significantly increases as the area of the impulse increases. The error becomes greatest near the apex of the petal structure, while still being within 5 near the origin. The error rises above 5 for times greater than $\tau \approx 0.5$ for the large impulse area, $v = 5 \times 10^{-3}$.

Although we see that the error increases significantly as v increases, we do not know whether it is the impulse potential itself or the duration of the impulse that causes the error to increase. We test three different durations, all for impulse area $v = 5 \times 10^{-4}$, in the next section.

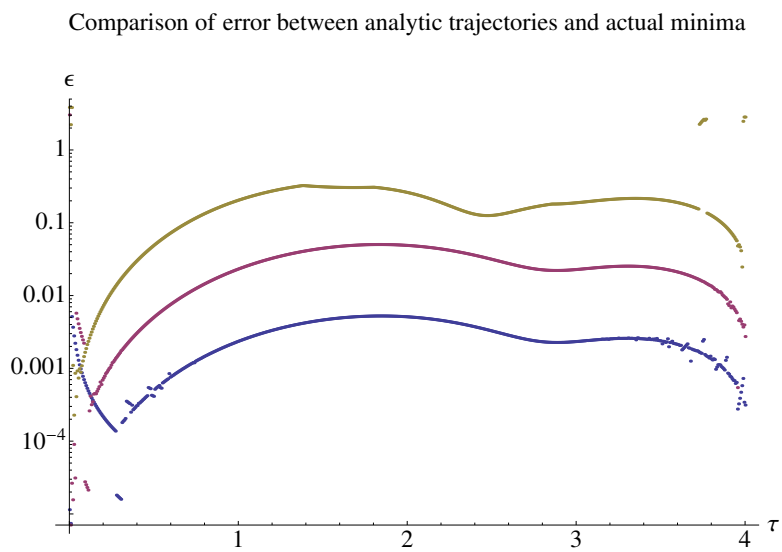

Figure 7.3: Error for impulse areas of $v = 5 \times 10^{-3}$ (yellow), $v = 5 \times 10^{-4}$ (pink), and $v = 5 \times 10^{-5}$ (blue). The error increases significantly as the duration of the impulse increases, but remains the lowest near the origin.

7.2 Numerical Comparison- Linear

The Gross-Pitaevskii equation, given by (2.6), was solved numerically for the same impulse used in the analytical analysis for the linear case of $g = 0$. To determine whether it is the duration of the impulse or the height of the impulse that affects the error, we include numerical integration studies for $g = 0$. Three studies were evaluated for impulse area $v = 5 \times 10^{-4}$, each with a different duration and height:

$$\Delta V(\tilde{x},\ \tilde{y}) = 5 \times 10^{-3}, \quad \Delta t = 10^{-1}, \quad v = 5 \times 10^{-4}; \tag{7.2}$$

$$\Delta V(\tilde{x},\ \tilde{y}) = 5 \times 10^{-2}, \quad \Delta t = 10^{-2}, \quad v = 5 \times 10^{-4}; \tag{7.3}$$

$$\Delta V(\tilde{x},\ \tilde{y}) = 5 \times 10^{-1}, \quad \Delta t = 10^{-3}, \quad v = 5 \times 10^{-4}. \tag{7.4}$$

If we plot each case, we see that there is no significant difference as the duration of the impulse is increased, as shown in Figure 7.4.

If we calculate the error between the analytic and numerical trajectories, we see that the error stays below 10% for all durations once the singularities leave the origin.

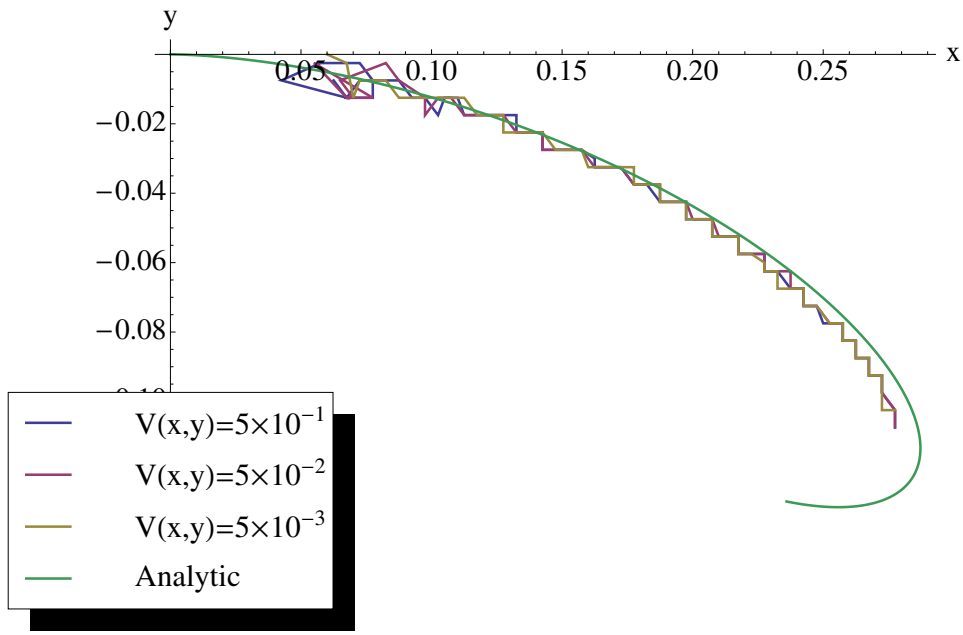

Figure 7.4: Numerical trajectories for impulse durations of $\Delta t = 10^{-1}$, $\Delta t = 10^{-2}$, and $\Delta t = 10^{-3}$, compared to analytic trajectories. We see no significant change as the duration is increased.

The large error near the origin is due to the unavoidable limitation related to the grid spacing necessary to compute the minima of the wave function. We plot the error on a logarithmic scale in Figure 7.5.

These results allow us to conclude that the actual duration of the impulse does not significantly change the dynamics of the system so long as the duration is less than the linear time scale, given in (2.7). Mathematically, $\Delta t \ll t_{\text{lin}} = 1/2$ in dimensionless units. We tested three different durations and found that the approximation holds. For the analytic trajectories, this means the approximation is valid to within 5% for impulse areas less than $\Delta V(\tilde{x},\ \tilde{y})\Delta t = 5 \times 10^{-4}$. For small areas, the impulse only serves to break the symmetry of the singularities, and becomes negligible if the duration is increased. In essence, a shallow potential for a longer time which is not governed by the impulse approximation has the same effect as an extremely strong potential for an infinitesimal amount of time, as long as the area $\Delta V(\tilde{x},\ \tilde{y})\Delta t$ remains small.

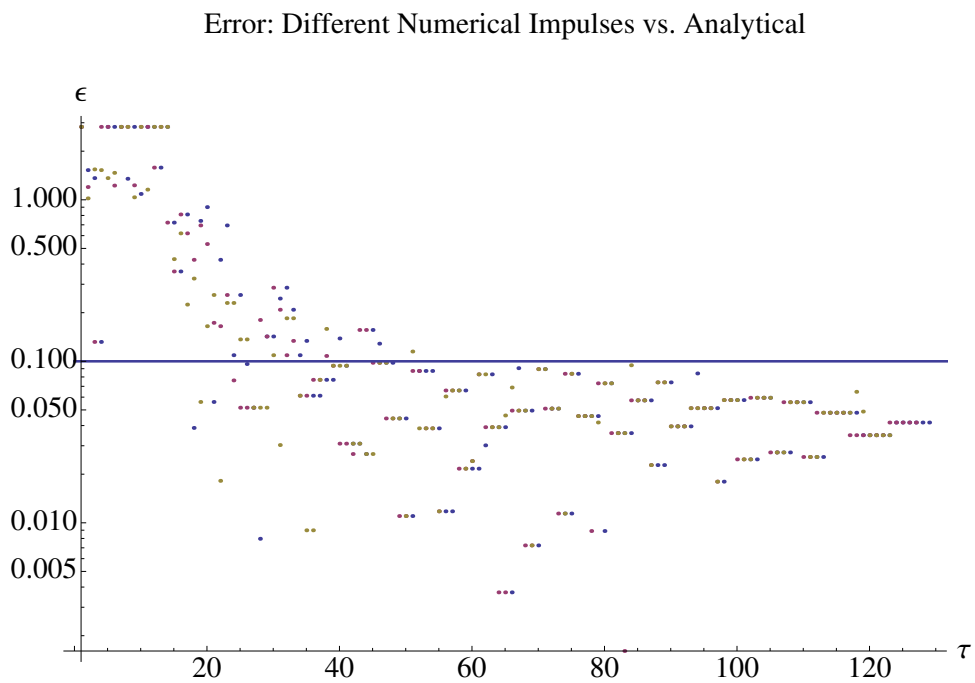

Figure 7.5: Error between numerical trajectories for impulse durations of $\Delta t = 10^{-1}$, $\Delta t = 10^{-2}$, and $\Delta t = 10^{-3}$, and analytic trajectories. We see no significant change as the duration is increased.

7.3 Numerical Comparison- Nonlinear

The Gross-Pitaevskii equation, given by (2.6), was solved numerically for the same impulse used in the analytical analysis for various values of the nonlinearity, g. The nonlinearity depends explicitly on the interaction length between particles, so the higher the nonlinearity, the more the particles are interacting with each other, and the sooner the interactions become significant. We observe the numerical data for attractive nonlinearity and repulsive nonlinearity to see the structure of the vortex trajectories in each case. The effect we pursue is in the very core of the vortex, but there is an unavoidable limitation related to the grid spacing necessary to compute the minima of the wave function. Thus, the numerics have large error near the origin, so we only include numerics to observe the general path taken by each singularity for nonlinear interactions, and do not directly calculate the error between numerics and analytics.

7.3.1 Repulsive Nonlinearity

Repulsive nonlinearity arises when the particles in a Bose-Einstein condensate interact with one another via a positive s-wave scattering length, corresponding to positive values of g. As the nonlinearity becomes larger, the trajectories begin to interact at further distances from each other. This prevents the singularities from recombining at the origin, and instead sends the trajectories into repulsive motion, similar to the behavior of like-charged particles, before returning to the oscillatory path about the origin. Trajectories derived from numerical integration for various repulsive nonlinearities, g, can be seen in Figure 7.6. By increasing the nonlinearity from $g = 0$ to $g = 1, 2, 3, 4$, we see that when the singularities come back to the origin, the nonlinearity begins to show its effects, as seen by the paths taken by the numerical data. As seen in the previous figure, once nonlinearity is introduced, the singularities interact before traveling straight across the origin.

7.3.2 Attractive Nonlinearity

Attractive nonlinearity corresponds to a negative value for the s-wave scattering length, resulting in negative values of the nonlinearity, g. As the attractive nonlinearity becomes increasingly negative, the trajectories begin to interact at further distances from each other. This prevents the singularities from recombining at the origin, behaving similarly to a system of planets, essentially "sling-shotting" around each other before returning to their oscillatory paths. Trajectories calculated numerically for attractive nonlinearity can be seen in Figure 7.8. Once the singularities are far enough away from each other for attractive interactions to lessen their effect, the singularities settle back onto the oscillatory path about the origin as described by the analytic trajectories. By increasing the attractive nonlinearity from $g = 0$ to $g = -1, -2, -3, -4$, we see that the nonlinearity begins to show its effects near the origin, as seen by the paths taken by the numerical data. However, with the attrac-

tive nonlinearity, the trajectories return to the opposite orbit as with the repulsive nonlinear data. In an interacting BEC it is possible for attractions to cause the BEC to collapse, for sufficiently negative g. This interesting possibility is not investigated as it lies outside the scope of the thesis.

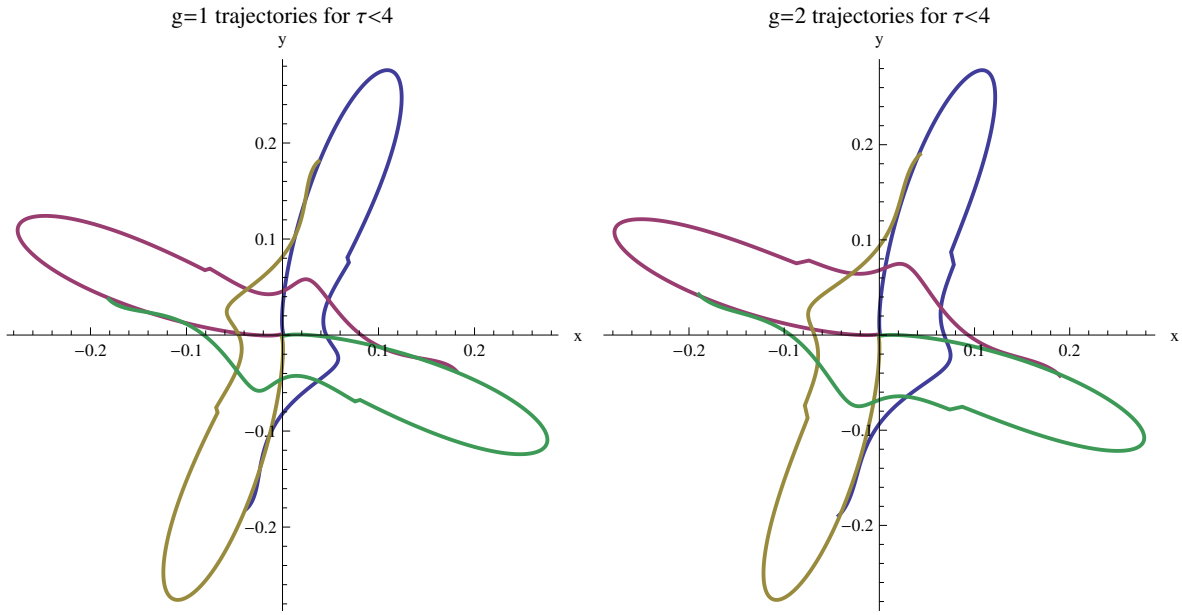

(a) $g = 1$

(b) $g = 2$

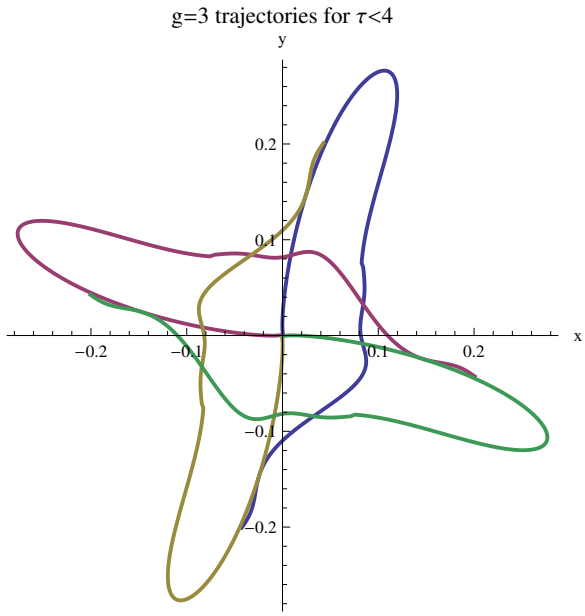

(c) $g = 3$

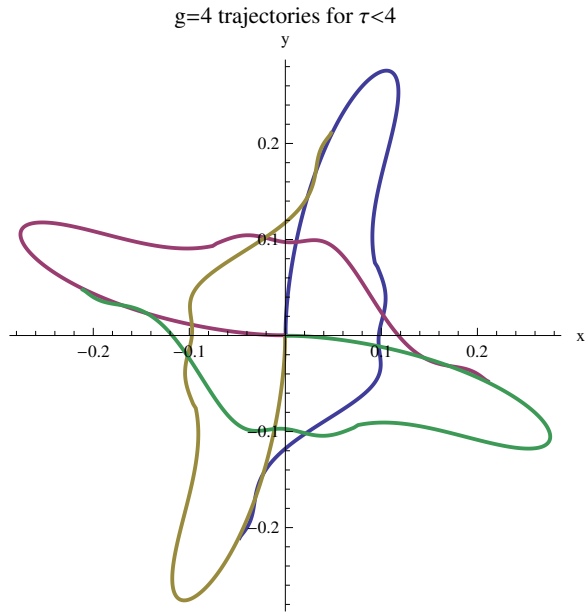

(d) $g = 4$

Figure 7.6: Numerical simulations for (a) repulsive nonlinearity of $g = 1$; (b) repulsive nonlinearity of $g = 2$; (c) repulsive nonlinearity of $g = 3$; (d) repulsive nonlinearity of $g = 4$.

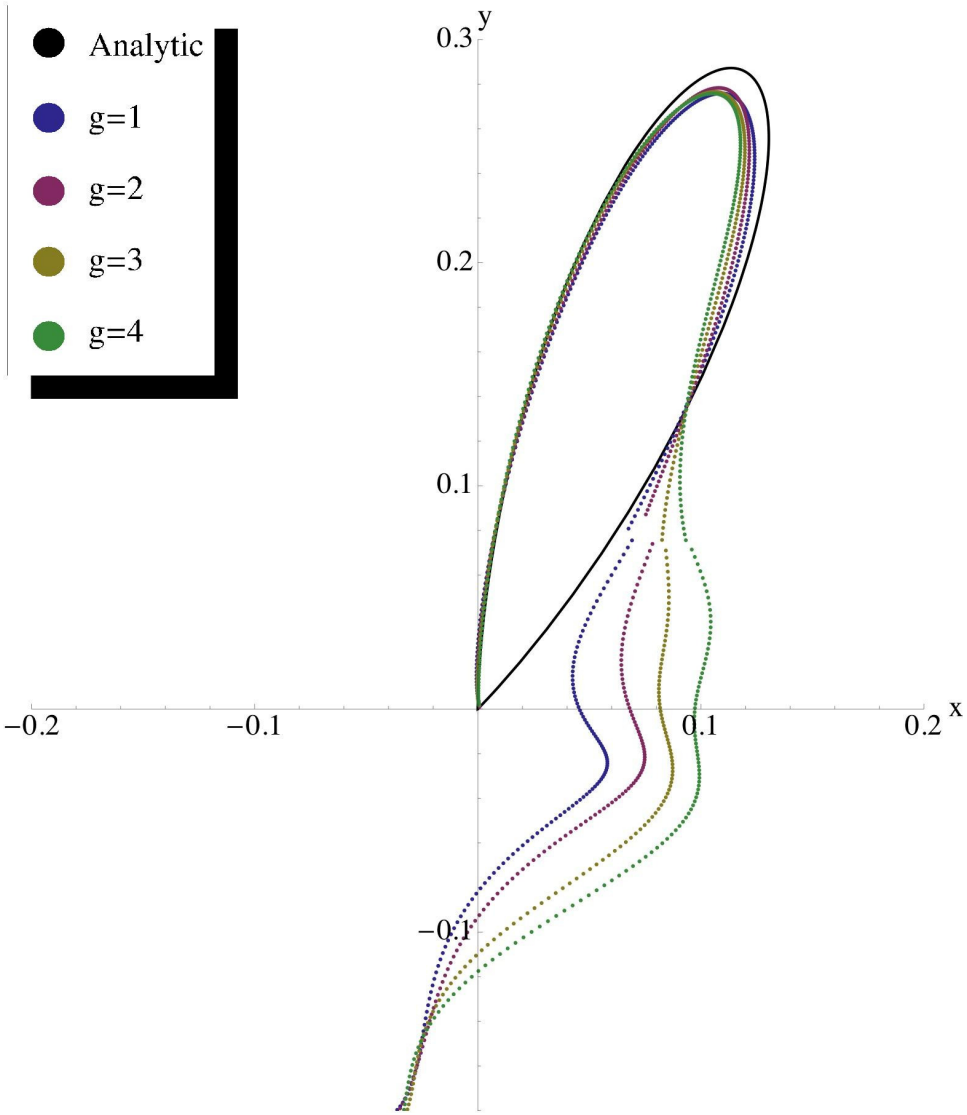

Figure 7.7: Comparison between repulsive nonlinear numerical data for $g = 1, 2, 3, 4$. As the nonlinearity increases, the singularities are less likely to return to the origin. This repulsive motion is similar to a system of like-charged particles in that the singularities interact with each other before returning to the oscillatory path about the origin.

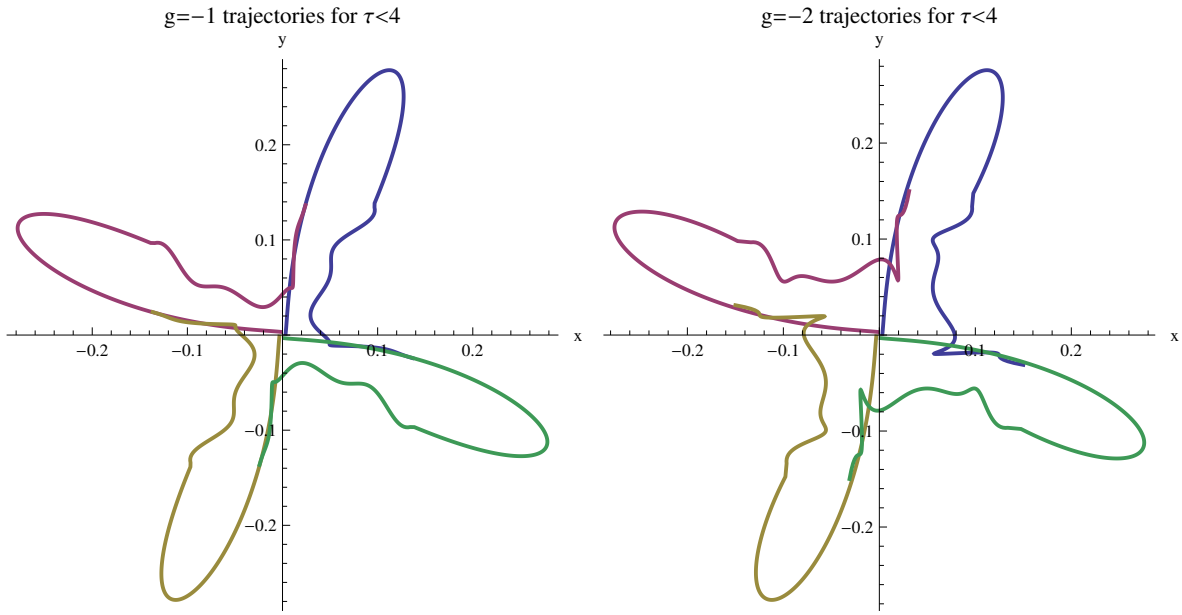

(a) $g = -1$

(b) $g = -2$

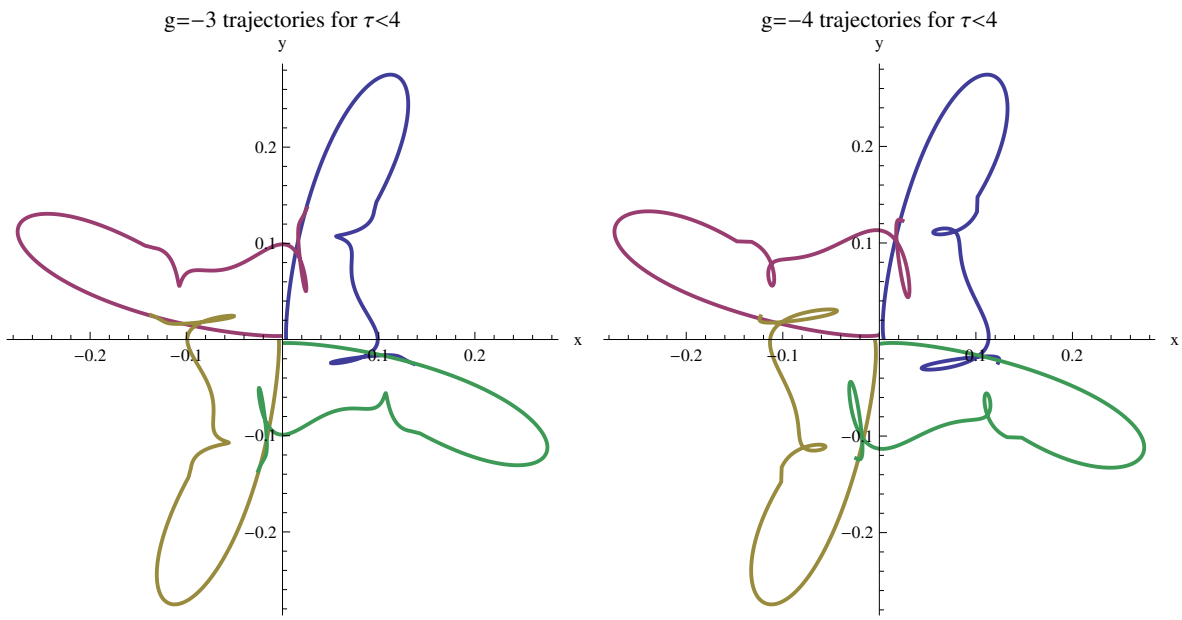

(c) $g = -3$

(d) $g = -4$

Figure 7.8: Numerical simulations for (a) attractive nonlinearity of $g = -1$; (b) attractive nonlinearity of $g = -2$; (c) attractive nonlinearity of $g = -3$; (d) attractive nonlinearity of $g = -4$.

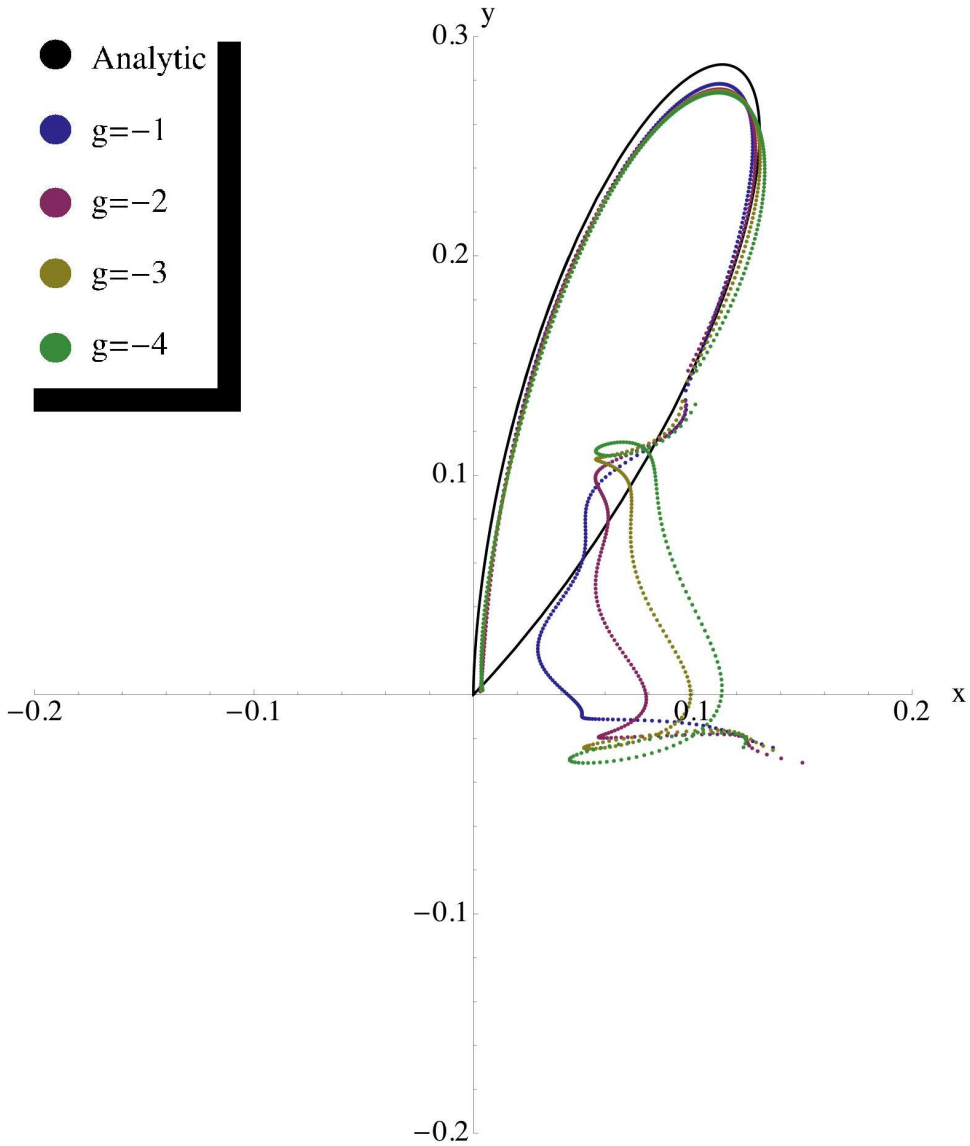

Figure 7.9: Comparison between attractive nonlinear numerical data for $g = -1,\ -2,\ -3,\ -4$. As the nonlinearity increases, the singularities are less likely to return to the origin. The negative nonlinearity sets the trajectories into orbital motion in the opposite direction as the repulsive nonlinear case, essentially "sling-shotting" around each other, causing the singularities to interact with each other before returning to the oscillatory path about the origin.

CHAPTER 8

CONCLUSIONS

We have analytically described the equations of motion for the off-axis daughter singularities that arise after the action of a symmetry breaking impulse on a single parent singularity. For an initial singularity of winding number $\ell = 3$ at the origin and a C_4 discretely symmetric impulse, the symmetry of the initial parent singularity is broken into C_4 as well. Four singularities with winding number $\ell = 1$ oscillate about the origin in a flowering pattern. A single singularity of winding number $m = -1$ remains stationary at the origin. All future evolution of the singularities is determined by the order of symmetry of the impulse, not by the actual form of the impulse, as one would expect. The singularities are imprinted by the impulse and "remember" the effect of symmetry breaking once back to an ordinary confining harmonic potential. It is intriguing to note that the actual form of the impulse does not change the motion of the singularities. It is the order of symmetry and the overall impulse area, $\Delta V \Delta t$, that determine all future propagation patterns. The symmetry determines the pattern of the singularities after symmetry breaking, and the impulse area determines how far the singularities travel away from the origin. The analytical trajectories of the off-axis singularities give rise to a blossoming structure. The singularities periodically oscillate about the origin, while rotating about the axis of symmetry. The disassociation of the initial parent singularity into several smaller daughter singularities is due to an effective singular repulsive harmonic potential that is introduced by the symmetry breaking impulse. The singularities also acquire angular momentum around the axis of symmetry due to an external effective torque. Once the effective repulsive potential is overpowered by the trapping harmonic potential, the singularities settle into an oscillatory pattern as expected in a harmonic trap. The analytic trajectories were compared with the local minima of the full Feynman propagator wave function for

impulse strengths of $v = 5 \times 10^{-3}$, $v = 5 \times 10^{-4}$, and $v = 5 \times 10^{-5}$. Comparison with the full Feynman propagator showed the trajectories to be within 0.5% error for $v = 5 \times 10^{-5}$, 5% error for $v = 5 \times 10^{-4}$, and 50% error for $v = 5 \times 10^{-3}$. The increase in error as the impulse area is increased is due primarily to approximations made in the analytical analysis, mainly the assumption we were working close to the origin. By superimposing the analytic trajectories with the local minima of the full Feynman propagator, we see that they are in agreement for small impulse strengths.

We also conclude that the actual duration of the impulse does not significantly change the dynamics of the system so long as the total impulse area is small, less than $\Delta V(\tilde{x},\ \tilde{y})\Delta t = 5 \times 10^{-4}$ to keep the error below 10%. For small areas, the impulse only serves to break the symmetry of the singularities. In essence, a shallow potential for a longer time which is not governed by the impulse approximation has the same effect as an extremely strong potential for an infinitesimal amount of time, as long as the area $\Delta V(\tilde{x},\ \tilde{y})\Delta t$ remains small. The initial break-up of the singularity is completely controlled by linear effects. It is only long-time behavior that requires full nonlinear analysis due to the interaction between particles in an interacting BEC. In the future, one might expand this theory to include an analytical model treating vortices as interacting point charges or singularities. This would allow us to treat vortex recombination for the interacting cases. For example, the image method of a charge at a boundary has been successfully applied to understand statics of vortices in BEC. Recently, point-charge methods have been successfully applied to vortex dynamics [115].

REFERENCES CITED

[1] P. G. Saffman. *Vortex Dynamics*. Cambridge University Press, New York, NY, 1992.

[2] R. Davies-Jones, R. J. Trapp, and H. B. Bluestein. *Severe Convective Storms*. National Severe Storms Laboratory, Norman, OK, 2001.

[3] P. Tanga, P. Michel, and D. C. Richardson. Planetesimal clusters in a Keplerian disk. *Astron. Astrophys.*, **395**:613, 2002.

[4] J. D. Barow, R. Maartens, and C. G. Tsagas. Cosmology with inhomogeneous magnetic fields. *Phys. Rep.*, **449**:131, 2007.

[5] L. M. Pismen. *Vortices in Nonlinear Fields*. Clarendon, Oxford, London, 1999.

[6] U. Essmann and H. Träuble. The direct observation of individual flux lines in type II superconductors. *Phys. Lett.*, **24A**(10):526, 1967.

[7] D. R. Tilley and J. Tilley. *Superfluidity and Superconductivity*. Hilger, London, third edition, 1990.

[8] G. Blatter. Vortices in high-temperature superconductors. *Rev. Mod. Phys.*, **66**(4):1125, 1994.

[9] J. M. Kosterlitz and D. J. Thouless. Ordering, metastability and phase transitions in two-dimensional systems. *J. Phys. C*, **6**:1181, 1973.

[10] A. Desyatnikov, L. Torner, and Y. S. Kivshar. *Progress in Optics*, volume **47**. North-Holland, Amsterdam, 2005.

[11] M. S. Soskin and M. V. Vasnetsov. Nonlinear singular optics. *Pure Appl. Opt.*, **7**:301, 1998.

[12] M. R. Matthews, B. P. Anderson, P. C. Haljan, D. S. Hall, C. E. Wieman, and E. A. Cornell. Vortices in a Bose-Einstein condensate. *Phys. Rev. Lett.*, **83** (13):2498, 1999.

[13] K. W. Madison, F. Chevy, W. Wohlleben, and J. Dalibard. Vortex formation in a stirred Bose-Einstein condensate. *Phys. Rev. Lett.*, **84**(5):806, 2000.

[14] F. Chevy, K. W. Madison, and J. Dalibard. Measurement of the angular momentum of a rotating Bose-Einstein condensate. *Phys. Rev. Lett.*, **85**(11): 2223, 2000.

[15] B. P. Anderson, P. C. Haljan, C. A. Regal, D. L. Feder, L. A. Collins, C. W. Clark, and E. A. Cornell. Watching dark solitons decay into vortex rings in a Bose-Einstein condensate. *Phys. Rev. Lett.*, **86**(14):2926, 2001.

[16] J. R. Abo-Shaeer, C. Raman, J. M. Vogels, and W. Ketterle. Observation of vortex lattices in Bose-Einstein condensates. *Science*, **292**(5516):476–479, 2001.

[17] Z. Dutton, M. Budde, C. Slowe, and L. Vestergaard Hau. Observation of quantum shock waves created with ultra-compressed slow light pulses in a Bose-Einstein condensate. *Science*, **293**(5530):663, 2001.

[18] S. Inouye, S. Gupta, T. Rosenband, A. P. Chikkatur, A. Görlitz, T. L. Gustavson, A. E. Leanhardt, D. E. Pritchard, and W. Ketterle. Observation of vortex phase singularities in Bose-Einstein condensates. *Phys. Rev. Lett.*, **87**(8):080402, 2001.

[19] C. Raman, J. R. Abo-Shaeer, J. M. Vogels, K. Xu, and W. Ketterle. Vortex nucleation in a stirred Bose-Einstein condensate. *Phys. Rev. Lett.*, **87**(21): 210402, 2001.

[20] A. E. Leanhardt, A. Görlitz, A. P. Chikkatur, D. Kielpinski, Y. Shin, D. E. Pritchard, and W. Ketterle. Imprinting vortices in a Bose-Einstein condensate using topological phases. *Phys. Rev. Lett.*, **89**(19):190403, 2002.

[21] Y. Shin, M. Saba, M. Vengalattore, T. A. Pasquini, C. Sanner, A. E. Leanhardt, M. Prentiss, D. E. Pritchard, and W. Ketterle. Dynamical instability of a doubly quantized vortex in a Bose-Einstein condensate. *Phys. Rev. Lett.*, **93**:160406, 2004.

[22] D. R. Scherer, C. N. Weiler, T. W. Neely, and B. P. Anderson. Vortex formation by merging of multiple trapped Bose-Einstein condensates. *Phys. Rev. Lett.*, **98**:110402, 2007.

[23] S. Thanvanthri, K. Kapale, and J. P. Dowlin. Ultra-stable matter-wave gyroscopy with counter-rotating vortex superpositions in Bose-Einstein condensates. *arXiv*, **0907**(1138v1), 2009.

[24] Y. Castin, Z. Hadzibabic, S. Stock, J. Dalibard, and S. Stringari. Quantized vortices in the ideal Bose gas: A physical realization of random polynomials. *Phys. Rev. Lett.*, **96**:040405, 2006.

[25] M.V. Berry and M.R. Dennis. Topological events on wave dislocation lines: Birth and death of loops, and reconnection. *J. Phys. A-Math. Theor.*, **40**:65, 2007.

[26] M.A. Garciá-March, A. Ferrando, M. Zacarés, S. Sahu, and D.E. Ceballos-Herrera. Symmetry, winding number, and topological charge of vortex solitons in discrete-symmetry media. *Phys. Rev. A*, **79**:053820, 2009.

[27] M. Hamermesh. *Group Theory and its Applications to Physical Problems.* Addison-Wesley, Reading, MA, first edition, 1964.

[28] A. Ferrando, M. Zacarés, and M. A. García-March. Vorticity cutoff in nonlinear photonic crystals. *Phys. Rev. Lett.*, **95**:043901, 2005.

[29] V. Peŕez-García and M.A. Garciá-March. Symmetry-assisted vorticity control in Bose-Einstein condensates. *Phys. Rev. A*, **75**:033618, 2007.

[30] M. A. García-March, A. Ferrando, M. Zacarés, J. Vijande, and L. D. Carr. Angular pseudomomentum theory for the generalized nonlinear Schrödinger equation in discrete rotational symmetry media. *Physica D*, **238**:1432, 2009.

[31] M. Zacarés, M. A. García-March, J. Vijande, A. Ferrando, and E. Merino. Topological charge selection rule for phase singularities. *Phys. Rev. A*, **80**: 043812, 2009.

[32] K. A. Commeford, M. A. García March, A. Ferrando, and L. D. Carr. Symmetry breaking and singularity structure in Bose-Einstein condensates. *arXiv*, **1204**(0727v2), 2012.

[33] P. Nozierez and D. Pines. *Theory of Quantum Liquids, Volume II: Superfluid Bose Liquids.* Westview Press, Boulder, CO 80301, 1994.

[34] G. Watanabe. Vortex-antivortex oscillation and tunneling in Bose-Einstein condensates. *Laser Physics*, **17**(4):533, 2007.

[35] S. McEndoo, S. Croke, J. Brophy, and Th. Busch. Phase evolution in spatial dark states. *Phys. Rev. A*, **81**:042640, 2010.

[36] I. Coddington, P. Engels, V. Schweikhard, and E.A. Cornell. Observation of Tkachenko oscillations in rapidly rotating Bose-Einstein condensates. *Phys. Rev. Lett.*, **91**(10):100402, 2003.

[37] J.P. Martikainen, K.A. Suominen, L. Santos, T. Schulte, and A. Sanpera. Generation and evolution of vortex-antivortex pairs in Bose-Einstein condensates. *Phys. Rev. A*, **64**:063602, 2001.

[38] P. Kuopanportti, J. A. M. Huhtamäki, and M. Möttönen. Size and dynamics of vortex dipoles in dilute Bose-Einstein condensates. *Phys. Rev. A*, **83**: 011603, 2011.

[39] D. V. Freilich, D. M. Bianchi, A. M. Kaufman, T. K. Langin, and D. S. Hall. Real-time dynamics of single vortex lines and vortex dipoles in a Bose-Einstein condensate. *Science*, **329**:1182, 2010.

[40] T. W. Neely, E. C. Samson, A. S. Bradley, M. J. Davis, and B.P. Anderson. Observation of vortex dipoles in an oblate Bose-Einstein condensate. *Phys. Rev. Lett.*, **104**:160401, 2010.

[41] A. Klein and D. Jaksch. Dynamics of vortices in weakly interacting Bose-Einstein condensates. *Phys. Rev. A*, **76**:043602, 2007.

[42] B. Jackson, J.F. McCann, and C.S. Adams. Vortex line and ring dynamics in trapped Bose-Einstein condensates. *Phys. Rev. A*, **61**:013604, 1999.

[43] Y. Zhang. Numerical study of vortex interactions in Bose-Einstein condensation. *Commun. Comput. Phys.*, **8**:327, 2010.

[44] I. Bialynicki-Birula, Z. Bialynicki-Birula, and C. Sliwa. Motion of vortex lines in quantum mechanics. *Phys. Rev. A*, **61**:032110, 2000.

[45] I. Bialynicki-Birula and Z. Bialynicki-Birula. Motion of vortex lines in nonlinear wave mechanics. *Phys. Rev. A*, **65**:014101, 2001.

[46] M.V. Berry and M.R. Dennis. Knotting and unknotting of phase singularities: Helmholtz waves, paraxial waves and waves 2 + 1 spacetime. *J. Phys. A-Math. Gen.*, **34**:8877, 2001.

[47] E. Infeld and A Senatorski. Theoretical confirmation of Feynman's hypothesis on the creation of circular vortices in Bose-Einstein condensates. *J. Phys.-Condens. Matter*, **15**:5865, 2003.

[48] D.A. Wisniacki, E.R. Pujals, and F. Borondo. Vortex interaction, chaos and quantum probabilities. *Europhys. Lett.*, **73**:671, 2006.

[49] D.A. Wisniacki, E.R. Pujals, and F. Borondo. Vortex dynamics and their interactions in quantum trajectories. *J. Phys. A:Math. Theor.*, **40**:14353, 2007.

[50] L. C. Crasovan, G. Molina-Terriza, J. P. Torres, and L. Torner. Globally linked vortex clusters in trapped wave fields. *Phys. Rev. E*, **66**:036612, 2002.

[51] T. Kobayashi and T. Shimbori. Zero-energy solutions and vortices in Schrödinger equations. *Phys. Rev. A*, **65**:042108, 2002.

[52] L. C. Crasovan, V. Vekslerchik, V. M. Pérez-García, J. P. Torres, and D. Mihalache. Stable vortex dipoles in non-rotating Bose-Einstein condensates. *Phys. Rev. A*, **68**:063609, 2003.

[53] Q. Zhou and H. Zhai. Vortex dipole in a trapped atomic Bose-Einstein condensate. *Phys. Rev. A*, **70**:043619, 2004.

[54] M. Liu, L. H. Wen, H. W. Xiong, and M. S. Zhan. Structure and generation of the vortex-antivortex superposed state in Bose-Einstein condensates. *Phys. Rev. A*, **73**:063620, 2006.

[55] Y. F. Chen and K. F. Huang. Quantum manifestations of classical periodic orbits in a square billiard: Formation of vortex lattices. *Phys. Rev. E*, **66**: 066210, 2002.

[56] R. Geurts, M.V. Milos, and F.M. Peeters. Topologically trapped vortex molecules in Bose-Einstein condensates. *Phys. Rev. A*, **78**:053610, 2008.

[57] M. Möttönen, S. M. M. Virtanen, T. Isoshima, and M. M. Salomaa. Stationary vortex clusters in non-rotating Bose-Einstein condensates. *Phys. Rev. A*, **71**:033626, 2005.

[58] D. Mihalache, D. Mazilu, B. A. Malomed, and F. Lederer. Vortex stability in nearly-two-dimensional Bose-Einstein condensates with attraction. *Phys. Rev. A*, **73**:043615, 2006.

[59] V. Pietilä, M. Möttönen, T. Isoshima, J. A. M. Huhtamäki, and S. M. M. Virtanen. Stability and dynamics of vortex clusters in non-rotated Bose-Einstein condensates. *Phys. Rev. A*, **74**:023603, 2006.

[60] A. Ferrando. Discrete symmetry vortices as angular Bloch modes. *Phys. Rev. E*, **72**:036612, 2005.

[61] A. Ferrando. *Analytic Calculation of Clustered Phase Singularities*. Unpublished, University of Valencia, Spain, 2008.

[62] E. H. Lieb. The stability of matter and quantum electrodynamics. *Milan J. Math*, **72**:199, 2003.

[63] E. A. Cornell and C. E. Wieman. The Bose-Einstein condensate. *Sci. Am.*, 1998.

[64] K. Burnett, M. Edwards, and C. W. Clark. The theory of Bose-Einstein condensation of dilute gases. *Phys. Today*, **52**(12):37–42, 1999.

[65] M. Massimi. *Pauli's Exclusion Principle: The Origin and Validation of a Scientific Principle*. Cambridge University Press, New York, NY, 2005.

[66] C. C. Bradley, C. A. Sackett, J. J. Tollett, and R. G. Hulet. Evidence of Bose-Einstein condensation in an atomic gas with attractive interactions. *Phys. Rev. Lett.*, **75**(9), 1995.

[67] K. B. Davis, M. O. Mewes, M. R. Andrews, N. J. van Druten, D. S. Durfee, D. M. Kurn, and W. Ketterle. Bose-Einstein condensation in a gas of sodium atoms. *Phys. Rev. Lett.*, **75**(22), 1995.

[68] M.H. Anderson, J.R. Ensher, M.R. Matthews, C.E. Wieman, and E.A. Cornell. Observation of Bose-Einstein condensation in a dilute atomic vapor. *Science*, **269**:198–201, 1995.

[69] T. W. Hänsch and A. L. Schawlow. Cooling of gases by laser radiation. *Opt. Comm.*, **13**(1), 1975.

[70] S. L. Gilbert and C. E. Wieman. Laser cooling and trapping for the masses. *Opt. Photonics News*, **4**(7):8–14, 1993.

[71] W. D. Phillips. Laser cooling and trapping of neutral atoms. *Rev. Mod. Phys.*, **70**(3), 1998.

[72] C. J. Pethick and H. Smith. *Bose-Einstein Condensation in Dilute Gases.* Cambridge University Press, New York, NY, second edition, 2008.

[73] T. Needham. *Visual Complex Analysis.* Oxford University Press, New York, NY, 1997.

[74] B. P. Anderson and P. Meystre. Nonlinear atom optics. *Contemp. Phys.*, **44**: 473, 2003.

[75] K. T. Kapale and J. P. Dowling. Vortex phase qubit: Generating arbitrary and counter-rotating and coherent superpositions in Bose-Einstein condensates via optical angular momentum beams. *Phys. Rev. Lett.*, **95**:173601, 2005.

[76] A. M. Forrest. Meissner and Ochsenfeld revisited. *Eur. J. Phys.*, **4**:117–120, 1983.

[77] P. E. Goa, H. Hauglin, A. A. F. Olsen, D. Shantsev, and T. H. Johansen. Manipulation of vortices by magnetic domain walls. *Appl. Phys. Lett.*, **82**(1), 2003.

[78] E. W. J. Straver, J. E. Hoffman, O. M. Auslaender, D. Rugar, and K. A. Moler. Controlled manipulation of individual vortices in a superconductor. *Appl. Phys. Lett.*, **93**, 2008.

[79] V. Yu. Bazhenov, M. V. Vasnetzov, and M. S. Soskin. Laser beams with screw dislocations in their wavefronts. *JETP Lett.*, **52**(8):429–431, 1991.

[80] G. Molina-Terriza and L. Torner. Vortex revivals with trapped light. *Opt. Lett.*, **26**(20):1601–1603, 2001.

[81] F. S. Roux. Dynamics of an optical vortex dipole in a GRIN lens medium. *Opt. Commun.*, **234**:63–70, 2004.

[82] I. Smalyukh, P. Ackerman, R. P. Trivedi, and T. Lee. Control of matter defects using optical phase singularities. *SPIE Newsroom*, 2010. doi: DOI:10.1117/2.1201008.003079.

[83] K. T. Gahagan and G. A. Swartzlander Jr. Optical vortex trapping of particles. *Opt. Lett.*, **21**(11):827–829, 1996.

[84] D. G. Grier. A revolution in optical manipulation. *Nature*, **424**:21–27, 2003.

[85] A. Ashkin. History of optical trapping and manipulation of small-neutral particles and atoms and molecules. *IEEE J. Sel. Top. Quantum Electron.*, **6**: 841–856, 2000.

[86] G. Wright, M. J. Tucker, P. C. Morton, C. L. Sweitzer-Yoder, and S. E. Smith. Micromanipulation in assisted reproduction: A review of current technology. *Curr. Opin. Obstet. Gyn.*, **10**:221–226, 1998.

[87] M. W. Berns, Y. Tadir, H. Liang, and B. Tromberg. Laser scissors and tweezers. *Methods Cell Biol.*, **55**:71–98, 1998.

[88] A. T. O'Neil and M. J. Padgett. Three-dimensional optical confinement of micron sized metal particles and the decoupling of the spin and orbital angular momentum within an optical spanner. *Opt. Commun.*, **185**:139–143, 2000.

[89] H. Rubinsztein-Dunlop, T. A. Nieminen, M. E. J. Friese, and N. R. Heckenberg. Optical trapping of absorbing particles. *Adv. Quantum Chem.*, **30**:469–492, 1998.

[90] J. E. Curtis and D. G. Grier. Structure of optical vortices. *Phys. Rev. Lett.*, **90**:133901, 2003.

[91] G. Molina-Terriza, J. P. Torres, and L. Torner. Management of the angular momentum of light: Preparation of photons in multidimensional vector states of angular momentum. *Phys. Rev. Lett.*, **88**(1), 2002.

[92] H. He, M. E. J. Friese, N. R. Heckenberg, and H. Rubinsztein-Dunlop. Direct observation of transfer of angular momentum to absorptive particles from a laser beam with a phase singularity. *Phys. Rev. Lett.*, **75**:826–829, 1995.

[93] A. P. Kazantsev, G. I. Surdutovich, and K. V. Yakovlev. *Mechanical Action of Light on Atoms*. World Scientific, Singapore, 1990.

[94] L. Allen, M. W. Beijersbergen, R. J. C. Spreeuw, and J. P. Woerdman. Orbital angular momentum of light and the transformation of Laguerre-Gaussian laser modes. *Phys. Rev. A*, **45**:8185–8189, 1992.

[95] C. H. J. Schmitz, K. Uhrig, J. P. Spatz, and J. E. Curtis. Tuning the orbital angular momentum in optical vortex beams. *Opt. Express*, **14**(15), 2006.

[96] N. K. Langford, R. B. Dalton, M. D. Harvey, J. L. O'Brien, G. J. Pryde, A. Gilchrist, S. D. Bartlett, and A. G. White. Measuring entangled qutrits and their use for quantum bit commitment. *Phys. Rev. Lett.*, **93**(5), 2004.

[97] G. Molina-Terriza, A. Vaziri, R. Ursin, and A. Zeilinger. Experimental coin tossing. *Phys. Rev. Lett.*, **94**:040501, 2005.

[98] A. Vaziri, G. Weihs, and A. Zeilinger. Experimental two-photon and three-dimensional entanglement for quantum communication. *Phys. Rev. Lett.*, **89**(24), 2002.

[99] A. Moir, A. Vaziri, G. Weihs, and A. Zeilinger. Entanglement of the orbital angular momentum states of photons. *Nature*, **412**:313–316, 2001.

[100] J. Leach, M. J. Padgett, S. M. Barnett, S. Franke-Arnold, and J. Courtial. Measuring the orbital angular momentum of a single photon. *Phys. Rev. Lett.*, **88**(25), 2002.

[101] A. Vaziri, J. W. Pan, T. Jennewein, G. Weihs, and A. Zeilinger. Concentration of higher dimensional entanglement: Qutrits of photon orbital angular momentum. *Phys. Rev. Lett.*, **91**(22), 2003.

[102] J. Ouellette. Seeing the future in photonic crystals. *The Industrial Physicist*, **7**(6):14–17, 2001.

[103] D. T. Moore. Gradient index optics: A review. *Appl. Optics*, **19**(7): 1035–1038, 1980.

[104] Sir A. Schuster. *An Introduction to the Theory of Optics*. Edward Arnold, London, 1904.

[105] M. Abramowitz and I. Stegun. *Handbook of Mathematical Functions with Formulas, Graphs, and Mathematical Tables*. National Bureau of Standards. Washington, D.C., 1964.

[106] L. P. Pitaevskii. Vortex lines in an imperfect Bose gas. *Sov. Phys. JETP-USSR*, **13**(2), 1961.

[107] L. D. Carr, M. J. Holland, and B. A. Malomed. Macroscopic quantum tunneling of Bose-Einstein condensates in a potential well of finite depth. *J. Phys. B: At. Mol. Opt.*, 38:3217, 2005.

[108] D. J. Griffiths. *Introduction to Quantum Mechanics*. Pearson Prentice Hall, Upper Saddle River, NJ 07458, 2005.

[109] B. Friedman. *Principles and Techniques of Applied Mathematics*. Dover Publications, 1990.

[110] R. Shankar. *Principles of Quantum Mechanics*. Springer Science + Business Media, Inc., 233 Spring St, New York, NY 10013, 1994.

[111] F. Chaos, L. Chaos-Cador, and E. Ley-Koo. Free-particle and harmonic-oscillator propagators in two and three dimensions. *RECEN*, **4**(2): 145–149, 2002.

[112] W. Magnus. On the exponential solution of differential equations for a linear operator. *Comm. Pur. Appl. Math VII*, **7**:649–673, 1954.

[113] D. L. Andrews. *Structured Light and its Applications: An Introduction to Phase Structured Beams and Nanoscale Optical Forces*. Elsevier Inc., Burlington, MA 01803, 2008.

[114] I. Kiyosi. *Encyclopedic Dictionary of Mathematics*. MIT Press, Cambridge, MA 02142, 1993.

[115] O. Fialko, A. S. Bradley, and J. Brand. Quantum tunneling of a vortex between two pinning potentials. *Phys. Rev. Lett.*, **108**:015301, 2012.

```
ClearAll["Global`*"]
```

Here we define our initial wave function for propagation.

$$\text{wave}[x\_, y\_] := \sqrt{\frac{1}{6}}\ (x + i\,y)^a\ \frac{1}{\sqrt{n!\,2^n}}\ \frac{1}{\sqrt{m!\,2^m}}\ \frac{1}{\sqrt{\pi}}\ \text{HermiteH}[n, x]\ \text{HermiteH}[m, y]\ e^{-\frac{1}{2}(x^2+y^2)}$$

Does our wavefunction satisfy the time-independent Shrodinger equation? It indeed does, as 1+a is an integer multiple of $\hbar\omega$'s. The value a is the topological charge of the vortex at the origin. We also set n=m=0, beginning with the Harmonic ground state and creating a vortex.

```
n = 0;
m = 0;
```

```
wave[x, y]
```

$$\frac{e^{\frac{1}{2}(-x^2-y^2)}\ (x + i\,y)^a}{\sqrt{6\,\pi}}$$

```
xd = FullSimplify[D[wave[x, y], {x, 2}]];
yd = FullSimplify[D[wave[x, y], {y, 2}]];
laplace = FullSimplify[xd + yd];
```

$$\text{Simplify}\left[\text{FullSimplify}\left[\left(-\frac{1}{2}\ \text{laplace} + \frac{1}{2}\ (x^2 + y^2)\ \text{wave}[x, y]\right) \Big/ \text{wave}[x, y]\right]\right]$$

1 + a

Finding the angular momentum eigenvalues

```
(x (-i D[wave[x, y], y]) - y (-i D[wave[x, y], x])) / wave[x, y] // FullSimplify
```

a

Is our input function normalized? For the distinct case of a=3, which we will be using in all following calculations, it is.

```
a = 3;
Integrate[Integrate[Abs[wave[x, y]^2], {x, -∞, ∞}], {y, -∞, ∞}]
```

1

Propagator Integral

This is the propagator integral to be carried out. The entire integral requires too much memory, so we append to a list term by term.

$$\text{expanded}[xp\_, yp\_, x\_, y\_, t\_] = \text{Expand}\Big[\frac{1}{2\,i\,\text{Sin}[t]}\ e^{\frac{i\,\text{Cos}[t]\,(x^2+y^2)}{2\,\text{Sin}[t]}}\ e^{\frac{i}{2\,\text{Sin}[t]}\left((xp^2+yp^2)\,\text{Cos}[t]-2\,(x\,xp+y\,yp)\right)}\ \left(1 + i\,vo\,(xp + i\,yp)^4 + i\,v1\,(xp - i\,yp)^4\right)\ \text{wave}[xp, yp]\Big];$$

```
int1[x_, y_, t_] =
  FullSimplify[Integrate[Integrate[expanded[xp, yp, x, y, t][[1]], {xp, -∞, ∞},
     Assumptions → {t ≥ 0, t ∈ Reals}], {yp, -∞, ∞}, Assumptions → {t ≥ 0, t ∈ Reals}]];

int2[x_, y_, t_] =
  FullSimplify[Integrate[Integrate[expanded[xp, yp, x, y, t][[2]], {xp, -∞, ∞},
     Assumptions → {t ≥ 0, t ∈ Reals}], {yp, -∞, ∞}, Assumptions → {t ≥ 0, t ∈ Reals}]];

int3[x_, y_, t_] =
  FullSimplify[Integrate[Integrate[expanded[xp, yp, x, y, t][[3]], {xp, -∞, ∞},
     Assumptions → {t ≥ 0, t ∈ Reals}], {yp, -∞, ∞}, Assumptions → {t ≥ 0, t ∈ Reals}]];

int4[x_, y_, t_] =
  FullSimplify[Integrate[Integrate[expanded[xp, yp, x, y, t][[4]], {xp, -∞, ∞},
     Assumptions → {t ≥ 0, t ∈ Reals}], {yp, -∞, ∞}, Assumptions → {t ≥ 0, t ∈ Reals}]];

int5[x_, y_, t_] =
  FullSimplify[Integrate[Integrate[expanded[xp, yp, x, y, t][[5]], {xp, -∞, ∞},
     Assumptions → {t ≥ 0, t ∈ Reals}], {yp, -∞, ∞}, Assumptions → {t ≥ 0, t ∈ Reals}]];

int6[x_, y_, t_] =
  FullSimplify[Integrate[Integrate[expanded[xp, yp, x, y, t][[6]], {xp, -∞, ∞},
     Assumptions → {t ≥ 0, t ∈ Reals}], {yp, -∞, ∞}, Assumptions → {t ≥ 0, t ∈ Reals}]];

int7[x_, y_, t_] =
  FullSimplify[Integrate[Integrate[expanded[xp, yp, x, y, t][[7]], {xp, -∞, ∞},
     Assumptions → {t ≥ 0, t ∈ Reals}], {yp, -∞, ∞}, Assumptions → {t ≥ 0, t ∈ Reals}]];

int8[x_, y_, t_] =
  FullSimplify[Integrate[Integrate[expanded[xp, yp, x, y, t][[8]], {xp, -∞, ∞},
     Assumptions → {t ≥ 0, t ∈ Reals}], {yp, -∞, ∞}, Assumptions → {t ≥ 0, t ∈ Reals}]];

int9[x_, y_, t_] =
  FullSimplify[Integrate[Integrate[expanded[xp, yp, x, y, t][[9]], {xp, -∞, ∞},
     Assumptions → {t ≥ 0, t ∈ Reals}], {yp, -∞, ∞}, Assumptions → {t ≥ 0, t ∈ Reals}]];

int10[x_, y_, t_] =
  FullSimplify[Integrate[Integrate[expanded[xp, yp, x, y, t][[10]], {xp, -∞, ∞},
     Assumptions → {t ≥ 0, t ∈ Reals}], {yp, -∞, ∞}, Assumptions → {t ≥ 0, t ∈ Reals}]];

int11[x_, y_, t_] =
  FullSimplify[Integrate[Integrate[expanded[xp, yp, x, y, t][[11]], {xp, -∞, ∞},
     Assumptions → {t ≥ 0, t ∈ Reals}], {yp, -∞, ∞}, Assumptions → {t ≥ 0, t ∈ Reals}]];

int12[x_, y_, t_] =
  FullSimplify[Integrate[Integrate[expanded[xp, yp, x, y, t][[12]], {xp, -∞, ∞},
     Assumptions → {t ≥ 0, t ∈ Reals}], {yp, -∞, ∞}, Assumptions → {t ≥ 0, t ∈ Reals}]];

int13[x_, y_, t_] =
  FullSimplify[Integrate[Integrate[expanded[xp, yp, x, y, t][[13]], {xp, -∞, ∞},
     Assumptions → {t ≥ 0, t ∈ Reals}], {yp, -∞, ∞}, Assumptions → {t ≥ 0, t ∈ Reals}]];

int14[x_, y_, t_] =
  FullSimplify[Integrate[Integrate[expanded[xp, yp, x, y, t][[14]], {xp, -∞, ∞},
     Assumptions → {t ≥ 0, t ∈ Reals}], {yp, -∞, ∞}, Assumptions → {t ≥ 0, t ∈ Reals}]];

int15[x_, y_, t_] =
  FullSimplify[Integrate[Integrate[expanded[xp, yp, x, y, t][[15]], {xp, -∞, ∞},
     Assumptions → {t ≥ 0, t ∈ Reals}], {yp, -∞, ∞}, Assumptions → {t ≥ 0, t ∈ Reals}]];

int16[x_, y_, t_] =
  FullSimplify[Integrate[Integrate[expanded[xp, yp, x, y, t][[16]], {xp, -∞, ∞},
     Assumptions → {t ≥ 0, t ∈ Reals}], {yp, -∞, ∞}, Assumptions → {t ≥ 0, t ∈ Reals}]];

int17[x_, y_, t_] =
  FullSimplify[Integrate[Integrate[expanded[xp, yp, x, y, t][[17]], {xp, -∞, ∞},
     Assumptions → {t ≥ 0, t ∈ Reals}], {yp, -∞, ∞}, Assumptions → {t ≥ 0, t ∈ Reals}]];
```

```
int18[x_, y_, t_] =
  FullSimplify[Integrate[Integrate[expanded[xp, yp, x, y, t][[18]], {xp, -∞, ∞},
     Assumptions → {t ≥ 0, t ∈ Reals}], {yp, -∞, ∞}, Assumptions → {t ≥ 0, t ∈ Reals}]];

int19[x_, y_, t_] =
  FullSimplify[Integrate[Integrate[expanded[xp, yp, x, y, t][[19]], {xp, -∞, ∞},
     Assumptions → {t ≥ 0, t ∈ Reals}], {yp, -∞, ∞}, Assumptions → {t ≥ 0, t ∈ Reals}]];

int20[x_, y_, t_] =
  FullSimplify[Integrate[Integrate[expanded[xp, yp, x, y, t][[20]], {xp, -∞, ∞},
     Assumptions → {t ≥ 0, t ∈ Reals}], {yp, -∞, ∞}, Assumptions → {t ≥ 0, t ∈ Reals}]];

FullSimplify[int1[x, y, t] + int2[x, y, t] + int3[x, y, t] + int4[x, y, t] + int5[x, y, t] +
  int6[x, y, t] + int7[x, y, t] + int8[x, y, t] + int9[x, y, t] + int10[x, y, t] +
  int11[x, y, t] + int12[x, y, t] + int13[x, y, t] + int14[x, y, t] + int15[x, y, t] +
  int16[x, y, t] + int17[x, y, t] + int18[x, y, t] + int19[x, y, t] + int20[x, y, t]]

ϕ[x_, y_, t_] :=
```

$$e^{-8 i t-\frac{x^2}{2}-\frac{y^2}{2}} \sqrt{\frac{\pi}{6}} \left(e^{4 i t} (x+i y)^3+i\, vo\, (x+i y)^7+v1\, (i x+y) \left(24 e^{6 i t}+36 e^{4 i t} \left(-2+x^2+y^2\right)+\left(-12+x^2+y^2\right) \left(x^2+y^2\right)^2+12 \left(-2+3 x^2+3 y^2\right)+12 e^{2 i t} \left(6+x^4-6 y^2+y^4+2 x^2 \left(-3+y^2\right)\right)\right)\right)$$

To see if we are achieving similar shapes to the numerical results, we must give the symmetry breaking parameters, vo and v1, numerical values, along with the characteristic length L. The value "span" is a range for graphing purposes.

```
l = 1;
vo = .0005;
v1 = .0005;
span = .3;
a = 3;

amplitude = ContourPlot3D[Abs[ϕ[x, y, t]] == .001,
   {x, -span, span}, {y, -span, span}, {t, 0, π}, PlotPoints → 30, Mesh → None,
   ContourStyle → Directive[Pink, Opacity[0.5], Specularity[White, 30]],
   ViewPoint → Top, PlotLabel → Style["Contour plot of |ϕ(x, y, t)|", Large],
   LabelStyle → Large, AxesLabel → {"x", "y    ", "  t "}, ImageSize → 500,
   Ticks → {{{-0.2, "-0.2 "}, {0, "0.0 "}, {0.2, "0.2 "}}, {{-0.2, "-0.2"},
      {0, "0.0"}, {0.2, "0.2"}}, {{0, " 0 "}, {1, " 1  "}, {2, " 2 "}, {3, " 3 "}}}];

Export["amplitude.eps", amplitude]

amplitude.eps

Clear[l, vo, v1]
```

Complex Coordinates

Now we desire to put our final wavefunction in terms of the complex coordinate, χ=x+i y.

```
replace = {x → 1/2 (χ + χstar), y → 1/(2 i) (χ - χstar)};
replace2 =
  {χ χstar^2 → χmag^2 χstar, χ^2 χstar^3 → χmag^4 χstar, χ^3 χstar^4 → χmag^6 χstar, χ χstar → χmag^2};
```

Here we separate into the form $A_+ \chi^7 + A_0(t)\,\chi^3 + A_-(|\chi|, t)\,\chi^*$.

```
frontbits = FullSimplify[ϕ[x, y, t] /. replace][[1]] FullSimplify[ϕ[x, y, t] /. replace][[2]]
```

$$e^{-8 i t - \frac{\chi\,\chi\text{star}}{2}} \sqrt{\frac{\pi}{6}}$$

```
collectors = Collect[Expand[FullSimplify[ϕ[x, y, t] /. replace][[3]]] /. replace2, χstar]
```

$$e^{4 i t} \chi^3 + i\,\text{vo}\,\chi^7 + \left(-24 i\,\text{v1} + 72 i\,e^{2 i t}\,\text{v1} - 72 i\,e^{4 i t}\,\text{v1} + 24 i\,e^{6 i t}\,\text{v1} + 36 i\,\text{v1}\,\chi\text{mag}^2 - 72 i\,e^{2 i t}\,\text{v1}\,\chi\text{mag}^2 + 36 i\,e^{4 i t}\,\text{v1}\,\chi\text{mag}^2 - 12 i\,\text{v1}\,\chi\text{mag}^4 + 12 i\,e^{2 i t}\,\text{v1}\,\chi\text{mag}^4 + i\,\text{v1}\,\chi\text{mag}^6\right)\chi\text{star}$$

```
Anot = Coefficient[collectors, χ, 3] /. χmag → Sqrt[χ χstar]
```

$$e^{4 i t}$$

```
Aplus = Coefficient[collectors, χ, 7] /. χmag → Sqrt[χ χstar]
```

$$i\,\text{vo}$$

```
Aminus = Coefficient[collectors, χstar] /. χmag → Sqrt[χ χstar] // FullSimplify
```

$$i\,\text{v1}\left(-24 + 24\,e^{6 i t} + \chi\,\chi\text{star}\,(-6 + \chi\,\chi\text{star})^2 + 36\,e^{4 i t}\,(-2 + \chi\,\chi\text{star}) + 12\,e^{2 i t}\,(6 + \chi\,\chi\text{star}\,(-6 + \chi\,\chi\text{star}))\right)$$

The complex version of ϕ

```
frontbits (Anot χ^3 + Aplus χ^7 + Aminus χstar) // FullSimplify
```

$$e^{-8 i t - \frac{\chi\,\chi\text{star}}{2}} \sqrt{\frac{\pi}{6}} \left(e^{4 i t} \chi^3 + i\,\text{vo}\,\chi^7 + i\,\text{v1}\,\chi\text{star}\left(-24 + 24\,e^{6 i t} + \chi\,\chi\text{star}\,(-6 + \chi\,\chi\text{star})^2 + 36\,e^{4 i t}\,(-2 + \chi\,\chi\text{star}) + 12\,e^{2 i t}\,(6 + \chi\,\chi\text{star}\,(-6 + \chi\,\chi\text{star}))\right)\right)$$

```
ϕcomplex[χ_, χstar_, t_] :=
```

$$e^{-8 i t - \frac{\chi\,\chi\text{star}}{2}} \sqrt{\frac{\pi}{6}} \left(e^{4 i t} \chi^3 + i\,\text{vo}\,\chi^7 + i\,\text{v1}\,\chi\text{star}\left(-24 + 24\,e^{6 i t} + \chi\,\chi\text{star}\,(-6 + \chi\,\chi\text{star})^2 + 36\,e^{4 i t}\,(-2 + \chi\,\chi\text{star}) + 12\,e^{2 i t}\,(6 + \chi\,\chi\text{star}\,(-6 + \chi\,\chi\text{star}))\right)\right)$$

Asymptotic Expansions

```
Series[ϕcomplex[χ, χstar, t], {χ, 0, 1}, {χstar, 0, 1}] // FullSimplify
```

$$\left(32\,e^{-5 i t}\sqrt{6\pi}\,\text{v1}\,\text{Sin}[t]^3\,\chi\text{star} + O[\chi\text{star}]^2\right) + O[\chi\text{star}]^2\,\chi + O[\chi]^2$$

Evidently, the singularity at the origin is due to the symmetry breaking of the vortex, as seen by the dependence on the symmetry breaking parameter v1. If we set v1=0, then $A_- = 0$, and the expansion about χ=0 is instead

```
v1 = 0;
Series[ϕcomplex[χ, χstar, t], {χ, 0, 3}, {χstar, 0, 3}] // FullSimplify
```

$$e^{-4 i t} \sqrt{\frac{\pi}{6}}\, \chi^3 + O[\chi]^4$$

which preserves the initial winding number of a=3, as evidenced by χ^3.

```
Clear[v1]
```

For the off axis singularities, we must solve the equation $A_+ \chi^8 + A_0(t)\, \chi^4 + |\chi|^2 A_-(|\chi|, t) = 0$. Assuming v1 and vo are of the same order and we go to the v=0 limit,

```
Aplus /. vo → 0
```

0

```
Aminus /. v1 → 0
```

0

For the previous equation to be true, it follows that as v→0, $A_0(t)\, \chi^4 \to 0$, and therefore χ→0. Evidentally, χ=χ(v), and in the v<<1 regime it is also true that |χ|<<1.

```
F = Aplus χ^8 + Anot χ^4 + χ χstar Aminus // Expand
```

$$e^{4 i t} \chi^4 + i\, vo\, \chi^8 - 24 i\, v1\, \chi\, \chi star + 72 i\, e^{2 i t}\, v1\, \chi\, \chi star - 72 i\, e^{4 i t}\, v1\, \chi\, \chi star + 24 i\, e^{6 i t}\, v1\, \chi\, \chi star + 36 i\, v1\, \chi^2\, \chi star^2 - 72 i\, e^{2 i t}\, v1\, \chi^2\, \chi star^2 + 36 i\, e^{4 i t}\, v1\, \chi^2\, \chi star^2 - 12 i\, v1\, \chi^3\, \chi star^3 + 12 i\, e^{2 i t}\, v1\, \chi^3\, \chi star^3 + i\, v1\, \chi^4\, \chi star^4$$

For small values of χ, the first terms that comes back into the expression are those in A_- that depend on $|\chi|^2 = \chi\, \chi$star.

```
firstterm = Coefficient[χ χstar Aminus // Expand, χ χstar]
```

$$-24 i\, v1 + 72 i\, e^{2 i t}\, v1 - 72 i\, e^{4 i t}\, v1 + 24 i\, e^{6 i t}\, v1$$

```
Anot χ^4 + firstterm χ χstar
```

$$e^{4 i t} \chi^4 + \left(-24 i\, v1 + 72 i\, e^{2 i t}\, v1 - 72 i\, e^{4 i t}\, v1 + 24 i\, e^{6 i t}\, v1\right) \chi\, \chi star$$

```
insides = -firstterm / e^(4 i t)
```

$$-e^{-4 i t} \left(-24 i\, v1 + 72 i\, e^{2 i t}\, v1 - 72 i\, e^{4 i t}\, v1 + 24 i\, e^{6 i t}\, v1\right)$$

```
phase[t_] := -e^(-4 i t) (-24 i v1 + 72 i e^(2 i t) v1 - 72 i e^(4 i t) v1 + 24 i e^(6 i t) v1)
real[t_] = FullSimplify[Re[phase[t]], Assumptions → {v1 ∈ Reals, l ∈ Reals}];
imaginary[t_] = FullSimplify[Im[phase[t]], Assumptions → {v1 ∈ Reals, l ∈ Reals}];
```

```
R[t_] := FullSimplify[Sqrt[Sqrt[real[t]^2 + imaginary[t]^2] , Assumptions → {t ∈ Reals}]]

realθ[t_] = FullSimplify[Re[phase[t]], Assumptions → {t ∈ Reals, v1 ∈ Reals, l ∈ Reals}];

imaginaryθ[t_] = FullSimplify[Im[phase[t]], Assumptions → {t ∈ Reals, v1 ∈ Reals, l ∈ Reals}];

θ[wind_, t_] :=
 FullSimplify[1/4 ArcTan[realθ[t], imaginaryθ[t]] + wind π/2, Assumptions → {l ∈ Reals, v1 ∈ Reals}]

v1 = .0005;
Plots = ParametricPlot3D[
   {{R[t] Cos[θ[0, t]], R[t] Sin[θ[0, t]], t}, {R[t] Cos[θ[1, t]], R[t] Sin[θ[1, t]], t},
    {R[t] Cos[θ[2, t]], R[t] Sin[θ[2, t]], t}, {R[t] Cos[θ[3, t]], R[t] Sin[θ[3, t]], t}},
   {t, 0, π}, ViewPoint → Top, PlotStyle → Thick, LabelStyle → 23,
   AxesLabel → {"x", "y      ", "  τ  "}, ImageSize → 500,
   Ticks → {{{-0.2, "-0.2 "}, {0, "0.0 "}, {0.2, "0.2 "}}, {{-0.2, "-0.2"},
      {0, "0.0"}, {0.2, "0.2"}}, {{0, " 0 "}, {1, " 1  "}, {2, " 2 "}, {3, " 3 "}}}];

Export["trajectories.eps", Plots]
```

```
trajectories.eps
```

```
Directory[]
```

```
/Users/kelleycommeford
```

Equations of motion

```
Clear[l, v, v1]
```

We further simplify our expression for χ to study the effective potentials immediately after symmetry breaking, when t is approximately zero. Further calculations are done by hand.

```
rapprox[t_] =
 FullSimplify[Series[R[t], {t, 0, 2}], Assumptions → {l ≥ 0, l ∈ Reals, v1 ≥ 0, v1 ∈ Reals}]
```

$$8\sqrt{3}\,\sqrt{v1}\,t^{3/2} + O[t]^{5/2}$$

```
θapprox[t_] =
 FullSimplify[Series[θ[0, t], {t, 0, 1}], Assumptions -> {l ≥ 0, l ∈ Reals, v1 ≥ 0, v1 ∈ Reals}]
```

$$\frac{\pi}{4} - \frac{t}{4} + O[t]^2$$

```
χ[t_] = 8 Sqrt[3] l^3 Sqrt[v1] t^(3/2) e^(i (π/4 - t/4))
```

$$8\sqrt{3}\,e^{i\left(\frac{\pi}{4}-\frac{t}{4}\right)}\,l^3\,t^{3/2}\,\sqrt{v1}$$

```
D[χ[t], t] / χ[t] // FullSimplify
```

$$-\frac{i}{4} + \frac{3}{2\,t}$$

```
D[χ[t], {t, 2}] / χ[t] // FullSimplify
```

$$\frac{12 - t\,(12\,i + t)}{16\,t^2}$$

Convergence- v=0.005

```
Clear[l, v1, vo, minimums3, calculateds3, i, x, y, min3]

l = 1;
v1 = .005;
vo = .005;

minimums3 = {};
calculateds3 = {};
shifted1 = {};
shifted2 = {};
shifted3 = {};
shifted43 = {};
times = {};
Δx3 = .1;
Δy3 = .1;

Do[
 calc = {R[i] Cos[θ[3, i]], R[i] Sin[θ[3, i]]};
 shiftx[b_] := R[i] Cos[θ[b, i] + π/4];
 shifty[b_] := R[i] Sin[θ[b, i] + π/4];
 min3 = If[R[i] > .1,
   Minimize[{Abs[ϕ[x, y, i]], calc[[1]] - Δx3 < x < calc[[1]] + Δx3, calc[[2]] - Δy3 < y < calc[[2]] + Δy3},
     {x, y}][[2]], Minimize[{Abs[ϕ[x, y, i]], calc[[1]] - Δx3 / 10 < x < calc[[1]] + Δx3 / 10,
      calc[[2]] - Δy3 / 10 < y < calc[[2]] + Δy3 / 10}, {x, y}][[2]]];
 AppendTo[minimums3, {x, y} /. min3];
 AppendTo[calculateds3, calc];
 AppendTo[shifted1, {i, shiftx[0], shifty[0]}];
 AppendTo[shifted2, {i, shiftx[1], shifty[1]}];
 AppendTo[shifted3, {i, shiftx[2], shifty[2]}];
 AppendTo[shifted43, {i, shiftx[3], shifty[3]}];
 Clear[min3],
 {i, 0.01, 4, .005}
]

compare3 = ListPlot[{minimums3, calculateds3}, PlotRange → All,
   LabelStyle → Large, ImageSize → 750, AxesLabel → {"  x", " y"}, PlotLabel →
    Style["Analytic trajectories vs. actual minima of wavefunction, v=0.005", Large]];

Export["compare3.eps", compare3]
```

compare3.eps

```
error3 = Abs[(Drop[calculateds3[[All, {1, 2}]], -180] - Drop[minimums3[[All, {1, 2}]], -180])
   / (1/2 (Drop[calculateds3[[All, {1, 2}]], -180] + Drop[minimums3[[All, {1, 2}]], -180]))];

logerror3 = Sqrt[error3[[All, 1]]^2 + error3[[All, 2]]^2];
```

```
lin3 = ListLogPlot[logerror3, AxesLabel → {"τ", "ϵ"},
   LabelStyle → Large, ImageSize → 750, PlotRange → All,
   PlotLabel → Style["Error between analytic trajectories and actual minima, v=0.005",
     Large], DataRange → {0, 4}];

Export["errorlin3.eps", lin3]
```

errorlin3.eps

```
numdata3 = Import["sing_g0_0p005.txt", "Table"];

ListPlot[{numdata3⟦All, {4, 5}⟧, shifted43⟦1 ;; 280, {2, 3}⟧}, Joined → True, PlotRange → All];

matched = {{R[10^-10] Cos[θ[3, 10^-10]], R[10^-10] Sin[θ[3, 10^-10]]}, shifted43⟦39, {2, 3}⟧,
   shifted43⟦61, {2, 3}⟧, shifted43⟦79, {2, 3}⟧, shifted43⟦99, {2, 3}⟧,
   shifted43⟦119, {2, 3}⟧, shifted43⟦139, {2, 3}⟧, shifted43⟦159, {2, 3}⟧,
   shifted43⟦179, {2, 3}⟧, shifted43⟦199, {2, 3}⟧, shifted43⟦219, {2, 3}⟧,
   shifted43⟦239, {2, 3}⟧, shifted43⟦259, {2, 3}⟧, shifted43⟦279, {2, 3}⟧};

errors = Abs[(matched - numdata3⟦All, {4, 5}⟧)/(1/2 (matched + numdata3⟦All, {4, 5}⟧))];

logerrors = Sqrt[errors⟦All, 1⟧^2 + errors⟦All, 2⟧^2];

ListLogPlot[Drop[logerrors, 2], Joined → True, DataRange → {0.2, 1.4}, PlotRange → All];
```

Convergence- v=0.00005

```
Clear[l, v1, vo, minimums, calculateds, i, x, y, min]

l = 1;
v1 = .00005;
vo = .00005;

minimums = {};
calculateds = {};
shifted1 = {};
shifted2 = {};
shifted3 = {};
shifted4 = {};
times = {};
Δx = .001;
Δy = .001;
```

```
Do[
 calc = {R[i] Cos[θ[3, i]], R[i] Sin[θ[3, i]]};
 shiftx[b_] := R[i] Cos[θ[b, i] + π/4];
 shifty[b_] := R[i] Sin[θ[b, i] + π/4];
 min = If[R[i] > .01,
   Minimize[{Abs[ϕ[x, y, i]], calc[[1]] - Δx < x < calc[[1]] + Δx, calc[[2]] - Δy < y < calc[[2]] + Δy},
     {x, y}][[2]], Minimize[{Abs[ϕ[x, y, i]], calc[[1]] - Δx / 10 < x < calc[[1]] + Δx / 10,
      calc[[2]] - Δy / 10 < y < calc[[2]] + Δy / 10}, {x, y}][[2]]];
 AppendTo[minimums, {x, y} /. min];
 AppendTo[calculateds, calc];
 AppendTo[shifted1, {i, shiftx[0], shifty[0]}];
 AppendTo[shifted2, {i, shiftx[1], shifty[1]}];
 AppendTo[shifted3, {i, shiftx[2], shifty[2]}];
 AppendTo[shifted4, {i, shiftx[3], shifty[3]}];
 Clear[min],
 {i, 0.01, 4, .005}
]

compare = ListPlot[{minimums, calculateds}, PlotRange → All,
   LabelStyle → Large, ImageSize → 750, AxesLabel → {"  x", " y"}];

Export["compare.eps", compare]

compare.eps

error = Abs[(Drop[calculateds[[All, {1, 2}]], -180] - Drop[minimums[[All, {1, 2}]], -180])/(1/2 (Drop[calculateds[[All, {1, 2}]], -180] + Drop[minimums[[All, {1, 2}]], -180]))];

logerror = Sqrt[error[[All, 1]]^2 + error[[All, 2]]^2];

lin = ListLogPlot[logerror, AxesLabel → {"τ", "ϵ"},
   LabelStyle → Large, ImageSize → 750, PlotRange → All, DataRange → {0, 4}];

Export["errorlin.eps", lin]

errorlin.eps

numdata = Import["sing_g0_0p00005.txt", "Table"];

ListPlot[{numdata[[All, {4, 5}]], shifted4[[1 ;; 240, {2, 3}]]}, Joined → True, PlotRange → All];
```

Convergence- v=0.0005

```
Clear[l, v1, vo, minimums2, calculateds2, i, x, y, min2]

l = 1;
v1 = .0005;
vo = .0005;
```

```
minimums2 = {};
calculateds2 = {};
shifted1 = {};
shifted2 = {};
shifted3 = {};
shifted42 = {};
times = {};
Δx2 = .01;
Δy2 = .01;

Do[
 calc = {R[i] Cos[θ[3, i]], R[i] Sin[θ[3, i]]};
 shiftx[b_] := R[i] Cos[θ[b, i] + π/4];
 shifty[b_] := R[i] Sin[θ[b, i] + π/4];
 min2 = If[R[i] > .02,
   Minimize[{Abs[ϕ[x, y, i]], calc[[1]] - Δx2 < x < calc[[1]] + Δx2, calc[[2]] - Δy2 < y < calc[[2]] + Δy2},
     {x, y}][[2]], Minimize[{Abs[ϕ[x, y, i]], calc[[1]] - Δx2 / 10 < x < calc[[1]] + Δx2 / 10,
      calc[[2]] - Δy2 / 10 < y < calc[[2]] + Δy2 / 10}, {x, y}][[2]]];
 AppendTo[minimums2, {x, y} /. min2];
 AppendTo[calculateds2, calc];
 AppendTo[shifted1, {i, shiftx[0], shifty[0]}];
 AppendTo[shifted2, {i, shiftx[1], shifty[1]}];
 AppendTo[shifted3, {i, shiftx[2], shifty[2]}];
 AppendTo[shifted42, {i, shiftx[3], shifty[3]}];
 Clear[min2],
 {i, 0.01, 4, .005}
]

compare2 = ListPlot[{minimums2, calculateds2}, PlotRange → All,
   LabelStyle → Large, ImageSize → 750, AxesLabel → {"  x", " y"}, PlotLabel →
    Style["Analytic trajectories vs. actual minima of wavefunction, v=0.0005", Large]];

Export["compare2.eps", compare2]

compare2.eps

error2 = Abs[(Drop[calculateds2[[All, {1, 2}]], -180] - Drop[minimums2[[All, {1, 2}]], -180])/(1/2 (Drop[calculateds2[[All, {1, 2}]], -180] + Drop[minimums2[[All, {1, 2}]], -180]))];

logerror2 = Sqrt[error2[[All, 1]]^2 + error2[[All, 2]]^2];

lin2 = ListLogPlot[logerror2, AxesLabel → {"τ", "ϵ"},
   LabelStyle → Large, ImageSize → 750, PlotRange → All,
   PlotLabel → Style["Error between analytic trajectories and actual minima, v=0.0005",
     Large], DataRange → {0, 4}];

Export["errorlin2.eps", lin2]

errorlin2.eps

numdata2 = Import["sing_g0_0p0005.txt", "Table"];

ListPlot[{numdata2[[All, {4, 5}]], shifted42[[1 ;; 240, {2, 3}]]}, Joined → True, PlotRange → All];

Needs["PlotLegends`"]

compareall = ListLogPlot[{logerror, logerror2, logerror3}, AxesLabel → {"τ", "ϵ"},
   LabelStyle → Large, ImageSize → 750, PlotRange → All, DataRange → {0, 4}];
```

```
Export["compareall.eps", compareall]
```

compareall.eps

Recombination times

```
Clear[l, v1, v0, v]
```

```
R[t]
```

$$8\sqrt{3}\,\left(v1^2\,\mathrm{Sin}[t]^6\right)^{1/4}$$

```
Clear[l, v1]
```

```
Reduce[R[t] == 0, t]
```

(C[1] ∈ Integers && (t == 2 π C[1] || t == π + 2 π C[1])) || v1 == 0

- **Always integer multiples of π, regardless of v or L, so recombination time is half the trapping period.**

```
FullSimplify[D[R[t], t], Assumptions → {l ∈ Reals, v1 ∈ Reals}]
```

$$12\sqrt{3}\,\mathrm{Cot}[t]\,\left(v1^2\,\mathrm{Sin}[t]^6\right)^{1/4}$$

```
Solve[D[R[t], t] == 0, t]
```

$$\left\{\left\{t \to -\frac{\pi}{2}\right\}, \left\{t \to \frac{\pi}{2}\right\}\right\}$$

- **Confirms maximum R is at π/2.**

$$R\left[\frac{\pi}{2}\right]$$

$$8\sqrt{3}\,\left(v1^2\right)^{1/4}$$

$$\mathrm{maxR}[\omega\_, v\_] := 8\sqrt{3}\,\left(\frac{1}{\sqrt{\omega}}\right)^3\sqrt{v}$$

```
Plot3D[maxR[ω, v], {ω, 0.5, 1}, {v, 0, .01}, AxesLabel → {ω, v}];
```

- **As ω goes to 0, the singularities never come back, as expected. Also, as v goes to 0, the singularities never blast apart, as expected.**

```
Plot[{maxR[1, .00005], maxR[1, .005], maxR[1, .05]}, {L, 0, 1}];
```

- **As the strength of the symmetry-breaking impulse increases, the maximum radius increases, as expected.**

Magnus Force

- **The magnus force is given by F=S(ω x v)**

```
ω = S {0, 0, w};
```

$$v = \left\{\frac{3}{4\,t}\,x,\ \frac{3}{4\,t}\,y,\ 0\right\};$$

```
f = Cross[ω, v]
```

$$\left\{-\frac{3\,S\,w\,y}{4\,t},\ \frac{3\,S\,w\,x}{4\,t},\ 0\right\}$$

- **Now we find the torque from this magnus force, τ=r x F**

```
r = {x, y, 0};
Cross[r, f] // FullSimplify
```

$$\left\{0,\ 0,\ \frac{3\,S\,w\,\left(x^2+y^2\right)}{4\,t}\right\}$$

Different V

```
Clear[R, θ, v, v1, vo, n]
```

$$R[v\_,\ t\_] := 8\sqrt{3}\ \left(v^2\,\mathrm{Sin}[t]^6\right)^{1/4}$$

$$\theta[v\_,\ n\_,\ t\_] := \frac{1}{4}\left(2\,n\,\pi + \mathrm{ArcTan}\left[-v\,\mathrm{Cos}[t]\,\mathrm{Sin}[t]^3,\ v\,\mathrm{Sin}[t]^4\right]\right)$$

```
ParametricPlot[{{R[.005, t] Cos[θ[.005, 0, t]], R[.005, t] Sin[θ[.005, 0, t]]},
   {R[.003, t] Cos[θ[.003, 0, t]], R[.003, t] Sin[θ[.003, 0, t]]},
   {R[.002, t] Cos[θ[.002, 0, t]], R[.002, t] Sin[θ[.002, 0, t]]},
   {R[.001, t] Cos[θ[.001, 0, t]], R[.001, t] Sin[θ[.001, 0, t]]},
   {R[.0005, t] Cos[θ[.0005, 0, t]], R[.0005, t] Sin[θ[.0005, 0, t]]},
   {R[0.00005, t] Cos[θ[0.00005, 0, t]], R[0.00005, t] Sin[θ[0.00005, 0, t]]}}, {t, 0, 3.1}];

ListPlot[{{0.005, maxR[1, .005]}, {0.003, maxR[1, .003]},
   {0.002, maxR[1, .002]}, {0.001, maxR[1, .001]}, {0.0005, maxR[1, .0005]},
   {0.00005, maxR[1, .00005]}}, Joined → True, PlotRange → {0, 1}];
```

Impulse Approximation

```
Clear[v0p5t0p001, v0p05t0p01, v0p005t0p1, data, time, fun, v0p5data, v0p05data,
 v0p005data, error0p5, error0p05, error0p005, magerror0p5, magerror0p05, magerror0p005]
```

```
SetDirectory["/Users/kelleycommeford/Dropbox/Kelley CSM/Mathematica"]

/Users/kelleycommeford/Dropbox/Kelley CSM/Mathematica

v0p5t0p001 = Import["V0_0p5_t0p001_A_0p0005.txt", "Table"];

v0p05t0p01 = Import["V0_0p05_t0p01_A_0p0005.txt", "Table"];

v0p005t0p1 = Import["V0_0p005_t0p1_A_0p0005.txt", "Table"];

data[wind_, list_] :=
  {Thread[{R[list] Cos[θ[wind, list] + π / 4], R[list] Sin[θ[wind, list] + π / 4]}]};

time = Range[10^-10, 2, 10^-3] // N;

fun = Nearest[data[1, time][[1]]];

v1 = 0.0005;

v0p5data = Table[fun[v0p5t0p001[[i, {6, 7}]][[1]], {i, Length[v0p5t0p001[[All, {6, 7}]]]}];
v0p05data = Table[fun[v0p05t0p01[[i, {6, 7}]][[1]], {i, Length[v0p05t0p01[[All, {6, 7}]]]}];
v0p005data = Table[fun[v0p005t0p1[[i, {6, 7}]][[1]], {i, Length[v0p005t0p1[[All, {6, 7}]]]}];

error0p5 = Abs[(v0p5data - v0p5t0p001[[All, {6, 7}]]) / (1/2 (v0p5data + v0p5t0p001[[All, {6, 7}]]))];

error0p05 = Abs[(v0p05data - v0p05t0p01[[All, {6, 7}]]) / (1/2 (v0p05data + v0p05t0p01[[All, {6, 7}]]))];

error0p005 = Abs[(v0p005data - v0p005t0p1[[All, {6, 7}]]) / (1/2 (v0p005data + v0p005t0p1[[All, {6, 7}]]))]


magerror0p5 = Sqrt[error0p5[[All, 1]]^2 + error0p5[[All, 2]]^2];

magerror0p05 = Sqrt[error0p05[[All, 1]]^2 + error0p05[[All, 2]]^2];

magerror0p005 = Sqrt[error0p005[[All, 1]]^2 + error0p005[[All, 2]]^2];

errorlin = Show[{ListLogPlot[{magerror0p5, magerror0p05, magerror0p005}, PlotRange → All,
      PlotStyle → Thick, LabelStyle → 23, AxesLabel → {"τ", "ϵ"}, ImageSize → 750],
    LogPlot[0.1, {x, 0, 150}, PlotStyle → Thick]}];

Directory[]

/Users/kelleycommeford/Dropbox/Kelley CSM/Mathematica


Export["impulseerror.eps", errorlin]

impulseerror.eps

Needs["PlotLegends`"]

impulses = ListPlot[{Drop[v0p5t0p001[[All, {4, 5}]], 15], Drop[v0p05t0p01[[All, {4, 5}]], 15],
    Drop[v0p005t0p1[[All, {4, 5}]], 15], data[3, time][[1]]}, Joined → True,
   AxesOrigin → {0, 0}, PlotStyle → Thick, LabelStyle → 23, AxesLabel → {"x", "y"},
   ImageSize → 750, PlotLegend → {Style["V(x,y)=0.5", Large], Style["V(x,y)=0.05", Large],
     Style["V(x,y)=0.005", Large], Style["Analytic", Large]}, LegendSize → {.75, .5}];
```

```
Export["impulses.eps", impulses]
```

```
impulses.eps
```

```
Export["analyticdata.txt", data[1, time][[1]], "Table"]
```

```
analyticdata.txt
```

```
Directory[]
```

```
/Users/kelleycommeford/Dropbox/Kelley CSM/Mathematica
```